Computational Methods for Reconstructing and Analyzing Polycrystalline Microstructures

by

Yufeng Shen

Submitted in partial fulfillment of the
requirements for the degree of
Doctor of Philosophy
at
Carnegie Mellon University
Department of Physics
Pittsburgh, Pennsylvania

Advised by Professor Robert M. Suter

February 9, 2022

Abstract

The ability to predict the performance and behavior of metals and other polycrystals in different conditions has huge impacts in real life. Besides phenomenological studies, finding the relationship between material microstructure and macroscopic properties is also indispensable, which relies on modern characterization techniques and complex computational tools. This thesis describes some recent developments of the computational tools for microstructure reconstruction and analysis. The grain coarsening phenomenon is studied in an α-phase Iron sample. We designed a new method to determine grain boundary energies (GBE) from triple junction geometries. The synchrotron based imaging technique Near-field High Energy X-ray Diffraction Microscopy (nf-HEDM) is extended to reconstruct intragranular strains. Meanwhile, A neural network based method is developed for Electron Backscatter Diffraction (EBSD) indexing, which is another popular characterization technique.

Acknowledgments

I would like to first express my gratitude to the members of my thesis committee, Professor Armand J Beaudoin, Professor Michael Widom, Professor Gregory Rohrer, and my advisor Professor Robert M Suter. I greatly appreciate their willingness to spend their valuable time giving feedback and advice, which greatly improved the quality of this work.

Special thanks to my advisor Professor Robert M Suter. He gives me the opportunity to work with him and meet with many other highly skilled people in this intriguing research area. Professor Suter, as one of the pioneers in the development of High Energy X-ray Diffration Microscopy, has invaluable insight into this technique. He and my colleague He Liu have helped me tremendously for learning the experimental details and reconstruction algorithms of nf-HEDM, as well as developing the GPU accelerated reconstruction algorithm for intragranular strain reconstruction.

I also owe a debt of gratitude to Professor Gregory Rohrer for educating me over the years, including most of my knowledge about the grain boundary theories and the computational tools for analyzing grain boundary data. All the works about grain boundary energy and grain coarsening in this thesis would not exist without his guidance.

I would also like to acknowledge Dr. Reeju Pokharel, who mentored me at Los Alamos National Laboratory in the 2018 summer when I interned there. Dr. Pokharel is an experienced and talented researcher, she taught me plenty when we worked together on the machine learning methods for EBSD indexing.

I am also indebted to many other individuals. Dr. Tugce Ozturk, Dr. Joel Bernier, Dr. Peter Kenesei, Dr. Jun-Sang Park, Dr. Paul Shade and Dr. William Musinski advised me patiently during my first few beamruns. Professor Armand Beaudoin, Dr. Kamalika Chatterjee and Dr. Jonathan Lind provided preliminary analysis for the strain of the Ti7Al sample, which is used in this thesis. Professor Anthony Rollett and his students Rachel Lim and Christopher Kantzos are of great help to me on materials science. Professor Adam Morawiec and his student Krzysztof Glowinski offered relevant codes and many important helps when we were developing the method for determining grain boundary energies. Dr. Siddharth Maddali reconstructed and registered the microstructure of the α-phase Iron sample, which is the basis for the grain coarsening analysis in this thesis. I must also thank Dr. Xiaoting Zhong, Aditi Bhattacharya and Xiaoyao Peng, with whom it was often helpful to talk through problems.

Contents

List of Tables

List of Figures

Chapter 1

Introduction

The work presented in this thesis is based on three published papers and one submitted manuscript that is under review. The references are as follows:

1. **Yu-Feng Shen**, Reeju Pokharel, Thomas J Nizolek, Anil Kumar, and Turab Lookman. Convolutional neural network-based method for real-time orientation indexing of measured electron backscatter diffraction patterns. *Acta Materialia*, 170:118-131, 2019. (https://doi.org/10.1016/j.actamat.2019.03.026)

   This paper is reproduced in Chapter 5.

2. **Yu-Feng Shen**, Xiaoting Zhong, He Liu, Robert M Suter, Adam Morawiec, and Gregory S Rohrer. Determining grain boundary energies from triple junction geometries without discretizing the five-parameter space. *Acta Materialia*, 166:126-134, 2019. (https://doi.org/10.1016/j.actamat.2018.12.022)

   This paper reproduced in Chapter 3.

3. **Yu-Feng Shen**, Siddharth Maddali, David Menasche, Aditi Bhattacharya, Gregory S Rohrer, and Robert M Suter. Importance of outliers: A three-dimensional study of coarsening in α-phase iron. *Phys. Rev. Materials*, 3: 063611, 2019. (https://doi.org/10.1103/PhysRevMaterials.3.063611)

   This paper reproduced in Chapter 2.

4. **Yu-Feng Shen**, He Liu, Chen Zhang, and Robert M Suter. Extending near-field High Energy Diffraction Microscopy: accelerated reconstructions and voxel-based strain tensors. *Current Opinion in Solid State and Materials Science* (submitted).

   This manuscript is reproduced in Chapter 4.

1.1 Background

Polycrystalline materials are solids which are composed of many single crystals (called grains) each with different orientations, shapes and even phases. The positions, sizes, shapes, orientations and phases of all grains are termed microstructure of the polycrystal. Metals and other polycrystals are widely used in modern society, examples range from buildings, bridges, to engine blades. Therefore, development of new metals, understanding their properties and control their behavior in different circumstances, are always important research areas and will have huge impacts on economy and human condition. It is well known that the macroscopic properties of polycrystals do not only depend on composition but also microstructure. So, people always endeavor to find physics-based models to explain the metal behaviors in thermal treatment (like recrystallization and grain coarsening phenomena), and their mechanical performance (like fatigue and cracking phenomena). Understanding the fundamental theories and having more accurate models will significantly benefit materials discovery and engineering.

Measuring the microstructures and observing their responses to thermal and mechanical treatments are essential to validate those theories and models for polycrystals. These valuable data sets have become available recently by virtue of the substantial progress in the characterization techniques. Among them, a technique called near field High Energy Diffraction Microscopy (nf-HEDM) utilizes the penetrative high energy X-rays ($10\,\text{keV} \sim 100\,\text{keV}$) as a non-destructive probe and reconstructs the microstructure from the diffraction images. As expected, sophisticated numerical and computational tools are necessary in the reconstruction procedure and to take advantage of these data sets, and these are the major topics to be covered in this thesis.

1.2 Thesis Outline

Our discussion of computational methods in reconstructing and analyzing polycrystalline microstructures consists of four parts. Chapter 3 and Chapter 2 focus on the conputational methods for analyzing microstructure, Chapter 4 and Chapter 5 focus on the computational methods for reconstructing microstructures from experimental datasets.

Chapter 2 provides a case study for grain coarsening in an α phase iron sample. The three dimensional microstructure of this sample was measured before and after annealing using high energy x-ray diffraction microscopy by Siddarth Maddali, a former graduate student in our group [5]. 4,971 grains that are entirely inside the sample are segmented in the initial state and 3,905 remain after annealing. A matching procedure was used to track 3,299 grains between the two states while the remainder were either consumed by neighbors or the tracking algorithm failed to correlate them. During the single annealing treatment, the average grain volume increased by 13%.

Statistical analysis in each state yields subtle changes in the grain size and nearest neighbor number distributions. Correlating topological features with volume changes between states, the average behavior is seen to be consistent with an isotropic model of curvature driven coarsening, but the dispersion of volume changes in each topological class is comparable to the overall trend in the average behaviors.

Chapter 3 describes the numerical methods for determining the grain boundary energy distribution (GBED) from the microstructures of polycrystalline materials. The methods assume that triple junctions (the region where three grain boundaries intersect at a line) are in local mechanical equilibrium, which is described by the Herring equation, and can be expressed using the Hoffman-Cahn formalism of the capillarity vector. This chapter reviews some basics about the five-parameter space of grain boundaries, and then explains a conventional method for determining the grain boundary energies which is based on discretizing the five-parameter space. After that, we propose a new numerical method which minimizes the difference between similar boundaries in the dataset while obeying the equilibrium equation at triple junctions. The advantages of the new method are then demonstrated on synthetic data sets. An application to a MgO dataset is also presented.

Chapter 4 reviews the basics of X-ray diffraction and explains the experimental setup of nf-HEDM along with the forward modeling method, which is the algorithm that reconstructs microstructure from diffraction images. We extend this algorithm to reconstruct not only the orientation but also the strain in the 3D volume. This new reconstruction routine is then tested on synthetic data and applied to data from a Ti7Al sample.

Chapter 5 works on another commonly used technique for obtaining spatially resolved microstructural information from polycrystalline materials, Electron Backscatter Diffraction (EBSD). We have developed two convolutional neural network approaches based on domain transform and transfer learning to reconstruct crystal orientations from electron backscatter diffraction patterns. Our models are robust to experimentally measured image noise and index orientations as fast as the highest EBSD scanning rates. We demonstrate that the quaternion norm metric is a strong indicator for assessing the reliability of the reconstructions in the absence of the ground truth. We demonstrate the applicability of the current methods on a tantalum sample.

Chapter 2

Grain Coarsening in α-phase Iron

2.1 Introduction

Many condensed matter systems undergo coarsening processes in which the average cell size in a large ensemble increases over time as large cells intrude on and consume smaller cells. This process is typically driven by reduction in the total interfacial energy, and, thus the total interfacial area. Examples are as diverse as foams, [6, 7, 8] phase separating liquids and solids, and polycrystalline aggregates. [9, 10, 11] For fluid systems, all interfaces have the same structure and properties, so the driving forces for motion can be modeled with a single homogeneous interfacial tension and mobility. Curved boundaries are expected to move toward their centers of curvature since this results in reduced local boundary areas. This flattening of boundaries tends to lead to polyhedral domain shapes.

For the case of coarsening in polycrystalline microstructures, the homogeneity condition is broken due to anisotropic crystal properties which result in the energies and mobilities of crystal-crystal interfaces being dependent on both the relative crystal orientations and the local orientation of the interface normal. Thus, boundaries between crystals or grain boundaries are characterized on the mesoscale by five parameters: for example, three disorientation parameters defining the symmetry reduced relative orientations of crystal unit cells and two parameters that define the local interface normal relative to unit cells of the two crystals. These (or alternative) sets of five degrees of freedom define the "grain boundary character" (GBC) [12] and coarsening is expected to depend on the distribution (GBCD) and connectivity of the boundary types. Finally, it should be noted that the interface motions described here are expected to dominate microstructure and boundary evolution only after bulk (grain interior) defect densities and their associated bulk excess energies have been reduced to negligible values. However, local irreducible strain fields associated with grain boundaries may well influence boundary energies and mobilities.

Because microstructure plays a key role in determining the properties [13, 14, 15] of polycrystalline materials that are used throughout modern societies, coarsening or

"grain growth," has been studied experimentally and theoretically for many decades. [16, 17, 18, 19] For two dimensional systems, the basis for most theoretical and experimental investigations[20, 21] is the von Neumann-Mullins "$n-6$ rule"[10, 11],

$$\frac{dA}{dt} = \frac{\pi}{3} M\gamma(n-6), \tag{2.1}$$

where $\frac{dA}{dt}$ is the area changing rate of the "two dimensional grain", n is the number of grain sides, M is the mobility and γ is the excess energy per unit length of boundary. This predicts that cells with more than six sides (or neighbors) will grow while those with fewer than six sides will shrink and eventually disappear. The simple form of (2.1) results from the assumption of homogeneity of boundary properties (hence the single values of M and γ) and it assumes mechanical equilibrium at vertices which implies triple point vertex angles of 120°.

Palmer et al. [22] compared (2.1) with experimental observations of thin organic polycrystalline films and found significant deviations from the expected vertex angles but nevertheless found that the trend in average growth rates in each topological class agreed well; however, large deviations, of the same order as the overall trend, were observed within each class. One suggested cause of deviations from $n-6$ was the heterogeneity in boundary properties. Since the optical measurement did not determine crystal orientations, it was not possible to classify the boundaries.

More than 50 years after von Neuman's and Mullins' work, a rigorous three dimensional (3D) generalization of (2.1) has been obtained by McPherson and Srolovitz, [9] the "M-S relation,"

$$\frac{dV}{dt} = \frac{\pi}{3} M\gamma \left(\mathcal{M} - 6\mathcal{L}_{grain}\right), \tag{2.2}$$

where $\mathcal{M}$ is the total triple line length around the grain and $\mathcal{L}_{grain}$ is the mean width of the grain. [9] Again, this result is based on homogeneous, isotropic grain boundary properties and therefore on the expectation of uniform 120° dihedral angles at triple lines where three grains meet.

It is only within the past decade that experiments have begun to be able to watch internal three dimensional microstructures evolve over time. The key development has been the application of diffraction methods using high flux, tunable synchrotron x-rays. Spatially resolved diffraction techniques have been developed that are able to image microstructures in three dimensions including crystalline grain unit cell orientations, grain shapes and positions; the non-destructive measurements allow collection of images of volumes of interest in successive states of evolution. [23, 24, 25, 26, 27] These measurements yield novel data sets spanning large ensembles of grains and grain boundaries. Extraction of either statistical characteristics of grains or local characteristics such as individual boundary motions requires development of trusted computational tools and careful consideration of measurement resolution in both position and orientation degrees of freedom.

Two distinct data collection methods have been used in the above studies. Zhang et al. [28], and McKenna et al. [29] apply diffraction contrast tomography (DCT)

[26] using data collected at the European Synchrotron Radiation Facility. Sun et al. [30] use a commercial, laboratory based DCT system. [31] Work at the Advanced Photon Source has applied near-field high energy diffraction microscopy (nf-HEDM) [24, 32, 33] which is an implementation of 3DXRD. [25] While nf-HEDM uses a line focused beam to illuminate a series of quasi-two dimensional cross-sections which are then stacked to yield three dimensional grain geometries, DCT uses a "box" beam to illuminate a volume of microstructure. Reconstruction approaches are quite different [4, 26] but, for the well ordered grain structures of interest to coarsening, results have comparable resolutions of grain orientations and grain boundary positions.

Recent observations of coarsening using the above diffraction based methods include studies of iron, [28, 30, 5] nickel, [34, 35] and strontium titanate. [36] Similar work was carried out using absorption tomography combined with grain boundary segregation in a titanium alloy. [29] Real time growth of individual selected grains based on evolution of a single spatially resolved Bragg peak have also been recorded. [37] Direct comparisons to computational phase field or finite element models have been carried out in a small number of cases. [29, 36]

Here, we present statistical analysis of data, also studying alpha iron, first presented in the thesis of S. Maddali. [5] This data set comprises a larger statistical sampling of grains in than previous work, by roughly a factor of 10, and therefore yields improved statistical distributions, but only two time steps are measured compared to 15 in [28]. Further work addressing boundary motions and making comparisons to computational models of evolution can be expected to follow in all of these cases.

2.2 Methodology

2.2.1 Sample preparation and data collection

The sample material was electrolytically grown high-purity iron (obtained from the Center for Iron and Steelmaking Research at Carnegie Mellon University) and with an elongated grain structure. At temperatures below 912 C, iron exists in its [-allotropic] alpha phase form, which has a body-centered cubic (BCC) crystal structure. The requirement of (statistically) isotropic grain boundary inclinations required the destruction of the elongated grain structure followed by regrowth through annealing and quenching. Accordingly, the sample was rolled in a mill from an original thickness of about 5 mm to about 1 mm and annealed in a tube furnace for two hours at 600 C in a forming gas atmosphere (N_2+3%H_2) and then quenched. A sample of approximate dimensions $1 \times 1 \times 30$ mm^3 was cut from this material.

Measurements were performed using the nf-HEDM apparatus in the E-hutch of beamline 1-ID at the Advanced Photon Source at Argonne National Laboratory. [24, 33] A 65.351 keV x-ray beam was focused vertically to a ≈ 1.5 μm full width at half maximum line beam. The beam size was limited in the horizontal direction to 1.5 mm using slits. As the sample was continuously rotated about a vertical

axis perpendicular to the beam plane, images of diffraction spots were collected over successive angular intervals of width $\delta\omega = 0.25°$. The total rotation range was 180° over which typical orientations generate roughly ≈ 180 observed Bragg peaks. The high resolution imaging detector used a scintillator (LuAG) whose scintillation light was optically coupled to a 2k×2k CCD camera; using a 5X objective lens, the effective pixel size was 1.54 μm. This rotation procedure was repeated at two different sample-to-detector distances and the data collection was repeated for multiple equally-spaced sample layers by translating the sample perpendicular to the beam; in this manner diffraction data from an entire volume was collected. Here, 65 layers with $3\mu m$ spacing were measured, so a total volume of about 1 mm × 1mm × 0.195 mm^3 was measured. After the first volume measurement, the sample was removed from its mount and annealed in a tube furnace at 600 C for half an hour again using a forming gas atmosphere. The sample was replaced in the HEDM apparatus and the same volume of the sample was measured again. For further details of the sample and procedure, the reader is referred to the Ph.D. thesis of Maddali [5].

2.2.2 nf-HEDM reconstruction, volume registration and grain segmentation

The reconstruction of sample microstructure is performed with the forward modeling software *IceNine* [4, 24] after image analysis that separates diffraction signals from background. [38] A critical feature of the image analysis is the use of a Lapacian-of-Gaussian edge detection algorithm that has been shown to yield diffraction spot shapes reflective of projected images of each diffracting grain cross-section. [39] For each measured layer, the reconstruction was performed on a simulation space which is larger than the illuminated sample cross-section. A mesh of $s = 1.56$ μm side-length equilateral triangles spanned the simulation space; each triangle encloses an area corresponding to a square with side length 0.581 μm. In each layer, there are about 10^6 triangular voxels. For each triangular element, the assigned orientation is that which generates the maximum overlap between simulated and experimental diffraction spots. For mesh elements near grain boundaries, even at the optimal orientation, the simulation will miss some diffraction spot edges due to detector discretization and image analysis noise; this leads to a decreased confidence or overlap metric. [24] Similarly, diffraction signals from two (or more) neighboring grains' orientations can each generate finite overlap of simulated diffraction. The optimization algorithm simply picks the orientation with maximal overlap for each mesh element. The large number of Bragg peak observations has the effect of signal averaging over the various noise sources and leads to ~ 1 μm accuracy in relative grain boundary positions within the reconstruction planes. [39]

The open source software package, *DREAM.3D*, [40] was used to segment the reconstructed data into individual grains. Before using *DREAM.3D*, the data were down-sampled from the set of reconstructed layer-by-layer *.mic* files to a single *.h5ebsd*

Table 2.1: Numbers and dimensions of grains in two sample states.

State	Total	Internal	Internal Grains		
			$V_T(10^7\mu\text{m}^3)$	$\langle V\rangle(10^4\mu\text{m}^3)$	$D_{eff}(\mu\text{m})$
0	10,927	4,971	5.96	1.20	28.4
1	9,224	3,905	5.28	1.35	29.6

file, with $3 \times 3 \times 3$ μm^3 cubic voxels; orientations were assigned as that of the nearest voxel in the *.mic* files. The orientation of each voxel is compared to its neighbors (in 3D) and contiguous sets of voxels with orientations that differ by $\leq 2^\circ$ were grouped together as grains; the minimum size of accepted grains was set to eight voxels. Those groups with fewer than eight voxels (i.e., < 216 μm^3 or < 7.4 μm spherical equivalent diameter) were treated as gaps in the microstructure. Less than 0.1% of voxels were in such gaps; gaps were then eliminated by dilating neighboring grains uniformly using a procedure in *DREAM.3D*. The aggressive down sampling described here yields a hard lower cutoff in the grain size distribution at a level above the expected minimum size to which the measurement is sensitive.

The analysis below is restricted to grains that are entirely inside the measured volume in both states. First, any grain whose centroid lies outside the black boundary in Fig. 2.1 is removed to avoid surface effects. Further, any grain that intersects the top or bottom edge of the reconstructed volume is also excluded from analysis. This method is similar to that used in [41] to avoid statistical bias from cut-off grains; however, as discussed below, the procedure also preferentially eliminates large grains. Global statistics are shown in Table 2.1. V_T is the total volume occupied by internal grains, $\langle V\rangle$ is the average grain volume, and $D_{eff} = 2\left(\frac{3}{4\pi}\langle V\rangle\right)^{1/3}$, is the average spherical equivalent diameter (SED). Note that D_{eff} is the SED of a grain with the average volume, not the average of SED values. The nominal trimmed measured sample volume is $\approx 1.3 \times 10^8 \mu\text{m}^3$ in both states.

Because it is not possible to re-mount the sample in exactly the same position and orientation after annealing, volume registration was required in order to correlate local properties before and after annealing. Registration was done in two steps [5]:

1. Determine the single rigid-body translation and rotation that aligns a single layer in the post-anneal volume with its corresponding layer in the pre-anneal volume, and apply this transformation to all layers in the post-anneal volume. This transformation was determined "by eye."

2. Pick one grain that is present in both volumes and rotationally align the entire post-anneal volume such that the two orientations of this grain coincide.

After this process, the angular alignment of the two volumes is within $\approx 0.1^\circ$ which is the expected experimental resolution. Figure 2.1 shows the final 3-D registered

reconstructions of the α-iron sample before and after annealing.

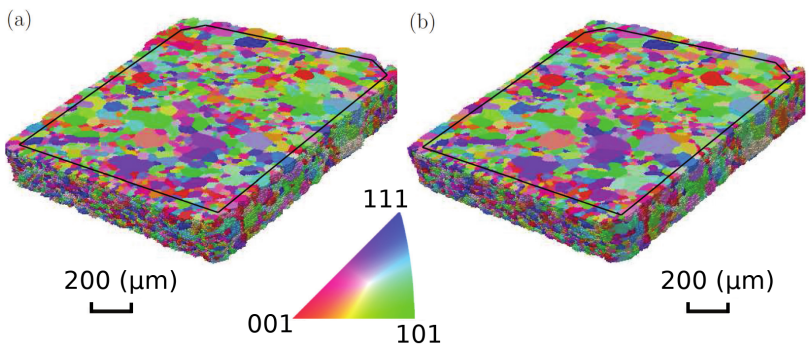

Figure 2.1. The measured sample volume, (a) before and (b) after annealing. Black lines indicate schematically a trimming of the sample edges used to avoid the damaged surface region that has anomalously small grains. Colors are according to the inverse pole figure key shown and is referenced to the normal direction to the square cross-section.

2.2.3 Grain matching

Algorithm 1: Grain matching

parameters: $MisorLim$, $VolRatLim$, $DistDiaLim$

for *grain* $A_i \in$ *State 0* **do**
  $D_A \leftarrow$ Diameter of A_i;
  $S_A \leftarrow$ Centroid of A_i;
  $V_A \leftarrow$ Volume of A_i;
  for *grain* $B_j \in$ *State 1* **do**
    $S_B \leftarrow$ Centroid of B_j;
    if $|S_A - S_B| \leq DistDiaLim \times D_A$ **then**
      $V_B \leftarrow$ Volume of B_j;
      if $\frac{1}{VolRatLim} \leq V_A/V_B \leq VolRatLim$ **then**
        if *Misorientation of* A_i *and* $B_j \leq MisorLim$ **then**
          Match B_j to A_i;
        end if
      end if
    end if
  end for
end for

To study coarsening dynamics, it is necessary to identify the same grain in different time step snapshots. For each grain in one state, we search every grain within a

surrounding volume of the other state and, if both the misorientation angle and volume ratio are within specified thresholds we call the pair a match. A detailed description is provided in Algorithm 1.

To ensure robustness, grain matching is performed in both directions; that is, for each grain in the initial state, we search for the same grain in the final state and for each grain in the final state we search for the same grain in the the initial state. Only matched pairs that are the same in both directions are kept for further analysis. The values $0.5°, 10, 2$ were chosen as *MisorienLim*, *VolRatioLim*, *DistToDiaLim*, respectively. These relatively strict limits result in 3299 pairs of matched grains. 30.2% of grains in the initial state are not matched in the annealed state whereas only 12.4% of final state grains are not located in the initial state. This disparity is largely attributed to small grains being consumed by larger ones and thus not existing in the annealed state. Assuming that new grains are not nucleated, the 12.4% missing in the reverse matching must be characteristic of the difficulty in matching small grains (many of which exist in both states since some grains are always shrinking and disappearing). Further characterization of matched and unmatched grains is given in 2.3.3.

Figure 2.2 shows some examples of matched grain pairs. It is seen qualitatively that, in most cases, grain boundaries move toward their centers of curvature as expected for capillarity driven growth.

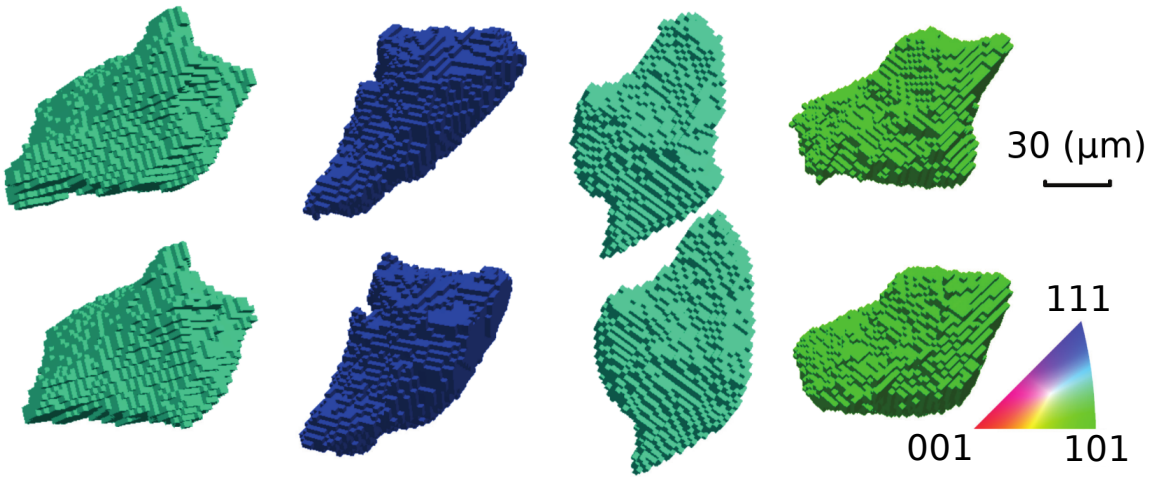

Figure 2.2. Examples of matched grains, top row before annealing and bottom row after annealing. The roughness of the surfaces is due to the discrete voxel size; no smoothing has been performed. The side length of each cubic voxel is 3 μm. Colors correspond to the crystal unit cell orientations according to the inverse pole figure scheme illustrated at bottom right.

2.3 Results

A variety of data sets characterizing three dimensional statistics of grains in specific states or "snapshots" are in the literature, for example, see [28, 41]. Non-destructive measurements allow comparisons of such statistics in multiple snapshots of the same material volume. The next section presents analyses that do not require tracking of individual grains but which do require the restriction to grains that are entirely enclosed within the sample and the measured volumes. The following section presents statistical analyses of the evolution of individual grains.

2.3.1 Statistical distributions of grain characteristics

Grain size distributions. The number of internal grains decreased from 4971 to 3905 with annealing; as listed in Table 2.1 this corresponds to an average grain volume increase from $\approx 11,993$ μm^3 to $\approx 13,533$ μm^3 or a $\approx 13\%$ volume increase or a 4% increase in linear dimension.

Individual grain volumes are extracted from the data sets as $V_g = V_{vox} N_g = (27\ \mu\text{m}^3)\ N_g$, the volume per voxel (see Sec. 2.2.2) times the number of voxels assigned to the grain. As shown in Fig. 2.3a, the measured grain volumes in each state span more than three decades even with the lower end cutoff at $N_g = 2^3 = 8$ contiguous voxels. Similarly, the large number of grains in the data set allows the probability density to be resolved over at least four decades. The observed distribution of volumes is monotonically decreasing. A more conventional "size distribution" in terms of spherical equivalent radii is shown in Fig. 2.3b; not surprisingly, this distribution extends over about one order of magnitude as seen in numerous other data sets. [28, 29, 41] The conservative small size cut-off used in this analysis results in the plot terminating just below the peak value. Error bars in both plots are derived from Poisson counting statistics related to the number of entries in each displayed bin. We next discuss the interpretation of the distributions and the relation between them.

Since the grain volume is a continuous variable, an appropriate way to characterize the distribution is with a probability density function, $P(V)$, where $P(V)dV$ is the probability of a grain having size V within the interval dV. In a large ensemble of N grains, the number within dV is $dN = NP(V)dV$. The goal is to approximate the distribution, $P_\infty(V)$, that would be observed in a very large (or infinite) ensemble. Fig. 2.3a plots empirical approximations to this distribution function for each of the measured states: $P_N(V) \approx \frac{\Delta N}{N}\frac{1}{\Delta V}$ with ΔN being the number of grains within ΔV of the nominal volume and N the total number of grains in each state. In Fig. 2.3a, bin widths are chosen such that $\frac{\Delta V}{V} \approx 0.26$ (more precisely, $\frac{V+\Delta V}{V} = 10^{0.1}$) which assures that the apparent $P_N(V)$ is roughly linear over each bin interval and the differential approximation is reasonable. $P_N(V)$ is seen to be monotonically decreasing and changes only slightly during the observed coarsening. From this logarithmic plot, it is clear that the measured $P_N(V)$ does not follow a simple power law form. The

observation that there are many grains with small volumes is reasonable since, during coarsening, there are always grains that are tending to zero volume as they are being consumed by larger grains.

Fig. 2.3b is a simple histogram of reduced spherical equivalent radii. Note, however, that volume is the measured physical quantity and the grains are far from being spherical; the radius, while being easily computed from the volume measurement and convenient for some purposes (see below), is not a physical characteristic of the grains. Nevertheless, Fig. 2.3b shows an apparent peak around $R/\langle R\rangle \sim 0.4$ which is qualitatively consistent with other data sets, see, for example, [41, 28, 30, 42] Figs. 2.3a and b are consistent with each other since the probability density functions for radius, P_r, and volume, P_V, are related by $P_r(r) = 4\pi r^2\ P_V(V(r))$. The factor of $4\pi r^2$ is present due to the fact that the volume interval covered by dr scales with the surface area of the sphere.

At least two biases could be present in the size distributions shown in Fig. 2.3. The maximum grain size included is $\approx 5 \times 10^5\ \mu\text{m}^3$ which corresponds to a spherical equivalent diameter (SED) of 100 μm which is comparable to the vertical size of the measured volume ($H_e = 195\ \mu$m). The center of such a spherical grain would have to be well centered in the measured volume in order to not be eliminated from the statistics used here. A rough correction that accounts for the reduction in volume available for the center of mass of a spherical grain of diameter D is

$$P_\infty(V)dV \approx \frac{dN}{N}\frac{1}{(1-\frac{D}{L_e})^2\ (1-\frac{D}{H_e})}, \tag{2.3}$$

where $D = 2\left(\frac{3}{4\pi}V\right)^{1/3}$ and L_e is the measured square cross section side length and H_e is the height of the measured volume. Open symbols in Fig. 2.3 show these corrected values for the post-annealing state. As seen in Fig. 2.2, typical measured grains are not particularly spherical and this may increase or decrease the appropriate correction factor depending on anisotropy relative to the shape of the anisotropic measured volume.

The second possible bias in Fig. 2.3 occurs at small grain sizes where diffraction signals may become weak and lead to reduced sensitivity. The cutoff in grain size described in Sec. 2.2.2 helps to assure that this effect is not present or not large in the distributions shown. In fact, using a less aggressive cutoff shows a continued increase in the number of observed grains below the volume limit in Fig. 2.3a.

Over most of the volume range, the shape of Fig. 2.3a is essentially unchanged while in the large grain limit a subtle (on the logarithmic scale) increase is seen which corresponds to the increased average grain volume. The finite volume correction tends to make the logarithmic plots more power-law like, but there remains significant curvature over the entire three and a half decades of volume variation. Without additional anneal states, it is not possible to speculate on a trend toward a power law behavior.

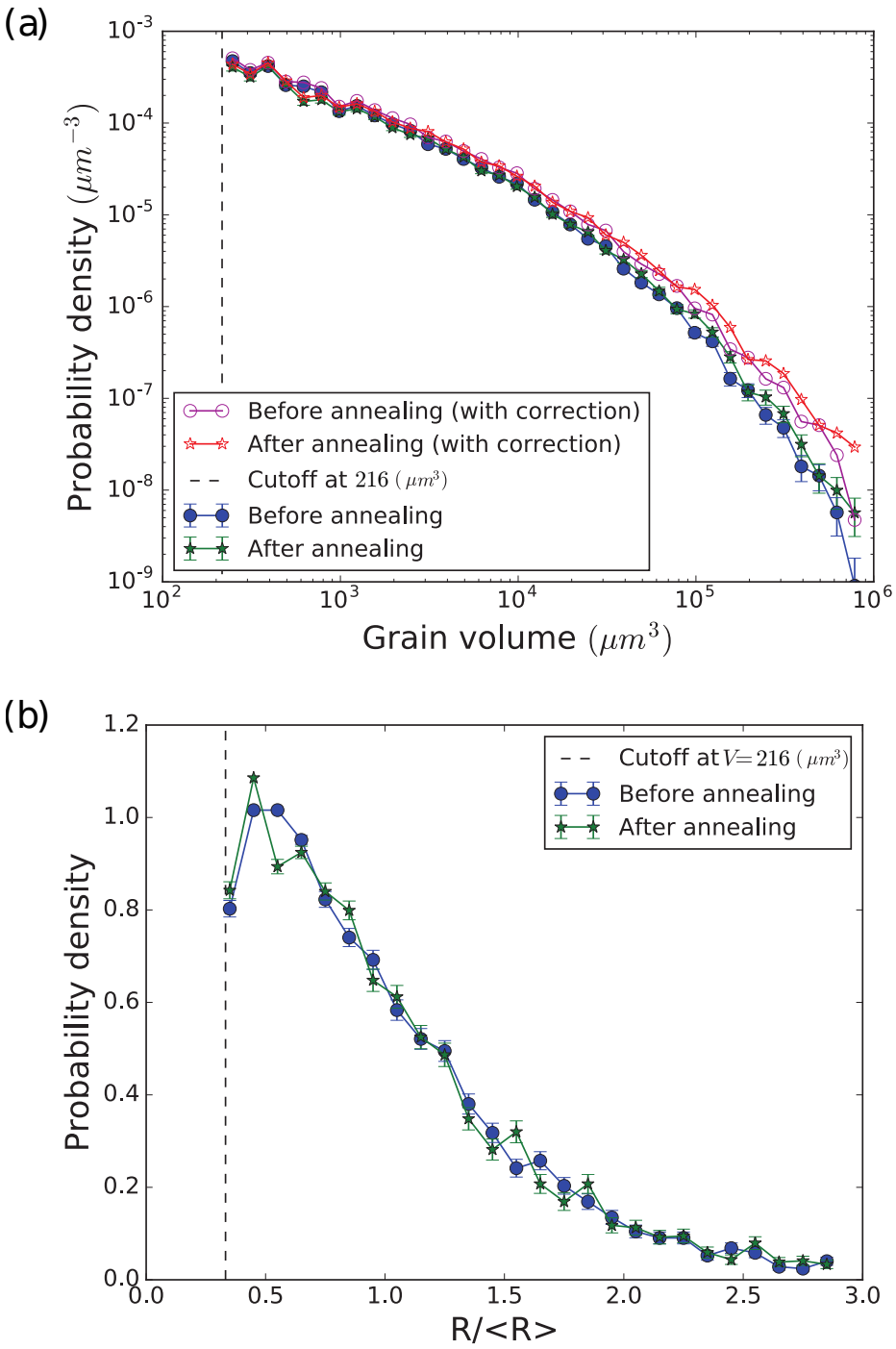

Figure 2.3. Estimated grain volume probability densities, $P(V)$, with units of μm^{-3}, in each of the two measured states. Closed symbols are directly computed from the data while open symbols are corrected by (2.3). b) The reduced radius distributions corresponding to (a) without the finite volume correction. See the text for discussion.

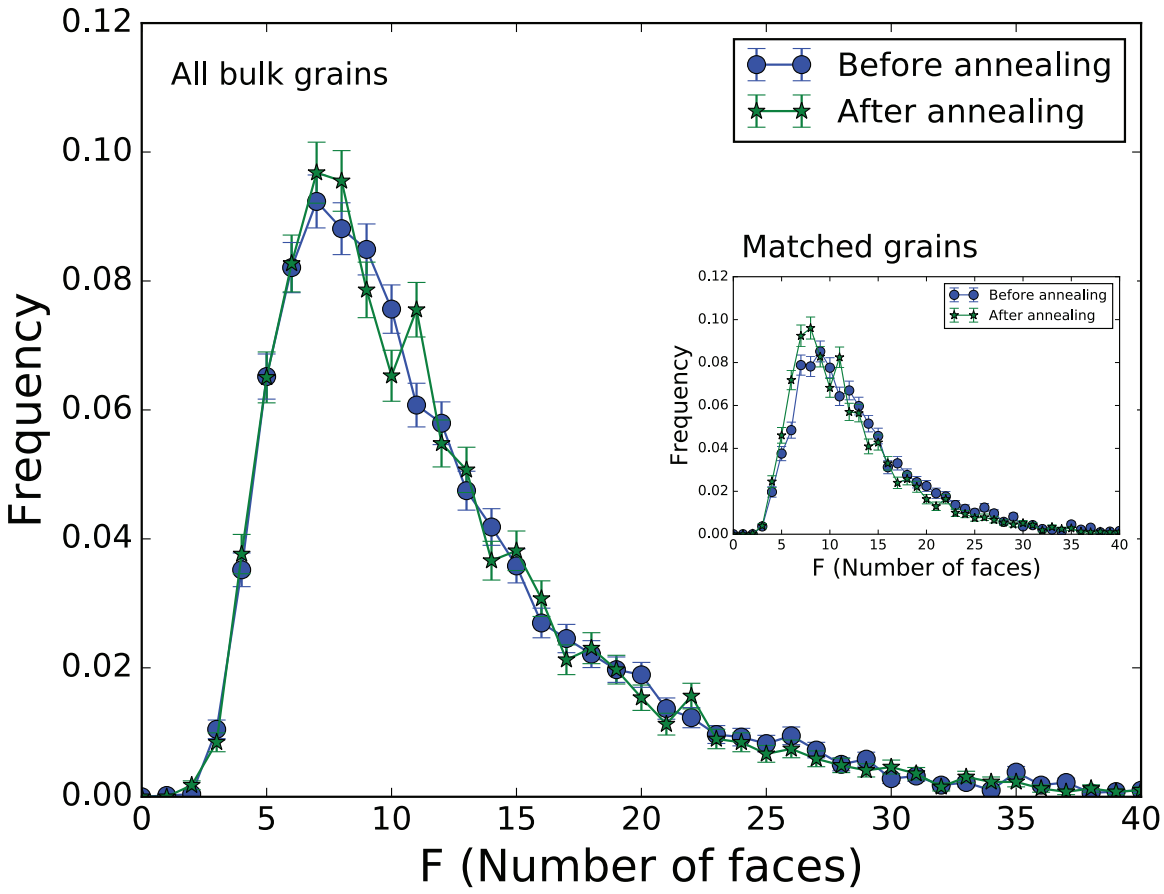

Figure 2.4. The distribution of the number of faces or nearest-neighbors per grain in each measured state. The frequency is the number of occurrences of F, N_F, divided by the total number in each state. Error bars are $\sqrt{N_F}/N_{tot}$. There exist (but are not shown) grains that have values as high as $F = 80$. The inset shows the corresponding distribution for the 3299 matched grains whose evolution is discussed in Sec. 2.3.2.

Number of faces distribution The number of faces or nearest neighbors, F, of a grain is a fundamental topological quantity. [10, 11, 43] The distribution of F over the measured grains is shown in Fig. 2.4. Note that the inclusion of the large number of small, unresolved grains would increase the frequency of small neighbor numbers if they could be reliably included and a similar effect may reduce the large F limit of the distribution due to the finite measurement volume. For the included grains, the average number of faces is $\langle F_0 \rangle \approx 12.0$ in the initial state, and $\langle F_1 \rangle \approx 11.8$ in final state; the peak is at $F \approx 7.5$ in both states. This distribution, like the volume distribution, is essentially unchanged under the annealing. There is a long tail containing a small number of grains having as many as 80 neighbors (not shown). Not surprisingly, the grains in the tail of this distribution are also in the large grain tail of the volume distribution. The shape of the distribution shown here is similar

to those seen in Fig. 4b of Zhang et al. [28]; counting statistics do not allow detailed comparisons to their evolving distributions. Additional statistics are presented in 2.3.3.

2.3.2 Statistical characterization of grain evolution

Changes in grain size are expected to correlate with topological characteristics of grains and their neighborhoods. While the average behaviors shown below appear consistent with the isotropic theory, the variations within each topological class are found to be at least comparable to the overall variation in the average behavior.

Dependence on number of grain faces As a first statistic, consider changes in the spherical equivalent diameters of grains as a function of the grains' number of nearest neighbors. The spherical equivalent diameter is $D = 2\left(\frac{3}{4\pi}V_g\right)^{1/3}$ and we use subscripts, 0 and 1 for the initial and annealed states. Note that most grains are far from spherical but D can be used as a linear characterization of size, growth, or shrinkage.

Fig. 2.5(a) shows diameter differences, $\Delta D = D_1 - D_0$, for each of the 3299 matched grains as a function of F_0, the number of faces in the initial state. Since F_0 correlates with grain size and large grains are expected to grow, a positive correlation of ΔD with F_0 is expected. The appropriate trend in the mean is apparent in the figure, apart from the upturn at small face numbers (see below). However, for grains in each class, the standard deviation of diameter changes is comparable to the overall variation in the mean. The large standard deviations at $F_0 = 46$ and 48 and the lack of standard deviations at larger numbers are due to the fact that only one or a few grains exist at these face numbers. It is apparent that at each value of F_0, some grains grow while others shrink. In spite of the fact that large F_0 correlates with large grains, this metric alone is not predictive of even the binary question of growth versus shrinkage of a particular grain.

The upturn in ΔD at small F_0 may be counter intuitive, but can be attributed to the fact that only grains that survive the annealing are included. Many small grains (typically with small F_0) should contribute $\Delta D = -D_0$. This bias can be removed in a statistical way. As stated above, there are 30.2% of initial state grains that are not paired in the forward matching and 12.4% in backward matching. Again assuming no nucleation, 12.4% is the estimated error rate in matching and the remaining 17.8% (885 grains) should be roughly the number of grains that disappeared. We randomly choose 885 of the forward matching unpaired grains and assume that they had $\Delta D = -D_0$. Including these yields Fig. 2.5(b) with intuitively reasonable average behavior of shrinking grains with small F_0 and growing grains at large F_0.

The mean growth curves in Fig. 2.5 cross zero at $F_0^{stagnent} \approx 19$, larger than $\langle F \rangle \approx 12$. Fig. 2.4 shows that about 80% of grains have $F < F_0^{stagnent}$; nevertheless, only roughly 50 % of grains shrank and 50% grew. A recent isotropic phase-field

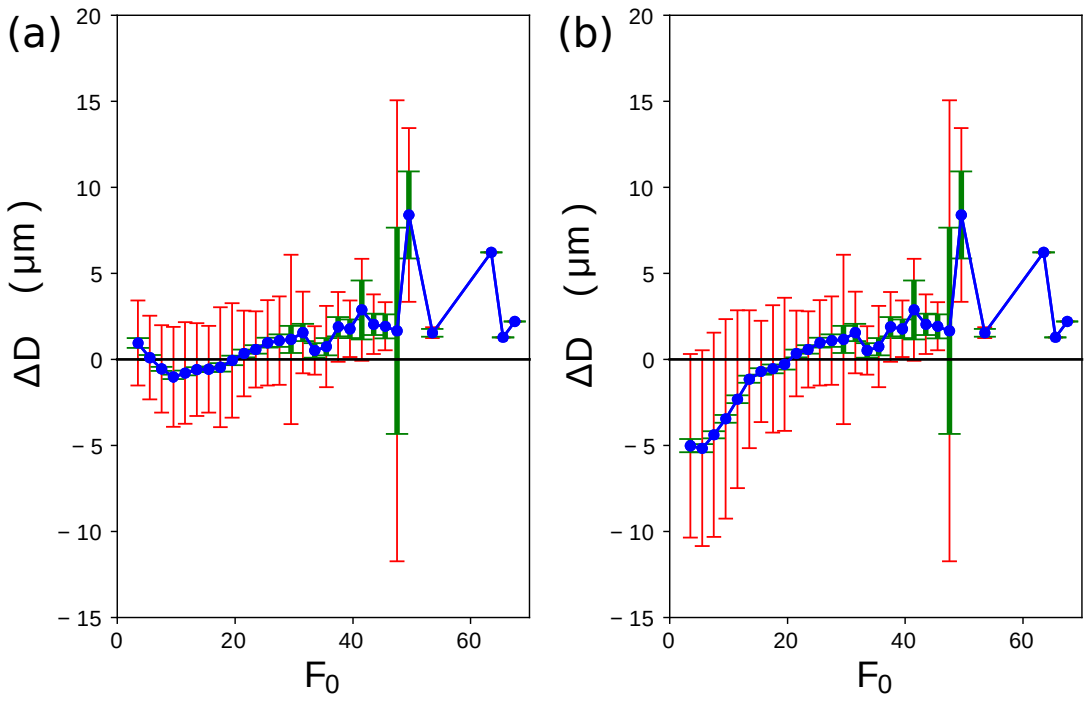

Figure 2.5. Statistics of diameter changes for grains with different numbers of nearest neighbors (or faces) in the initial state. Pairs of face numbers have been binned for clarity. The mean (blue points) and standard deviations (red error bars) are shown for each grain class. Green error bars are the standard deviations of the estimated mean values, which are $\frac{1}{\sqrt{n}}$ times the standard deviations (red error bars), where n is the number of grains in each bin. (a) includes only matched grains whereas (b) also includes a statistically estimated correction for grains that disappear and therefore have $\Delta D = -D_0$ (see text for discussion).

simulation [42] yields both a zero average growth rate and an average face number of ≈ 15 for a variety of initial grain sizes and face number distributions and at different time points. These distinctions are discussed in Sec. 2.4.

Dependence on grain neighborhoods Under the assumption that grain boundary interface energies and mobilities are independent of the five crystallographic parameters specifying grain boundary character, grain growth process should be described by the MacPherson-Srolovitz model. [9] Mullins and von Neumann [10, 11] showed that the evolution of grain boundary interfaces is driven by the local mean

curvature of that boundary, and as a result, the total volume growth rate is given by

$$\frac{dV}{dt} = V^{1/3} M \gamma g \tag{2.4}$$

$$g = -\frac{1}{V^{1/3}} \int_{\text{Faces}} \left(\frac{1}{R_1} + \frac{1}{R_2} \right) dS \tag{2.5}$$

where M is a mobility constant for the grain boundary, γ is the excess interfacial energy per unit area and g represents the normalized integral mean curvature of the grain faces. R_1 and R_2 are local radii of curvature of the boundary and dS is an element of interfacial area. It is based on (2.4) and (2.5) that MacPherson and Srolovitz were able to obtain (2.2).

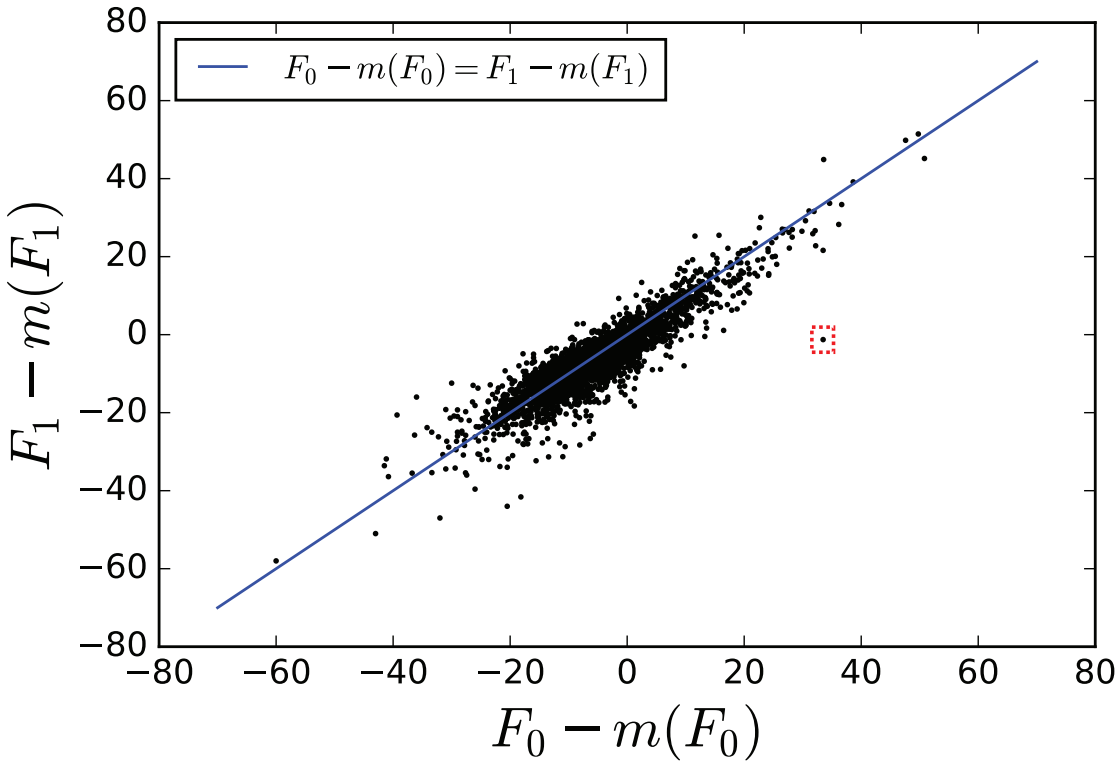

Figure 2.6. Changes of the excess grain face number. Each point represents an individual grain. See discussion in the text. The outlier in the red box is discussed below in Sec. 2.3.4

To compare with our experimental data, Eq. (2.4) is converted to integral form, $\Delta V^{2/3} = \frac{2}{3} \int M \gamma g \, dt$. Earlier work by Rowenhorst et al. [41, 44] showed empirically that g is, at least in an averaged sense, proportional to $F - m(F)$, where F is the number of faces of a grain and $m(F)$ is the average number of faces of that grain's nearest neighbors; we refer to $F - m(F)$ as the "excess face number." As shown in

Fig. 2.6, for most of the grains, the value of $F - m(F)$ does not change dramatically during the annealing. For grains with a given value in one state, the mean value in the other state is the same within a standard deviation of ≈ 4 . We infer that there should be a roughly linear relation between g and $F - m(F)$ and therefore that

$$\Delta V^{2/3} = V_1^{2/3} - V_0^{2/3} \propto \int [F - m(F)] \; dt \approx (F_1 - m(F_1)) \; \Delta t. \tag{2.6}$$

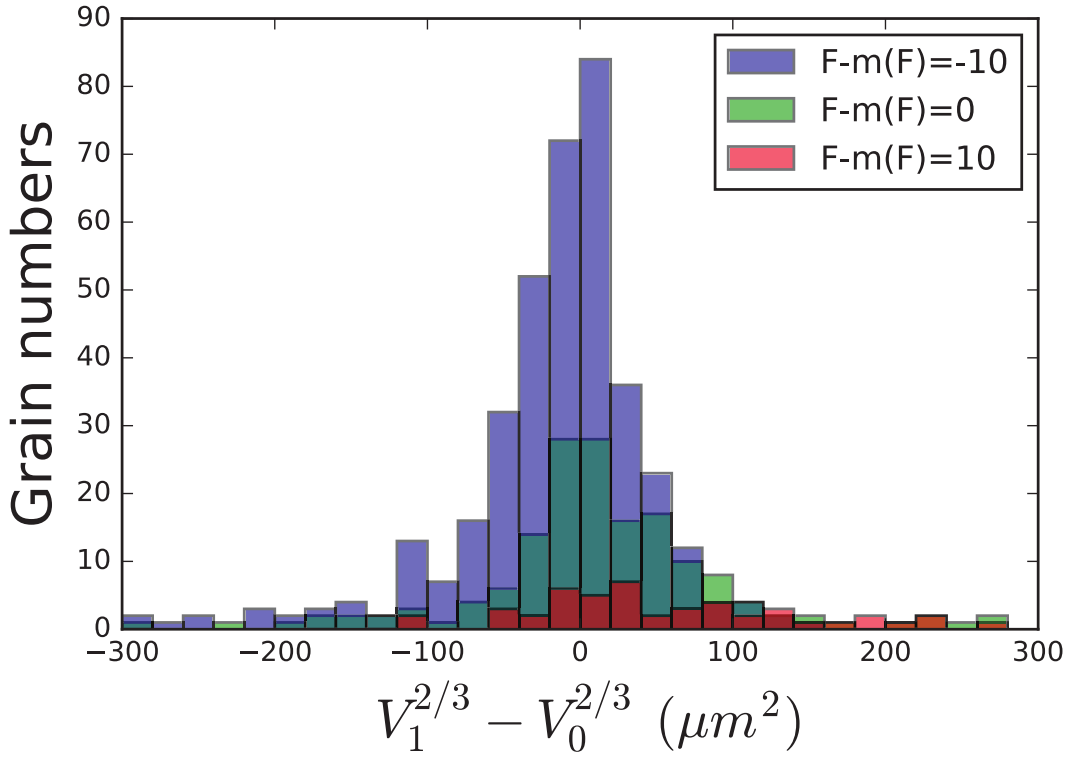

Figure 2.7. Histograms of $\Delta V^{2/3}$ in (2.6) for three excess face numbers, $F - m(F)$. Here, $F = F_1$ is taken from the annealed state.

Fig. 2.7 demonstrates that the isotropic prediction (2.6) is not obeyed since for given values of $F - m(F)$, a wide distribution of values of $\Delta V^{2/3}$ is observed. On the other hand, there is a subtle shift of the histograms toward positive $\Delta V^{2/3}$ as the excess face number increases. It is also clear from these histograms that the total number of grains (integral under the curves) decreases strongly with increasing excess face number.

Fig. 2.8 shows the means and standard deviations of distributions like those shown in Fig. 2.7 over a broad range of excess face number. The range $-20 \leq F_1 - m(F_1) \leq 20$ corresponds a range over which the number of entries is large enough that the statistical result is robust. Remarkably, the mean values of the broad distributions

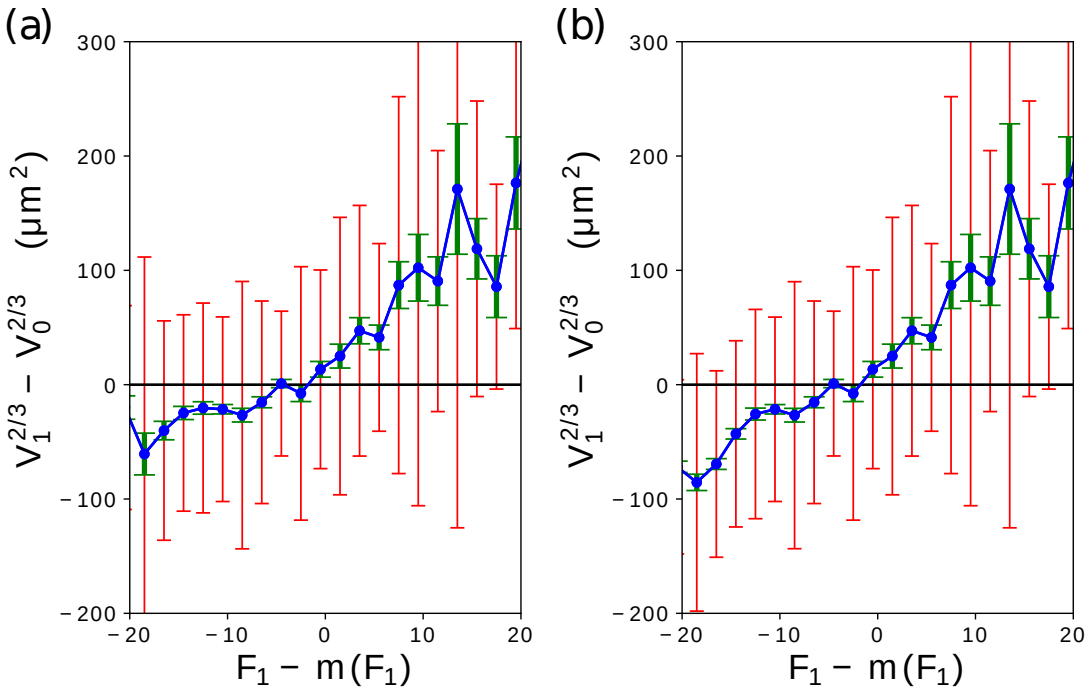

Figure 2.8. Test of the linear relation of equation (2.6). (a) shows matched grains only while (b) includes a statistically estimated correction, based on the size distribution of unmatched grains, for grains that were consumed during annealing; these grains were assigned $V_1 = 0$. The same as Fig. 2.5, blue points and red error bars are the means and standard deviations for each bin. Green error bars are the standard deviations of the estimated mean values.

do appear to roughly correlate with Equation (2.6). The mean values roughly follow a straight line which crosses zero volume change near $F_1 - m(F_1) = 0$. However, the region $F_1 - m(F_1) < 0$, where neighbors have more faces than the grain in question, appears to deviate from the linear trend. As discussed with respect to Fig. 2.5, this is likely due to neglect of disappearing grains. Performing the same correction as in that case yields Fig. 2.8(b) with an improved linear region around zero volume change. The large standard deviations are consistent with Fig. 2.7 and are seen to be comparable to the overall trend in the mean.

Again in this case, the variation in response within each category, indicated by the standard deviation bars, is large and crosses zero volume change in almost every class. The average behavior is again not a good predictor of a particular grain's response. We discuss this failure, which is consistent with prior work [22, 28] in Sec. 2.4; the

next section gives anecdotal examples of unexpected behaviors.

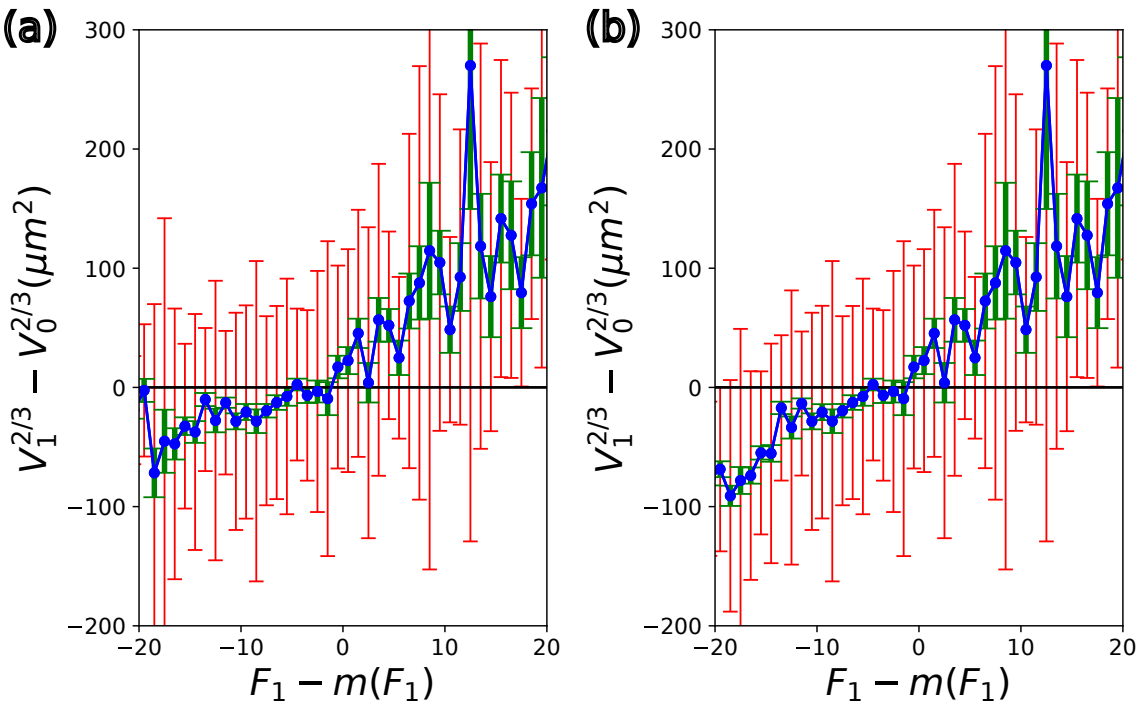

Figure 2.9. Test of the linear relation of equation (2.6) with a smaller binning size. (a) shows matched grains only while (b) includes a statistically estimated correction, based on the size distribution of unmatched grains, for grains that were consumed during annealing; these grains were assigned $V_1 = 0$. The same as Fig. 2.5, blue points and red error bars are the means and standard deviations for each bin. Green error bars are the standard deviations of the estimated mean values.

A similar plot with smaller binning size is shown in Fig. 2.9. It shows some fluctuations of the blue lines, which are the averaged values in the bins. Those fluctuations result from counting noisy, therefore measuring large number of grains (and tracking them) is essential to these and similar statistical analyses.

2.3.3 Other statistics

Statistical distributions Fig. 2.10 shows the distributions of disorientations at grain boundaries, weighted by boundary area (the boundary area is calculated without any smoothing, so this is larger than the real boundary area). Note that the distributions are similar to the Mackenzie distribution, but are slightly larger than random for low angle boundaries and there is a deficit near the peak at 45°. These features, as well as the peak at 60°, reflect the anisotropic grain boundary energies presented in Ref. [45]. As expected, the peak due to the low energy twin boundaries at 60° is weaker than that found in fcc nickel. [32]

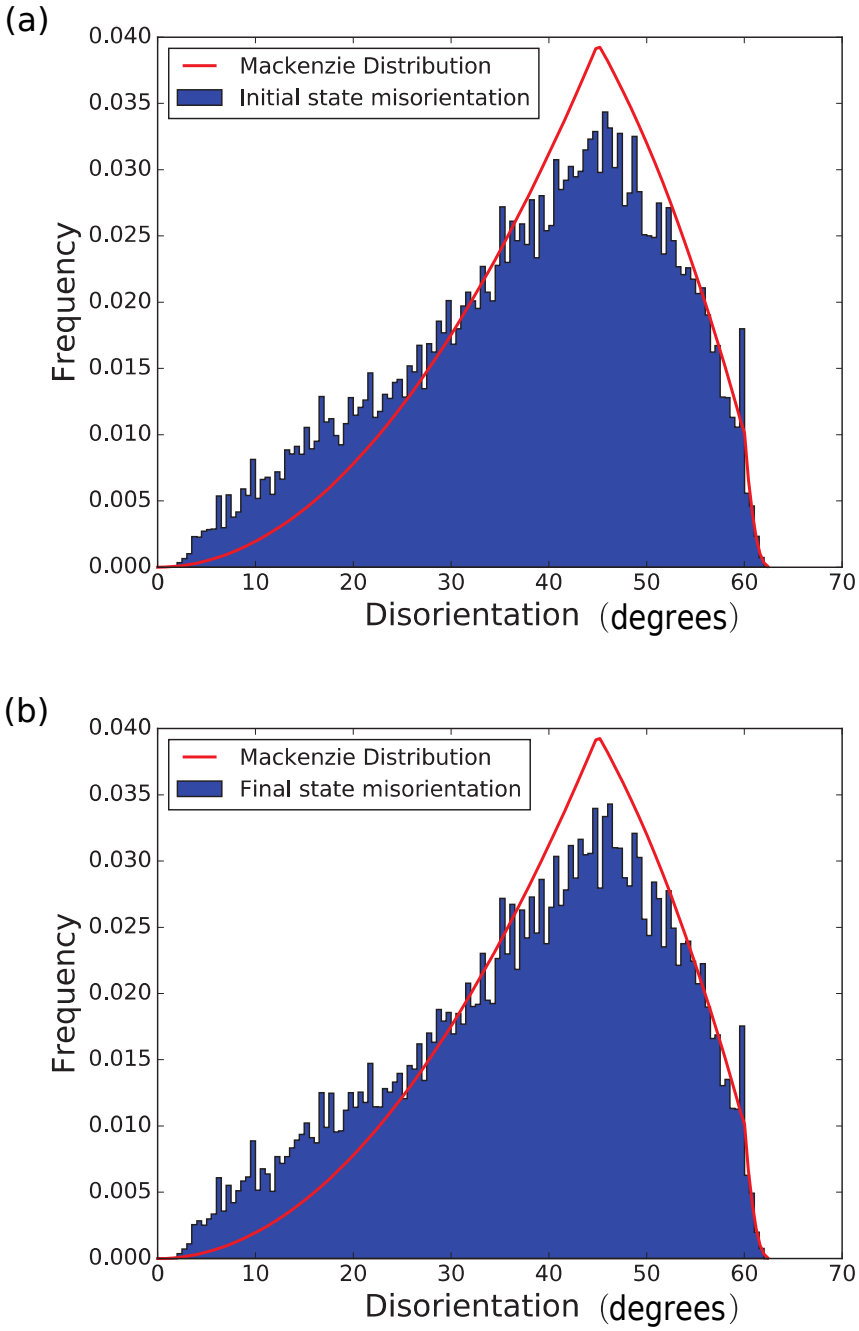

Figure 2.10. Disorientation distribution with bin size equal to 0.5°. The solid red line is the Mackenzie distribution [1] for randomly oriented cubes. The distribution is essentially unchanged during annealing.

Other important statistics are about grain faces. Fig. 2.11 confirms that on

average larger grains have more faces than small grains. The dispersion in the SED values here is smaller than the overall trend, in contrast to the growth characteristics discussed in the text.

Fig. 2.12, similar to Fig. 7 of [41], shows that grains with small face numbers, F, are likely to be surrounded by grains having more faces; grains with $F \approx 18$ have zero excess face number, which is consistent with Figs. 2.5 and 2.8. Fig. 2.8 shows that this value separates, on average, grains that grow from grains that shrink. However, this criterion is not predictive for individual grains.These plots are similar to, but with slightly different parameters from plots seen in, for example, Refs. [42, 41].

Matched grain pair characteristics The following figures show statistical analysis of the grain pairs found through the analysis described in Sec. 2.2.3. These figures validate the parameters used in the grain matching algorithm. Fig. 2.13a shows the size ratios of paired grains. Of the tracked grains, roughly as many decreased in size as increased. Of course, many grains disappeared or were consumed by others (and therefore were not matched); such events break the near-symmetry and result in increased average grain size.

Fig. 2.13b shows the ratio of center-of-mass displacements to the spherical equivalent diameter in the final state. Most displacements are less than one diameter but a few are substantially larger indicating asymmetric growth, which results primarily from some small grains.

The misorientation angles between tracked grains in the initial state and after annealing are shown in Fig. 2.13c to be generally less than 0.1° which is the nominal resolution of the measurement. A small number of pairs extend up to the maximum rotation allowed by the parameters used in the matching algorithm. The cut-off at $\approx 0.04^\circ$ probably indicates residual misalignment of the two sample states.

Figs. 2.13d - 2.13f show individual center-of-mass displacement components in the sample coordinate system. The mean values correspond to $\approx (-7, 10, 4)$ μm with x and y being in the plane of each layer measurement and z being perpendicular thereto. With average grain diameters of ≈ 30 μm, these displacements are consistent with data of Fig. 2.13b. The fact that these component displacements are not centered on zero may indicate a residual lack of alignment or simply the statistics of grains that were tracked. Note that the average z-displacement corresponds to roughly one layer spacing in the measurement; the in-plane voxel side lengths are 3 μm.

Next, we turn to the statistics associated with unmatched grains. Fig. 2.14a shows the size distribution of unmatched grains in each state. Most contain fewer than 100 voxels in the initial state and an even tighter distribution in the final state. Many of these grains may have been consumed during annealing and therefore are not present after annealing. However, those grains having spherical equivalent diameters < 5 μm, which is less than the offsets shown in Figs. 2.13d - 2.13f, also may have been rejected by the matching algorithm. In addition, smaller grains may tend to have larger volume change ratios, which is another reason that they could be wrongly rejected

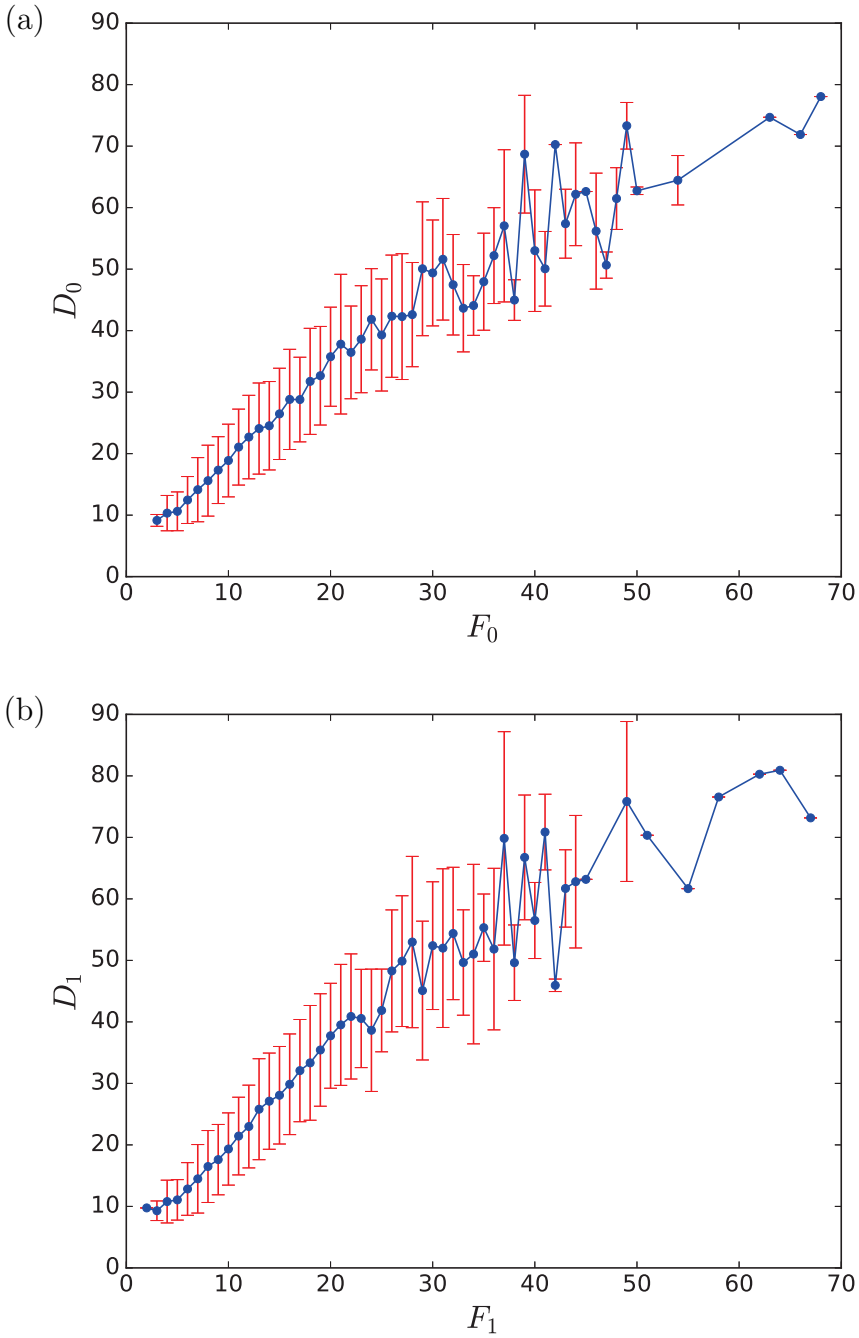

Figure 2.11. Relation between grain spherical equivalent diameter and the number of nearest neighbors, F. The grains with the same numbers of neighbors are grouped together and the mean (blue line) and standard deviation (red bar) are calculated for each group. (a) initial state, (b) final state.

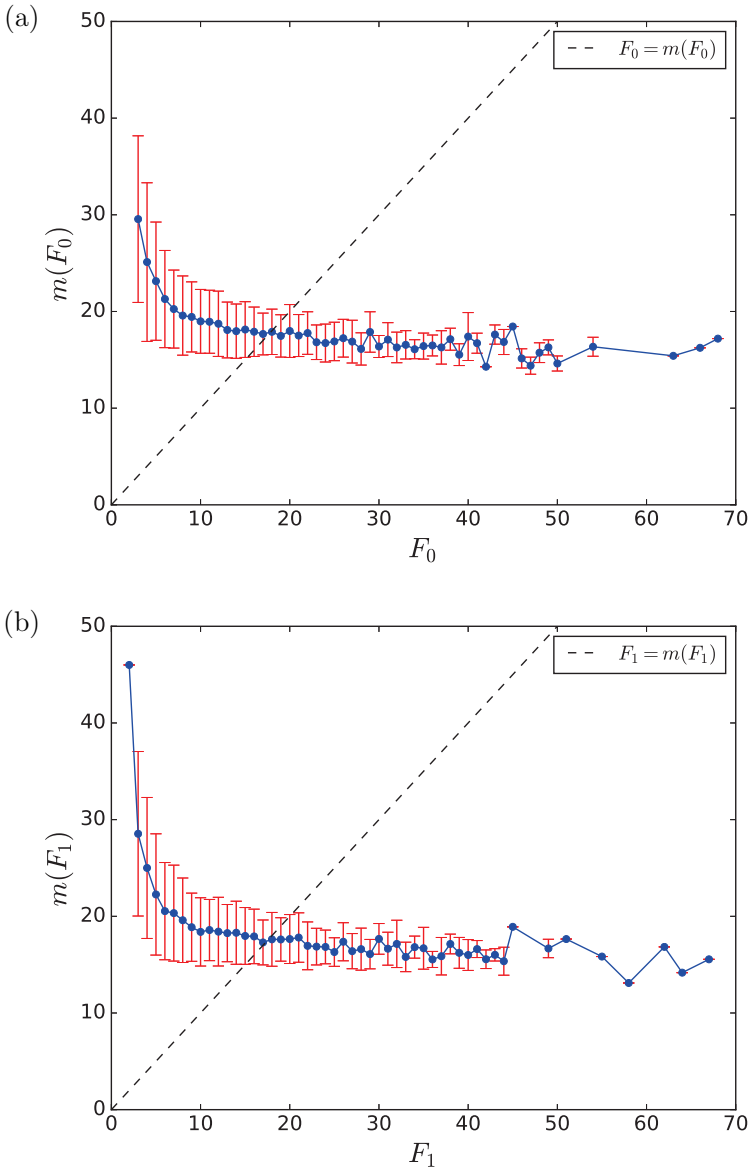

Figure 2.12. Aboav-Weaire plots [2, 3] giving the relation between the number of neighbors a grain has, F, and the average number of neighbors its neighbors have, $m(F)$. Subscripts on F indicate (a) initial and (b) final anneal states. Grains with each neighbor number F are grouped together and the mean (blue) and standard deviation (red) of $m(F)$ for those grains are plotted. The dashed line separates regions in which $m(F) > F$ (upper left) from the region with $m(F) < F$ (lower right).

by the matching algorithm. Fig. 2.14b shows the vertical position distribution of unmatched grains, which is roughly uniform as expected. There are slightly more unmatched grains at the bottom edge of the initial state and the top edge of final

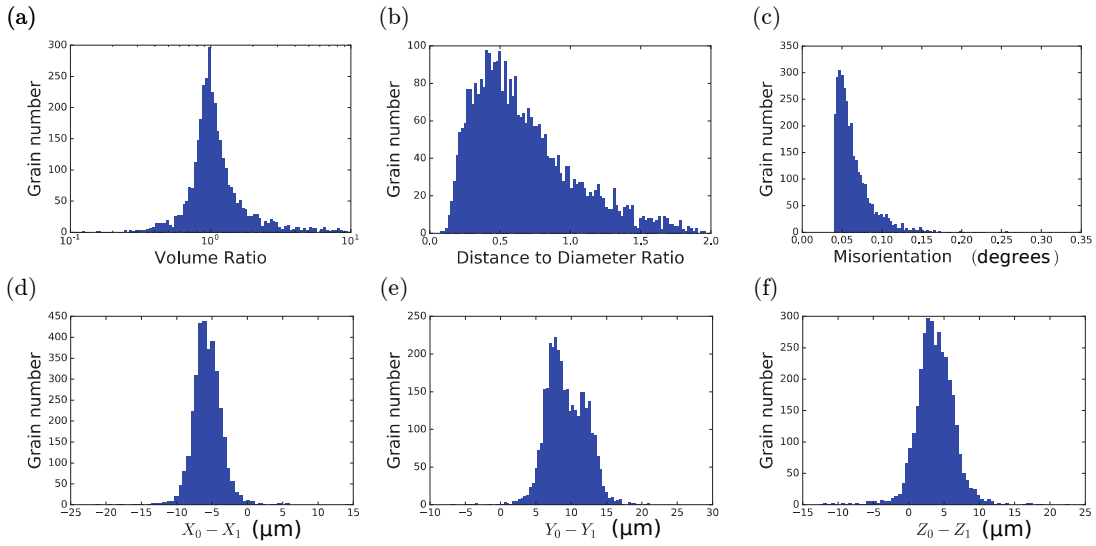

Figure 2.13. Distributions of matched grain properties. Horizontal axis units in (d) - (f) are microns. (a) shows the ratio of spherical equivalent diameters, D_1/D_0; (b) shows the distance between centers-of-mass in the two states divided by D_0; (c) demonstrates that the rotation angle required to bring matched grain orientations in the two states into coincidence is typically less than 0.1 degree; (d) through (f) show the center-of-mass displacements between states in Cartesian component form; the z direction is perpendicular to the line focused x-ray beam plane.

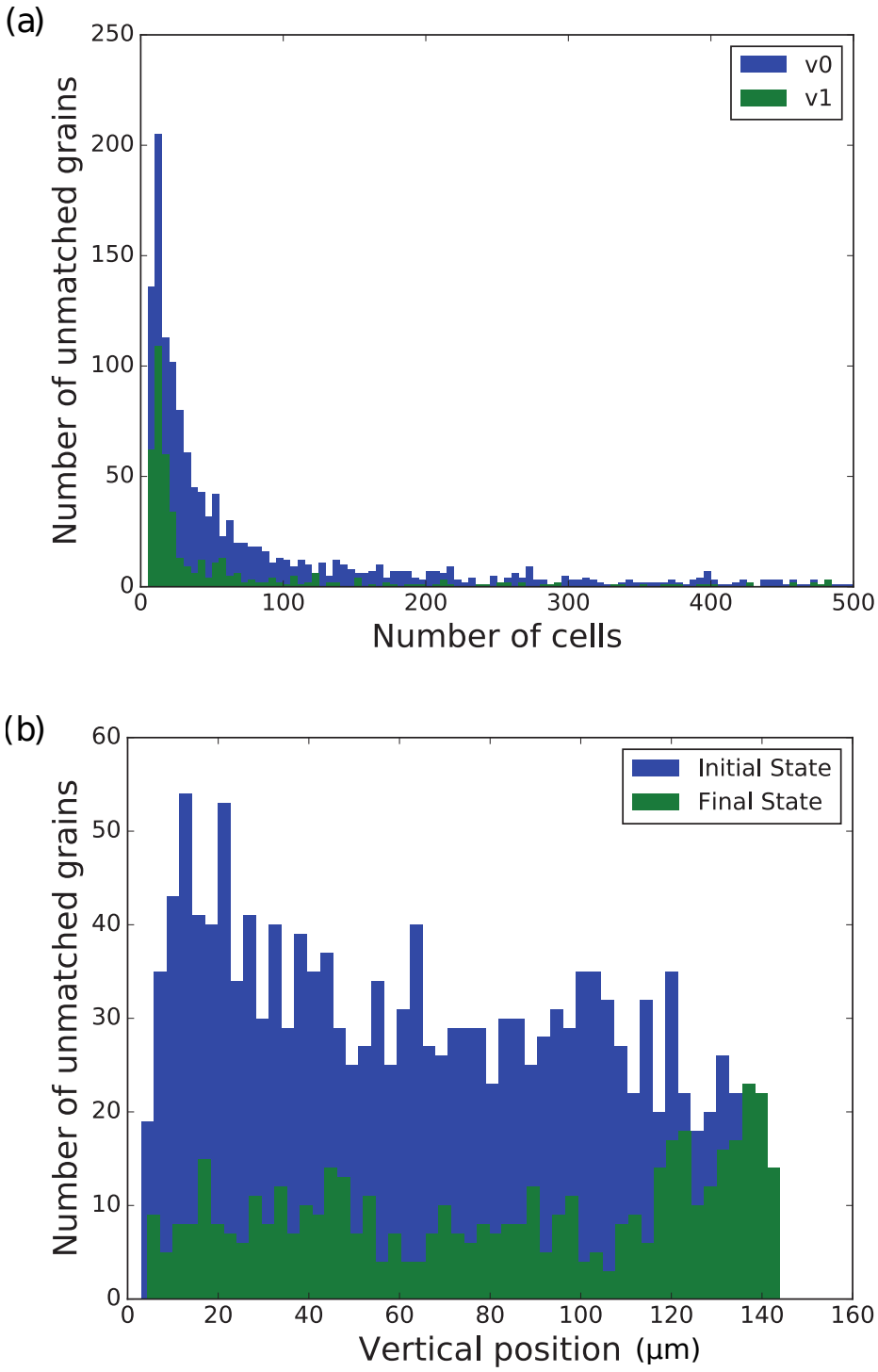

Figure 2.14. Statistics of unmatched grains. (a) Shows the size distributions in each state in terms of the number of $3 \times 3 \times 3$ μm^3 cells, each of which corresponds to about eight reconstructed voxels. A small number of larger unmatched grains are not shown. (b) Shows the locations in z coordinate in microns of unmatched grains.

state; this is consistent with Fig. 2.13f which shows a ~ 4 μm offset between the two volume measurements.

2.3.4 Examples of anomalous behavior

The large standard deviations discussed above imply that local fluctuations in behavior are important and that outlier behavior can be expected. While a comprehensive analysis of grain boundary movements correlated with grain boundary character is beyond the scope of this work, we show here examples of counter intuitive behavior. These examples illustrate both intrinsic effects and ambiguities that arise from the parameters associated with defining and matching grains.

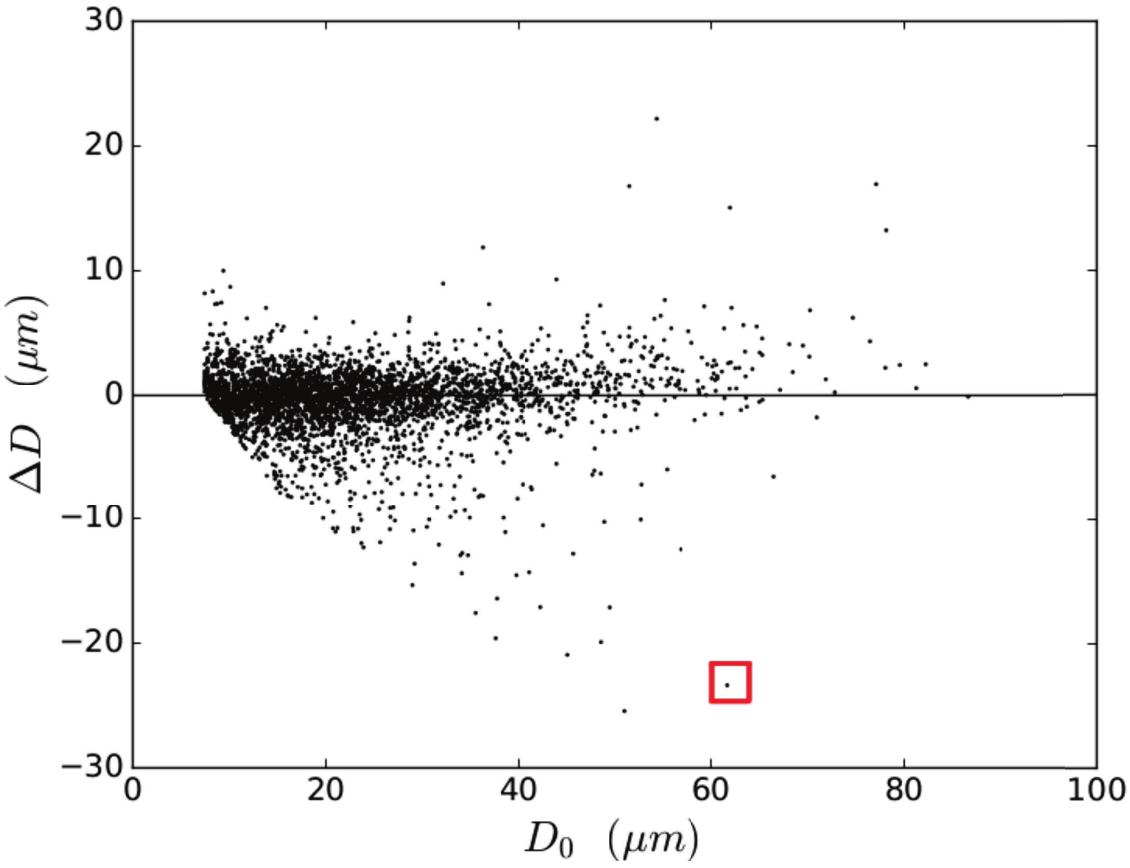

Figure 2.15. Changes in diameter for all 3299 matched grains as a function of initial size. Each point represents a single grain. A large grain, discussed in Sec. 2.3.4 that shrank during annealing is identified by red box.

Big vs. bigger In a large ensemble, it is not surprising to find two or more large grains that are nearest neighbors. Since "large" grains are expected to consume

"small" ones, this is one mechanism to explain the observation that some large grains shrink. Such behavior is entirely consistent with curvature driven growth laws, either with or without the isotropy assumption. With the statistical correlation between face number and grain size shown in Fig. 2.11, this effect can explain at least some of the dispersion seen in Figs. 2.5 and 2.8.

Fig. 2.15 shows the change in spherical equivalent diameter for grains with a wide range of initial diameters. There is only a weak average trend for larger grains to grow, as is implicit in Fig. 2.5. Again, dispersion is the dominant feature. The red box indicates an initially large grain (initial SED of 62 μm or volume $\sim 10^5$ μm^3) that shrinks substantially during annealing. Fig. 2.16 shows this grain in yellow and two of its neighbors (green and purple) that are even larger in the two states. The yellow grain appears to be convex over much of the visible boundary and it is consumed by the large and oddly shaped green grain beneath it as well as by the unseen grain in front.

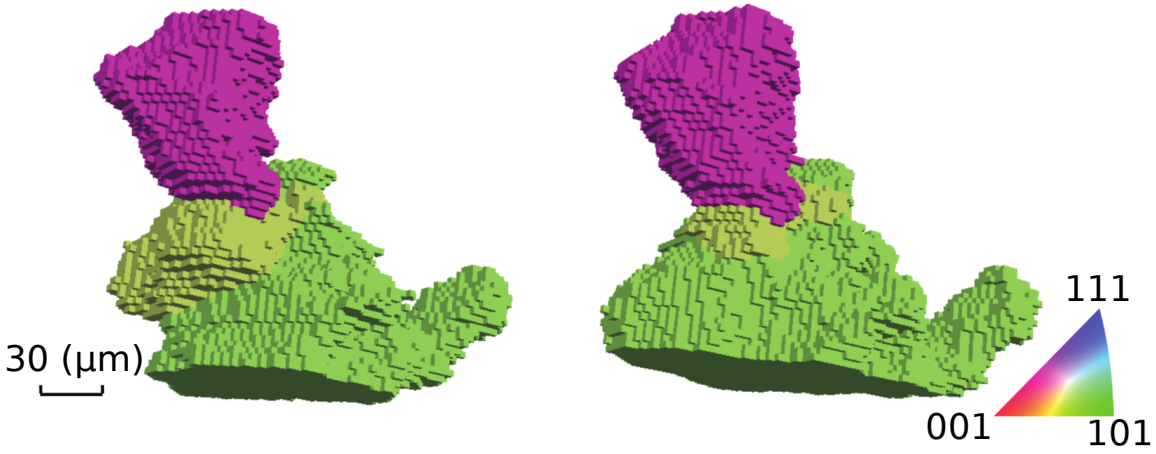

Figure 2.16. The yellow grain is large but is seen to shrink during annealing. The bottom of the green grain is cut off by the end of the measurement volume.

Anomalous grain division and matching Another interesting case is the grain boxed in red in Fig. 2.6: in the initial state, it has a substantial excess number of faces, $F_0 - m(F_0) \approx 35$. But the grain boundary topology changed dramatically during annealing so that $F_1 - m(F_1) \approx 0$ afterwards. After some investigation, it turns out that the relevant grain (light blue) was split in two by a growing small grain, as shown in Fig. 2.17. The grain matching algorithm, when run in the forward direction, matched the initial grain to one of the two split grains, resulting in the dramatic reduction in excess face number. In the reverse direction, both split grains are matched to the same initial whole grain. This anomalous behavior also caused the unexpected drop in Fig. 2.5 between $40 < F_0 < 50$. The mystery, of course, is why did the small yellow grain succeed in growing through its larger neighbor? An

alternate explanation would be some sort of unexpected reconstruction artifact in one or the other state.

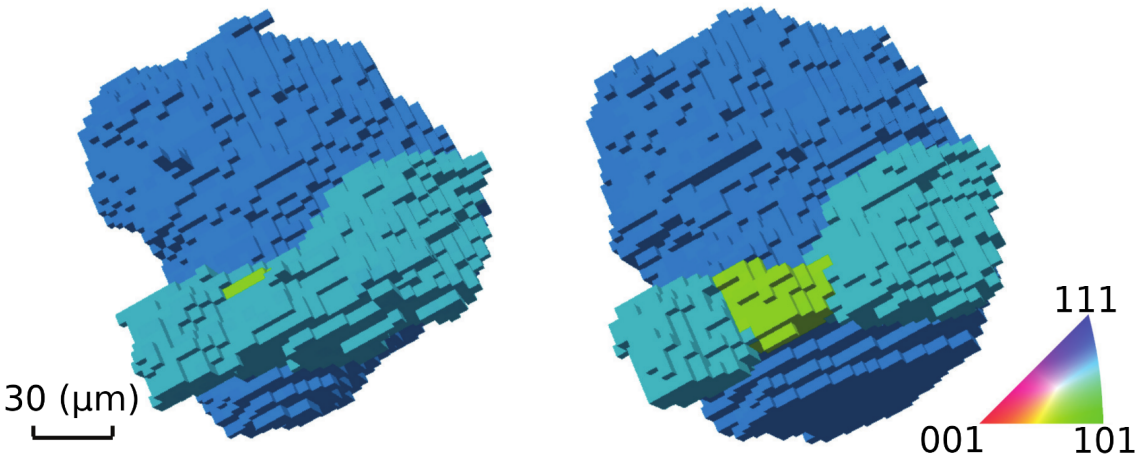

Figure 2.17. The light blue grain in the initial state (left) is split in two (right) by a growing small yellow grain. The flat bottom of the large dark blue grain in the annealed state indicates that it reached the edge of the measurement volume.

Apparent grain rotation For grains with diameters of several microns and larger, grain rotation is not expected during the coarsening process because the constituent crystallites are highly constrained by their neighbors. The distribution of disorientation angles between matched grain pairs are shown in Fig. 2.13c. Most have $\leq 0.1°$ disorientations which is the resolution of the measurement and is therefore consistent with zero. However, there are several cases (out of 3299 matched pairs) where the disorientations are $> 0.2°$. Fig. 2.18 explains one extreme case and shows that this case is an artifact of the arbitrary threshold used in segmenting grains. The two grains shown are separated by a low angle boundary, indicated by the black lines, of $\approx 1.8°$ disorientation. With the disorientation tolerance of 2° used in *DREAM.3D* for segmenting voxels into grains, these two grains were grouped together as one. The change of relative volumes caused by motion of the low angle boundary during annealing caused the grain average orientation to change while the orientations of each sub-grain did not change beyond the experimental resolution. Again, the grain matching algorithm in this work uses the disorientation angle as one of its criteria, so it may miss grain pairs whose average orientation rotated too much ($> 0.5°$) due to such low angle boundary motions.

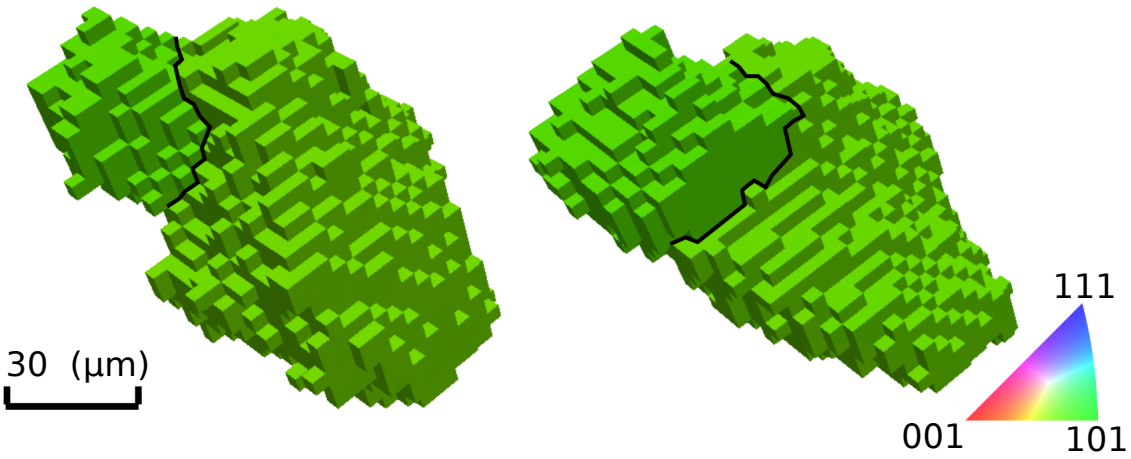

Figure 2.18. Two grains that have a low angle boundary of $\approx 1.8°$ disorientation, indicated by the black lines. With the disorientation tolerance ($= 2°$) used in *DREAM.3D*, they were considered together as one grain, so the change of relative volume ratio caused the change of the average grain orientation.

2.4 Discussion

Near-field high energy x-ray diffraction microscopy makes possible this statistical study of α phase iron grain coarsening. Over 10,000 grains are reconstructed with the forward modeling method [24, 4] in each of two sample states. The grain statistics and changes thereof presented here are not dependent on resolution of individual grain boundaries and therefore do not involve boundary smoothing and tracking. On the other hand, the estimation of the probability density for finding grains of volume V (Fig. 2.3) is affected by the finite measured volume and finite experimental resolution. We give an estimated correction for the finite volume effect and we use a conservative small size cut-off to avoid distortions due to reduced sensitivity in this limit. The most significant contribution to uncertainty in the grain evolution analysis is the lack of perfect matching of grains between the two states; this problem is most apparent for small grains as shown in Fig. 2.14a but also has a contribution due to initial grains that grow past the boundaries of the measured volume in the final state.

We assume that new grains do not nucleate in the fully recrystallized material with tens of micron grain dimensions. While rare exceptions have been observed in nickel [46] associated with very low energy annealing twin formation, corresponding low energy boundaries are not available in the α phase, bcc structure measured here. The lack of large twin populations simplifies analysis relative to current studies of nickel. [47]

In an averaged sense, the isotropic model for coarsening that assumes that all boundaries have the same energy and mobility compares very well with the observed grain evolution. This implies that the normalized mean curvature alone can be used to

describe average grain growth behavior. However, as shown in Figs. 2.5 and 2.8, individual grains within a topological class vary in their growth by as much as $\sim \pm 100\%$ of the observed range of average behaviors. This range of variation is consistent with prior observations of coarsening in two dimensional succinonitrile ($C_2H_4(CN)_2$) polycrystals [22], with recent observations of iron by Zhang et al., [28] and with our observations of nickel. [47] In the succinonitrile case, the authors observed that the growth rate of the average grain area, $\langle A \rangle$, within topological classes specified by the number of grain sides or neighbors, n, was consistent with the classic, isotropic $n-6$ dependence. [10, 11] But, similar to the recent observations, large variations from grain to grain were observed with variations in each class of order 100% of the observed range of averaged behaviors.

There are a number of possible origins of the observed large dispersion in growth characteristics within topological classes. i) The empirical relation between $F-m(F)$ and mean curvature, g, itself has substantial dispersion but less than the range of variation in g. [41] It is based on experimentally measured curvatures so a portion of observed dispersion may be due to measurement uncertainties. It appears that this contribution does not account for observed variations in Figs. 2.7 and 2.8. ii) During the annealing used here, the values of $F - m(F)$ are not constant as shown in Fig. 2.6. However, given the slope of the mean in Fig. 2.8, changes of ± 4 as consistent with Fig. 2.6 are not sufficient to generate the observed large distribution widths. iii) More interestingly, grain boundary energies and mobilities are, in fact, not uniform and the inclusion of many boundary types within topological classes can be expected to generate dispersion in the statistics presented here. Further, Zhang et al. [28] speculate that their observed reduction in growth rate may be associated with large variations in mobility. These observations strongly motivate ongoing work that will analyze motions of individual boundaries and that can extract, for example, boundary energy distributions. [48] Further experimental work is certainly warranted. Extending measured volumes while maintaining comparable grain sizes can increase the dynamic range of the measurements. Expanding the range of growth may elucidate how distributions evolve toward the steady state.

On a measurement technique note, the apparent near-field HEDM measurement sensitivity to almost four decades in grain volume while the detector sensitivity spans only about three decades can be understood from the fact that observed intensities on the near-field detector do not scale with grain volume as they do in a more traditional (or in a far-field HEDM [33]) measurement. In a sub-grain resolved diffraction measurement, detector pixel intensities are proportional to the sub-volume of the grain, $V_{(j,k)}^{grain}$, that projects intensity to the pixel rather than the entire grain volume. Here, (j,k) specifies a pixel coordinate. For a large grain, $V_{(j,k)}^{grain}$ is proportional to the pixel area (and the beam height and geometric factors specifying the scattering geometry for a given Bragg peak). Until the volume "seen" by the pixel starts to extend beyond the grain's boundaries (due to either small grain size or when scattering originates from near a boundary of a large grain) the intensity is independent of grain size.

Chapter 3

Determining Grain Boundary Energies From Triple Junction Geometries

3.1 Background

The property and performance of polycrystalline materials can be modified by engineering the grain boundary network [49]. For example, Kokawa shows a one-step thermomechanical process can suppress the weld-decay of an austenitic steel as the degree of sensitization drops 63% and the corrosion rate drops 44% [50]. It was shown that the steady state creep rate of Ni-16Cr-9Fe decreases 96% at 360°C in an argon atmosphere as the fraction of coincident site lattice boundaries increases from 16% to 43% [51]. Underlying such dramatic performance changes is the fact that grain boundary properties are anisotropic. Our work focuses on determining the relative grain boundary energies, which govern the evolution of the grain boundary network at high temperatures.

Decades of research have been devoted to finding a concise and descriptive function for the dependence of the grain boundary energy on the five crystallographic parameters. Several theoretical models [52, 53, 54, 55, 56] are inspired by experimental observations [57, 58, 59, 60]. However, though the existing models usually work well under their specific set of assumptions, most of them fail to capture the entire grain boundary energy landscape [61]. The greatest obstacles are the vast number of distinct grain boundary types and limited experimental data. Recently, Bulatov proposed an interpolation function which appears to successfully capture variations of grain boundary energy in face-centered cubic materials for the first time [61]. Nevertheless, Bulatov's function was entirely based on the Read-Shockley-Wolf function [62] and 388 grain boundary energies calculated by molecular dynamics simulations [63]. It is likely that if more accurate and abundant experimental data becomes available, it will be possible to create a similar, or more general, experiment-based grain

boundary energy function.

A method to extract relative grain boundary energies from experimental data was described by Morawiec in 2000 [64]. The experimental data used as input for the method consists of the geometries of many triple lines; for each triple line, the three grain orientations, the triple line direction, and the orientations of the three grain boundary planes are specified. The method has been used to reconstruct the grain boundary energy distributions of MgO, Ni, Y_2O_3, austenite, and ferrite [65, 66, 67, 68, 69].

3.1.1 Preliminaries

Grain boundaries can be characterized by five macroscopic parameters. Typically, three parameters are used for the lattice misorientation across the boundary and the other two for the boundary plane orientation [12]. Experimental systems provide voxel-wise orientations in a 3D volume, which can be used to determine grain orientations and boundary plane inclinations. Using the same notation as in [64], the orientations of the two neighboring grains are represented by two special orthogonal matrices $\bar{\mathbf{o}}_\mathbf{1}$ and $\bar{\mathbf{o}}_\mathbf{2}$ (the over-line means that the variable is in the sample frame, otherwise the variable is in the crystal frame). So the misorientation is $\mathbf{m} = \bar{\mathbf{o}}_\mathbf{1}\bar{\mathbf{o}}_\mathbf{2}^T$, and the normal direction of the boundary directed from the first grain to the second grain is represented by a unit vector $\mathbf{n}$. The macro-parameters $\mathbf{m}$ and $\mathbf{n}$ together will determine the grain boundary energy γ. For convenience, we can use a 4×4 matrix $\mathbf{b}$ to represent all five parameters:

$$\mathbf{b}(\mathbf{m}, \mathbf{n}) = \begin{bmatrix} \mathbf{m} & \mathbf{n} \\ -\mathbf{n^T m} & 0 \end{bmatrix}.$$

As a result of crystal symmetry, there are many distinct sets of parameters corresponding to physically indistinguishable grain boundaries. A 4×4 matrix

$$\mathbf{C_i} = \begin{bmatrix} \mathbf{c_i} & 0 \\ 0 & 1 \end{bmatrix},$$

where $\mathbf{c_i}$ is a 3×3 matrix used to represent one of the symmetry operations of the crystal point group (without improper rotations). Then, the set of physically identical grain boundaries of $\mathbf{b}$ consists of $\mathbf{C_i b C_j}$, $\mathbf{C_i b^T C_j}$, $\mathbf{C_i b^- C_j}$, $\mathbf{C_i (b^-)^T C_j}$, where $\mathbf{b}^- = \mathbf{b}(\mathbf{m}, -\mathbf{n})$. We use $S_q(\mathbf{b})$ as the qth element in this set. Obviously, all elements in this set have the same energy because they are physically identical.

It is convenient to define the "distance" between boundaries i and j as $\chi^2 = \chi_{ij}^2 = \min_q \|S_q(\mathbf{b_i}) - \mathbf{b_j}\|^2/2$, where the norm $\|\cdot\|$ of a matrix $\mathbf{M}$ is given by $\|\mathbf{M}\| = tr(\mathbf{M^T M})^{1/2}$. The exceptional case is the distance from the "no misorientation boundary" $\mathbf{b}(\mathbf{I_3}, \mathbf{n})$, where $\mathbf{I_3}$ is the identity matrix. Since the normal direction is irrelevant when there is no misorientation between grains, in this case we define $\chi^2 = \min_q \|S_q(\mathbf{m}) - \mathbf{I_3}\|^2/2$, where $\mathbf{m}$ is the 3×3 misorientation for boundary

$\mathbf{b}(\mathbf{m},\mathbf{n})$ and $S_q(\mathbf{m})$ are the misorientations symmetrically equivalent to $\mathbf{m}$, i.e., $\mathbf{c_i m c_j}$ and $\mathbf{c_i m^T c_j}$ for all $\mathbf{c_i}, \mathbf{c_j}$.

The grain boundary energy $\gamma(\mathbf{b}) = \gamma(S_q(\mathbf{b}))$ is what we want to infer from experimental data. Based on the assumption of local equilibrium, we can recover relative grain boundary energies from the triple junction geometries.

For the triple junction that consists of grain boundaries i, j, k, the equilibrium equation is

$$(\bar{\xi}_\mathbf{i} + \bar{\xi}_\mathbf{j} + \bar{\xi}_\mathbf{k}) \times \bar{\mathbf{t}} = \mathbf{0}, \tag{3.1}$$

where $\bar{\mathbf{t}}$ is tangent to the junction and $\bar{\xi}_\mathbf{i}$ is the capillarity vector of the ith boundary. The capillarity vector is defined as

$$\xi = \gamma \mathbf{n} + \frac{\partial \gamma}{\partial \mathbf{n}}.$$

For more details on the capillarity vector, readers are refered to the original papers [70, 71, 72].

3.1.2 Conventional method

We refer to Morawiec's method [64] as the conventional method in this chapter. In the conventional method, the five-parameter space is divided into discrete bins and each bin is associated with one unknown capillarity vector ξ_α (we use Greek letters as the indices of the bins). For every grain boundary in the experimental dataset, its capillarity vector $\bar{\xi}_\mathbf{i}$ is calculated by averaging all the capillarity vectors ξ_α of the bins that contain $\mathbf{b_i}$'s equivalences. Substituting the $\bar{\xi}_\mathbf{i}$'s in Eq. 3.1 with linear combinations of ξ_α's for all triple junctions yields a set of linear equations for ξ_α's

$$\mathbf{A} \cdot \mathbf{X} = \mathbf{0} \ , \tag{3.2}$$

where $\mathbf{X} = [\xi_1^x \ \xi_1^y \ \xi_1^z \ \ldots \ \xi_\alpha^x \ \xi_\alpha^y \ \xi_\alpha^z \ \ldots \ \xi_M^x \ \xi_M^y \ \xi_M^z]^T$, M is the total number of bins, $\xi_\alpha^x, \xi_\alpha^y, \xi_\alpha^z$ are the x, y, z components of ξ_α, and matrix $\mathbf{A}$ is derived from the equilibrium equations and the symmetry operations. See [64] for the detailed expression of matrix $\mathbf{A}$. Finally, we solve for the ξ_αs from this linear equation set by minimizing the sum of squared residuals while keeping the norm of the vector of unknowns. The solution is the eigenvector corresponding to the smallest eigenvalue of $\mathbf{A^T A}$. It can be solved by gradient-based iterative methods.

So, mathematically, this method uses a set of basis functions (having value 1 in one bin and value 0 in other bins) for the capillarity vector function $\xi(\mathbf{b})$, and all the capillarity vectors, ξ_α, defined on the bins are the coefficients. The reconstruction process is to find the best set of coefficients to approximate a $\xi(\mathbf{b})$ that satisfies all the equilibrium equations. When the grain boundary parameters are discretized, the three Eulerian angles giving the disorientation are considered within the domain of 0 to 90°. For the spherical angles defining the boundary inclination, the polar angle is

also considered within the domain of 0 to 90° and the azimuthal angle is considered within the domain of 0 to 360°. Using a typical discretization with 10° bins, there are $M = 9^4 \times 36$ bins and $3M = 708588$ coefficients to be fit [73, 74].

Currently, a typical 3D microstructure dataset measured by electron backscatter diffraction (EBSD) [75] or high energy X-ray diffraction microscopy (HEDM) [24] contains $10^4 \sim 10^5$ triple junctions [68, 69], and each triple junction gives one equilibrium equation (Equation 3.1), which corresponds to two independent scalar equations. So the reconstruction problem is an under-determined inverse problem, which has more unknowns (708588) than equations, i.e. $\mathbf{A}$ in equation 3.2 has more columns than rows, so $\mathbf{A^T A}$ has multiple eigenvectors corresponding to the smallest eigenvalue 0. In the original paper [64], the author addressed this issue by setting the starting point to be the boundary normal unit vector (i.e. $\xi_{\alpha \mathbf{0}} = \mathbf{n}_\alpha$) and using the gradient descent algorithm to find the minimum, which is an implicit regularization. Empirically this works very well for most cases, and the reconstructed grain boundary functions are consistent with theoretical expectations [65, 66, 67, 68, 69].

3.1.3 Motivation

While the conventional approach has been useful, it also has a number of limitations:

- It can not take advantage of increasing dataset size. If the dataset is too large, the discretization of five-parameter space can lead to some unexpected artifacts. See Section 3.4.3 for details.

- In many samples, grain boundaries are not distributed uniformly in the five-parameter space and in some cases, they are concentrated in a small region of five-parameter space and we only want to get the grain boundary energy function in that region. The conventional method cannot determine grain boundary energies from this kind of dataset easily. See Section 3.4.2 for details.

We propose a new framework for determining grain boundary energies from triple junction geometry. Instead of discretizing the five-parameter space and fitting the coefficients, this approach directly fits the capillarity vector $\xi_{\mathbf{i}}$ of each grain boundary in the dataset. Because the proposed approach does not use any parametric model for the grain boundary energy function, we refer to it as the non-parametric reconstruction method. The reconstruction method is described in detail in Section 3.2, and some results reconstructed from simulated triple junction geometries are presented in Section 3.4.

3.2 Non-parametric reconstruction framework

3.2.1 Overview

The goal of our new approach is to reconstruct the capillarity vector $\xi_\mathbf{i}$ of each grain boundary in the dataset without discretizing the five-parameter space. The unknowns can be written as a vector

$$\mathbf{X} = [\xi_1^x \ \xi_1^y \ \xi_1^z \ \cdots \ \xi_i^x \ \xi_i^y \ \xi_i^z \ \cdots \ \xi_{3W}^x \ \xi_{3W}^y \ \xi_{3W}^z]^T,$$

where W is the total number of triple junctions and the number of unknowns is $9W$ (three capillarity vectors for each triple junction, and three components for each vector).

We define $S(J)$ as the set of grain boundary IDs that consist in triple junction J, whose equilibrium equation (Eq. 3.1) can be written as

$$0 = \sum_{i \in S(J)} \sum_{l} B_{J,a}^{i,l} \xi_i^l,$$

where $B_{J,a}^{i,l} \equiv \sum_{b,c} \epsilon_{abc} \bar{t}^c \bar{o}_i{}^{lb}$ and ϵ_{abc} is the permutation symbol. See 3.2.2 for details.

Using the subscript (J, a) as the row index, and the superscript (i, l) as the column index of matrix $\mathbf{B}$, we have a matrix equation $\mathbf{B} \cdot \mathbf{X} = \mathbf{0}$ to represent the equilibrium equations of all the triple junctions. There are $3W$ equations, and only $2W$ of them are independent, so this reconstruction problem is also an under-determined inverse problem. Because of this, some regularization techniques are needed. Mathematically, we can write it as a constrained minimization problem:

$$\begin{aligned} &\min_{\mathbf{X}} \ \ R(\mathbf{X}) \\ &s.t. \ \ \|\mathbf{X}\|^2 = 1, \ \ \mathbf{B} \cdot \mathbf{X} = \mathbf{0}. \end{aligned} \tag{3.3}$$

There are many choices for the regularization term $R(\mathbf{X})$. A common choice is based on the assumption that grain boundary energy functions are smooth, which means that if two grain boundaries i and j have similar physical characteristics (i.e., χ_{ij} is small), then their capillarity vectors should be similar, i.e.,

$$R(\mathbf{X}) = \sum_{(i,j) \in E} w_{ij} \|\xi_\mathbf{i} - \mathbf{T_{ij}} \cdot \xi_\mathbf{j}\|^2, \tag{3.4}$$

where $E = \{(i, j) |$ boundary i and j are similar$\}$, w_{ij} is the weight that is proportional to the similarity of boundaries i and j, and $\mathbf{T_{ij}}$ is the operator that makes boundaries i and j have similar plane normal directions, i.e., $\mathbf{T_{ij}n_j} \approx \mathbf{n_i}$. 3.2.2 shows how to calculate $\mathbf{T_{ij}}$ from the symmetry operator and the misorientation. This regularization term penalizes the difference between capillarity vectors of physically similar grain boundaries. The form of the weight w_{ij} and the criterion for including

a pair of boundaries in the set E are essential in this non-parametric framework. In our work, the set E contains the boundary pairs whose distances are smaller than a threshold, and we use the inverse of distance as the weight $w_{ij} = 1/\chi_{ij}$. See 3.2.2 for more details.

Other regularization terms are also possible in this framework, for example using "similar energy" instead of "similar capillarity vector". Different choices correspond to different prior knowledge of the grain boundary energy distribution (GBED) and they will influence the results, robustness, and efficiency of the reconstruction. One thing we need to emphasize is that, no matter which regularization term we chose, the reconstruction result always satisfies all the equilibrium equations. The comparison of different regularization terms is beyond the scope of this work; in the following sections, we will use Eq. 3.4 as the regularization term.

Once the capillarity vectors are reconstructed, the grain boundary energy is $\gamma_i = \xi_{\mathbf{i}} \cdot \mathbf{n_i}$. Based on the values γ_i, the landscape of grain boundary energy function can be constructed by any interpolation method.

3.2.2 Numerical Details

Rewriting the equilibrium equation

We define $S(J)$ as the set of grain boundary IDs that consist in triple junction J. Vectors and tensors in sample frame are over-lined, otherwise they are in crystal frame. Writing all vectors and tensors in component form, the equilibrium equation becomes:

$$\begin{aligned} 0 &= \sum_{b,c} \epsilon_{abc} \sum_{i \in S(J)} \bar{\xi}_i^b \bar{t}^c \\ &= \sum_{b,c} \epsilon_{abc} \bar{t}^c \sum_{i \in S(J)} (\bar{\mathbf{o}}_{\mathbf{i}}^{\mathbf{T}} \xi_{\mathbf{i}})^b \\ &= \sum_{b,c} \epsilon_{abc} \bar{t}^c \sum_{i \in S(J)} \sum_{l} \bar{o}_i^{lb} \xi_i^l \\ \Longrightarrow 0 &= \sum_{i \in S(J)} \sum_{l} B_{J,a}^{i,l} \xi_i^l, \end{aligned}$$

where $B_{J,a}^{i,l} \equiv \sum_{b,c} \epsilon_{abc} \bar{t}^c \bar{o}_i^{lb}$.

The regularization term

Most of the computation time of the non-parametric approach is spent on constructing the regularization term. Because we need to find "neighbors" for each grain boundary, a naive algorithm has $O(n^2)$ time complexity, where n is the total number of grain boundaries in the dataset.

For every grain boundary $\mathbf{b}$ there are a set of physically identical boundaries $S_q(\mathbf{b})$, and they are all related by linear symmetry operators. To compare the capillarity vectors of boundaries i and j, we need the operator $\mathbf{T_{ij}}$ that makes boundaries i and j have similar plane normal directions, i.e., $\mathbf{T_{ij}n_j} \approx \mathbf{n_i}$, which can be calculated as follows:

$$\mathbf{T_{ij}} = \begin{cases} \mathbf{c_1} & \text{if} \quad S_{q^*}(\mathbf{b_j}) = \mathbf{C_1 b_j C_2} \\ -\mathbf{c_1 m_j^T} & \text{if} \quad S_{q^*}(\mathbf{b_j}) = \mathbf{C_1 b_j^T C_2} \\ -\mathbf{c_1} & \text{if} \quad S_{q^*}(\mathbf{b_j}) = \mathbf{C_1 b_j^- C_2} \\ \mathbf{c_1 m_j^T} & \text{if} \quad S_{q^*}(\mathbf{b_j}) = \mathbf{C_1 (b_j^-)^T C_2} \end{cases},$$

where $q^* = \arg\min_q \|\mathbf{b_i} - S_q(\mathbf{b_j})\|^2$.

After we find all the elements in the set $E = \{\text{Similar boundaries } (i,j)\}$, we can construct the regularization term:

$$R(\mathbf{X}) = \sum_{(i,j)\in E} \frac{1}{\chi_{ij}} \|\xi_\mathbf{i} - \mathbf{T_{ij}} \cdot \xi_\mathbf{j}\|^2,$$

where χ_{ij} is the "distance" between boundaries i and j defined in Section 3.1.1. The unknowns are represented by $\mathbf{X} = [\xi_1^x \ \xi_1^y \ \xi_1^z \ \ldots \ \xi_i^x \ \xi_i^y \ \xi_i^z \ \ldots \ \xi_{3W}^x \ \xi_{3W}^y \ \xi_{3W}^z]^T$. In this paper, we use $E = \{(i,j) \mid \chi_{ij} < 0.03\}$ for **DA06** and $E = \{(i,j) \mid \chi_{ij} < 0.015\}$ for **DB**, so that most boundaries have approximately 30 "neighbors".

Solving the minimization problem

If we use the equilibrium equations and normalization condition as the constraints, and try to minimize the regularization term, we get the following constrained optimization problem:

$$\begin{aligned} &\min_\mathbf{X} \quad \sum_{(i,j)\in E} \frac{1}{\chi_{ij}} \|\xi_\mathbf{i} - \mathbf{T_{ij}} \cdot \xi_\mathbf{j}\|^2 \equiv \min_\mathbf{X} \quad \|\mathbf{C} \cdot \mathbf{X}\|^2 \\ &s.t. \quad \|\mathbf{X}\|^2 = 1, \quad \mathbf{B} \cdot \mathbf{X} = 0, \end{aligned}$$

where $\mathbf{C}$ is defined by this regularization term.

One way to solve it is to choose a large enough number λ and the optimization problem approximately becomes:

$$\begin{aligned} &\min_\mathbf{X}(\|\mathbf{C} \cdot \mathbf{X}\|^2 + \lambda^2 \|\mathbf{B} \cdot \mathbf{X}\|^2) = \min_\mathbf{X} \mathbf{X^T}(\mathbf{C^T C} + \lambda^2 \mathbf{B^T B})\mathbf{X} \\ &s.t. \quad \|\mathbf{X}\|^2 = 1. \end{aligned}$$

This is an eigenvalue problem for finding the eigenvector corresponding to the smallest eigenvalue of $(\mathbf{C^T C} + \lambda^2 \mathbf{B^T B})$.

Another advantage of introducing λ is that, if the dataset is noisy we may want to relax the equilibrium equation constraints, we can then use smaller λ and have a trade-off between smoothness $\|\mathbf{C} \cdot \mathbf{X}\|^2$ and the noisy measurements $\|\mathbf{B} \cdot \mathbf{X}\|^2$.

Minimization algorithms

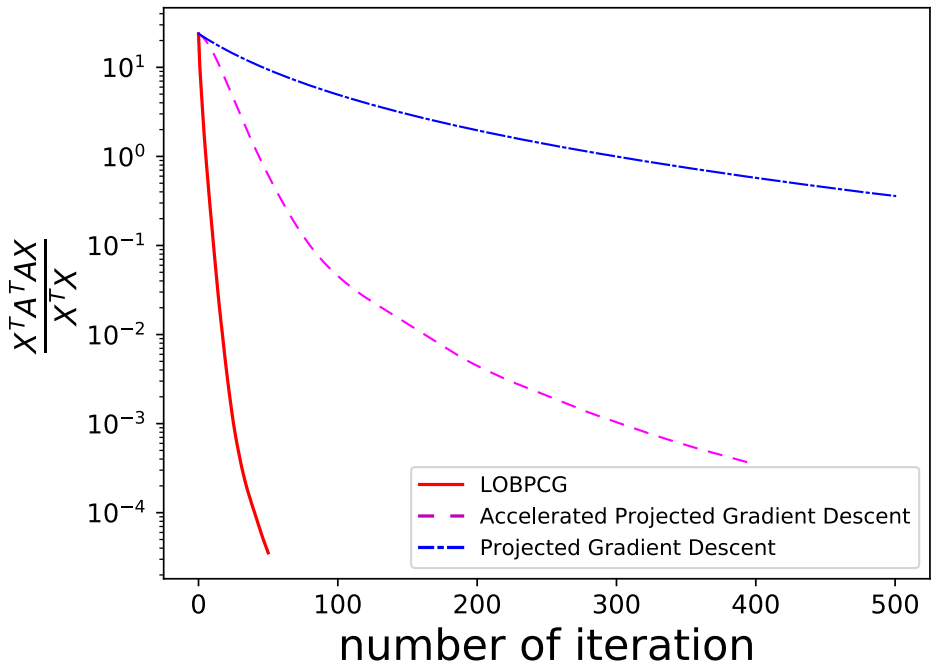

Figure 3.1: Comparison of convergence rate of different optimization methods. Projected Gradient Descent, Accelerated Projected Gradient Descent, and LOBPCG were used for the same problem. LOBPCG outperforms the other two methods.

Both the conventional method and the non-parametric approach make it necessary to solve a minimization problem. The projected gradient descent method was used in the prior work [64]. In our work, we rephrased the minimization problems as eigenvalue problems, which can be solved efficiently by the Locally Optimal Block Preconditioned Conjugate Gradient (LOBPCG) method [76]. It is also an iterative method but uses more information besides the gradient. A comparison between several different optimization methods was made. In Figure 3.1, the LOBPCG method converges much faster than other two methods. Faster optimization methods not only make it possible to reconstruct larger datasets, they also allow for more extensive investigation of the performance of the reconstruction under varying conditions.

3.3 Simulated datasets

We tested the non-parametric method and conventional method on several simulated datasets, which are only collections of triple junction geometries instead of the whole 3D microstructures. Based on any user-defined grain boundary energy functions, the simulation code can calculate the capillarity vector for any grain boundary pa-

Model	Σ	misorientation		boundary
		angle (°)	axis	plane
A	1	0.00	N/A	N/A
	3	60.00	[1 1 1]	(1 1 1)
	5	36.87	[1 0 0]	(0 2 1)
	7	38.21	[1 1 1]	(1 2 $\overline{3}$)
	9	38.94	[1 1 0]	(1 $\overline{1}$ 2)
	11	50.48	[1 1 0]	(2 $\overline{2}$ 3)
	13	22.62	[1 0 0]	(0 3 2)
	13	27.80	[1 1 1]	(1 3 $\overline{4}$)
B	1	0.00	N/A	N/A
	2	20.00	[0 0 1]	(1 1 0)

Table 3.1: Cusps in our grain boundary energy function models. We used $1/\sqrt{\Sigma}$ as the depth of the cusp and $\pi/(12\sqrt{\Sigma})$ as the width of cusp.

rameters, and it randomly generates the triple junction geometries that satisfy the equilibrium equations. The details of the simulation are in the Appendix of [64].

3.3.1 Model grain boundary energy function

In our work, the grain boundary energy functions that were used to create simulated triple junction geometries are based on a uniform energy distribution with superimposed cusps. The cusps are shaped in analogy to the Read-Shockley model [52]:

$$f(x,a) = ax(1-\ln x) + (1-a) \text{ for } 0 < x \leq 1$$
$$f(0,a) = 1-a \text{ and } f(x,a) = 1 \text{ otherwise,}$$

where a determines the "depth" of the cusp and x is the "relative distance" from the cusp center.

For the model that has cups at $\mathbf{b_k}$ ($k = 1, 2, 3...$), the grain boundary energy is $\gamma(\mathbf{b}) = \Pi_k f(\chi(\mathbf{b}, \mathbf{b_k})/w_k, a_k)$ where w_k, a_k are the width and depth of cusp k. The distance χ is defined in Section 3.1.1. So, the grain boundary energy is unity everywhere outside the cusps, and the cusps have the shape of the Read-Shockley expression.

3.3.2 Datasets

We used two hypothetical grain boundary energy functions, whose cusps are listed in Table 3.1. The depth of each cusp is $1/\sqrt{\Sigma}$ and the width is $\pi/(12\sqrt{\Sigma})$.

Model A has eight cusps and their Σs are the unit cell volume of the coincidence site lattice (CSL) in units of the elementary unit cell volume. Based on model A,

we generated a dataset containing 260000 random triple junctions, which we refer to as **DA26**. The grain boundaries in **DA26** are nearly uniformly distributed in the five-parameter space. We refer to the first 60000 triple junctions in **DA26** as **DA06**, which is close to the size of a real experimental dataset.

Model B mimics a sample with ideal axial texture and a columnar microstructure. It has 2 cusps, one is zero misorientation ($\Sigma = 1$), and the other one is manually picked whose Σ is just used in the simulation code for calculating the depth and width but is not related to the inverse coincidence. Using model B, we generated a dataset containing 1538 triple junctions, which we refer to as **DB**. The grain boundaries in **DB** are constrained in a 2D subspace of the five-parameter space: all misorientation axes are [0 0 1] and all boundary normals are perpendicular to [0 0 1]. In other words, in this dataset, all grains' [0 0 1] directions are parallel to a same direction, and that direction is also parallel to all junctions. Model B's cusps were chosen in this 2D subspace deliberately.

3.4 Results

Because the Eq. 3.1 is homogeneous, all grain boundary energies can only be determined up to a constant factor. To compare with the ground truth, we normalize the reconstructed grain boundary energies so that the average energy is the same as the average energy of the ground truth distribution; we refer to these as "normalized energies", γ_{rec}. Then γ_{rec} has whatever units are used to define the ground truth dataset.

3.4.1 Results on a normal size dataset

The performance of the reconstruction on **DA06** is representative of real datasets. Figure 3.2 shows the GBED for the $\Sigma 7$ misorientation of **DA06**, the stereographic projections are generated by a method based on boundary-space metrics [74]. Figure 3.3 demonstrates the energies of grain boundaries that are inside of $\Sigma 1$ cusp. Both the conventional method and the non-parametric method reconstructed the grain boundary energies well.

Figure 3.4 shows the reconstruction error in more detail. For every grain boundary (GB), we calculate the difference between normalized reconstructed energy and the ground truth $\gamma_{rec} - \gamma_{true}$, which have zero mean over the whole dataset by the definition of γ_{rec}. However, after we bin the grain boundaries by their true energy γ_{true}, the averaged $\gamma_{rec} - \gamma_{true}$ for each bin is no longer zero. As shown in Figure 3.4(a), grain boundaries with smaller γ_{true} tend to have larger $\gamma_{rec} - \gamma_{true}$, which means the cusps in the grain boundary energy function are smoothed by the reconstruction. Figure 3.4(b) and Figure 3.4(c) are the detailed $\gamma_{rec} - \gamma_{true}$ distributions in the bins $0.45 < \gamma_{true} < 0.6$ and $0.75 < \gamma_{true} < 0.9$, respectively. As we can see, the non-parametric

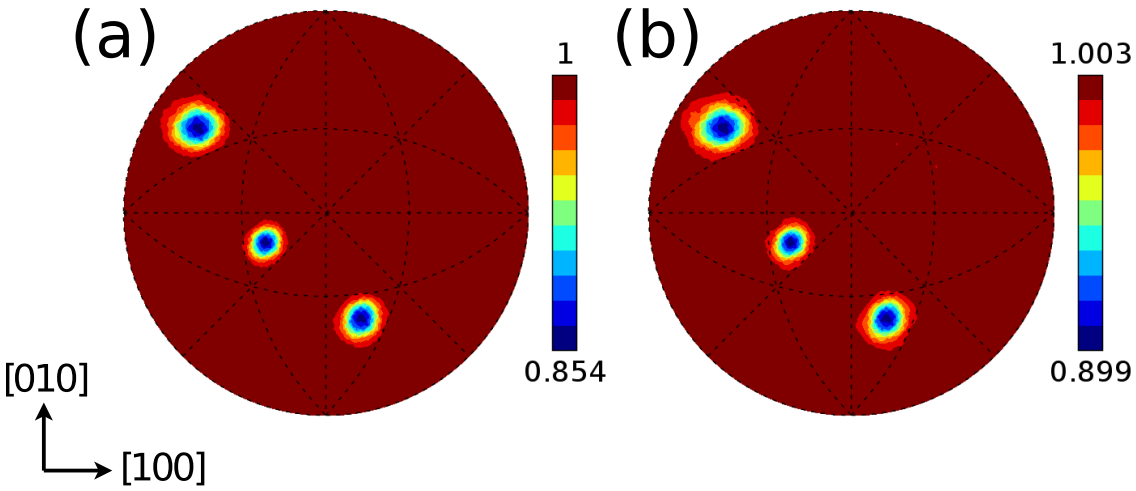

Figure 3.2: Stereographic projections of the normalized grain boundary energy distribution (GBED) for the Σ7 misorientation of **DA06**. (a) Ground truth; (b) reconstructed by the non-parametric method.

method results have smaller bias and variance than the conventional method in almost every bin.

3.4.2 Results on a clustered dataset

Sometimes in real materials grain boundaries are not uniformly distributed in the five-parameter space. For example, the data will be clustered in a textured sample, and we may want to reconstruct the energy of grain boundaries in those datasets. In these cases, we actually only need the grain boundary energy function values in constrained regions of the five-parameter space. While the conventional method still tries to reconstruct the grain boundary energy function on the whole five-parameter space, the non-parametric approach inherently exploits the clustered structure in the datasets. Therefore, we can expect that the non-parametric approach can use less data but get a better reconstruction result than the conventional method.

Dataset **DB** is an extreme case of a clustered dataset with all grain boundaries located in a 2D subspace of the five-parameter space. We tested both the conventional method and the non-parametric method on this dataset, and the reconstructed energies are shown in Figure 3.5. In Figure 3.5, all grain boundaries are ordered by their true energy γ_{true} so that smaller grain ID corresponds to lower γ_{true}. We can see that the non-parametric method can reconstruct the energies of **DB** fairly well. Figure 3.6 shows the mean value and standard deviation of the difference between reconstructed energy and the ground truth $\gamma_{rec} - \gamma_{true}$ for grain boundaries with different γ_{true}.

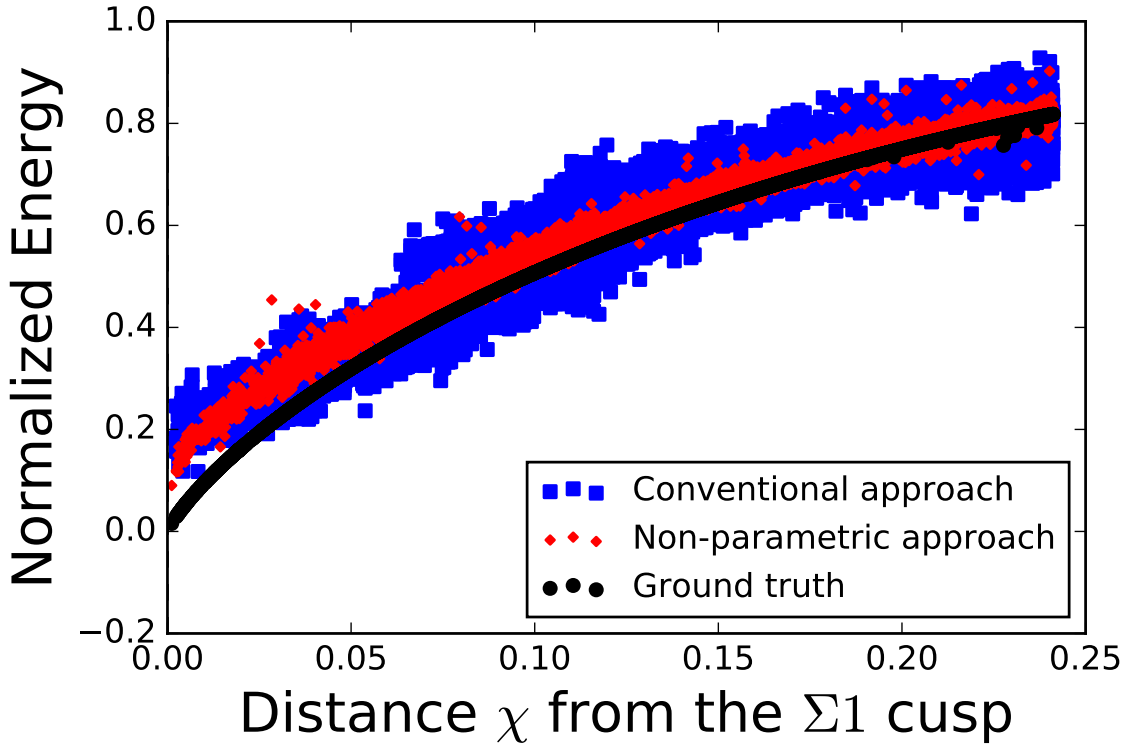

Figure 3.3: Comparison of the conventional method and the non-parametric method reconstruction results near the $\Sigma 1$ cusp of **DA06**. The distance χ is defined in Section 3.1.1. Every point represents one grain boundary, blue points are results of the conventional approach, red points are results of the non-parametric approach, and the ground truth are represented by black points. Reconstructed energies have been normalized so that they have the same average value as the ground truth distribution.

3.4.3 Effects of the dataset size

It is important to know how dataset size influences the reconstruction's performance. To investigate this, we reconstructed the grain boundary energies using only the first $k \times 10^4$ triple junctions in **DA26**, where $k = 1, 3, 6, 12, 14, 16, 17, 18,$ and 26. The reconstruction results on these subsets are shown in Figure 3.7. Because the reconstruction errors are different for the cusp and the remaining region, we seperated the grain boundaries into two categories, $\gamma_{true} > 0.9$ and $\gamma_{true} < 0.9$, which correspond to the grain boundaries that are outside and inside of the cusps, respectively. The reconstruction error is measured by the square root of mean squared error $\sqrt{\overline{(\gamma_{rec} - \gamma_{true})^2}}$, which includes the effect of bias and variation. As expected, the error of the non-parametric method decreases when the dataset size increases. Surprisingly, the errors in the conventional method are sometimes greater in larger datasets. We will discuss this further in Section 3.6.

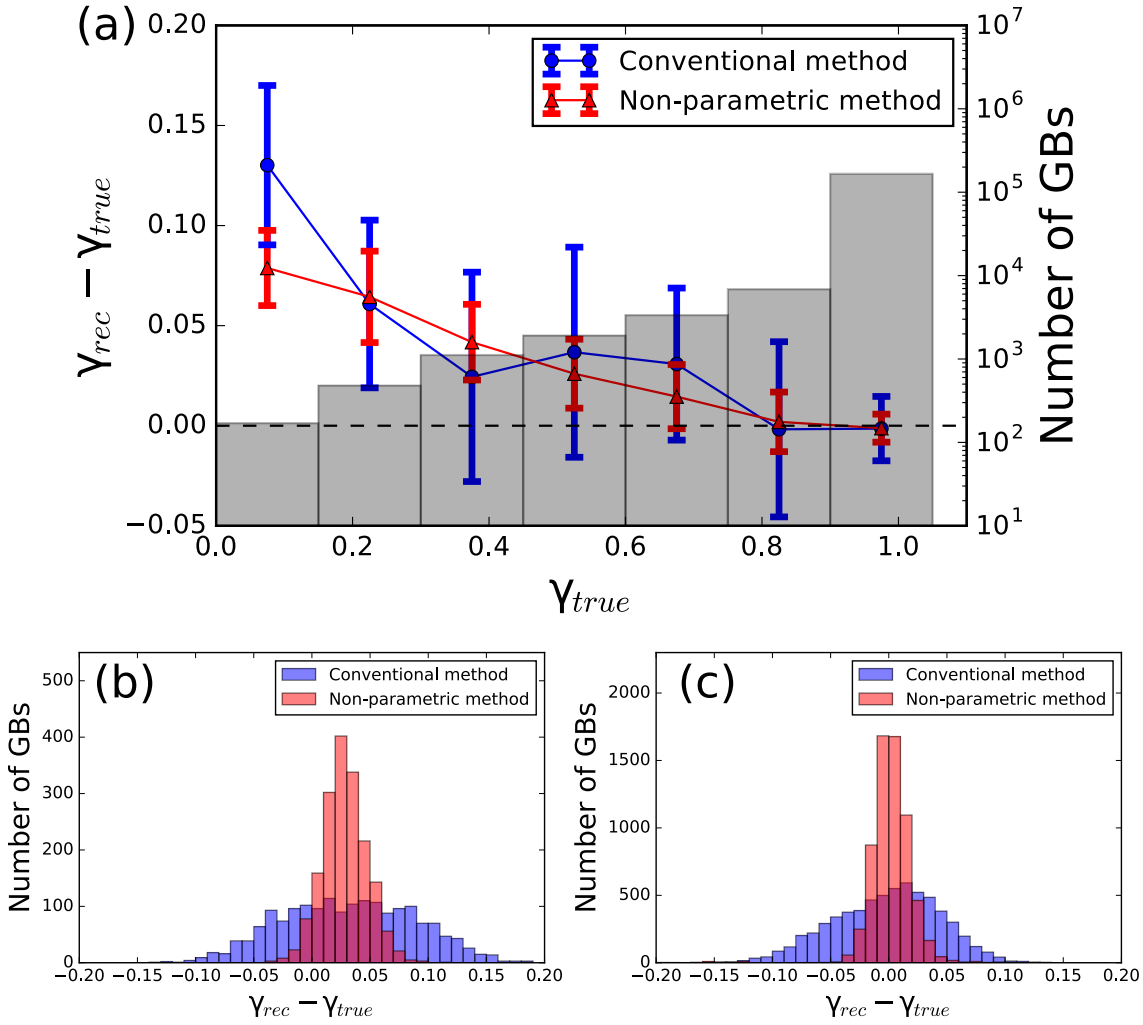

Figure 3.4: Reconstruction results of the conventional method and the non-parametric method on **DA06**. We calculated the difference between reconstructed energy and the ground truth $\gamma_{rec} - \gamma_{true}$ for every grain boundary. All grain boundaries are binned by their true energy γ_{true}, and for each bin we calculated the mean value and standard deviation of $\gamma_{rec} - \gamma_{true}$, which is shown in (a). The gray bars in (a) are the number of grain boundaries in the bins. The histograms in (b) and (c) are the detailed $\gamma_{rec} - \gamma_{true}$ distributions in the bin $0.45 < \gamma_{true} < 0.6$ and bin $0.75 < \gamma_{true} < 0.9$, respectively. Blue line and bars are results of the conventional method, and red line and bars are results of the non-parametric method.

3.4.4 Effects of measurement noise

Experimental data always has measurement noise. For a microstructure measured by EBSD or HEDM, the uncertainty of grain orientation is negligible, and the main error is the triple junction geometry. To analyze the reconstruction robustness against

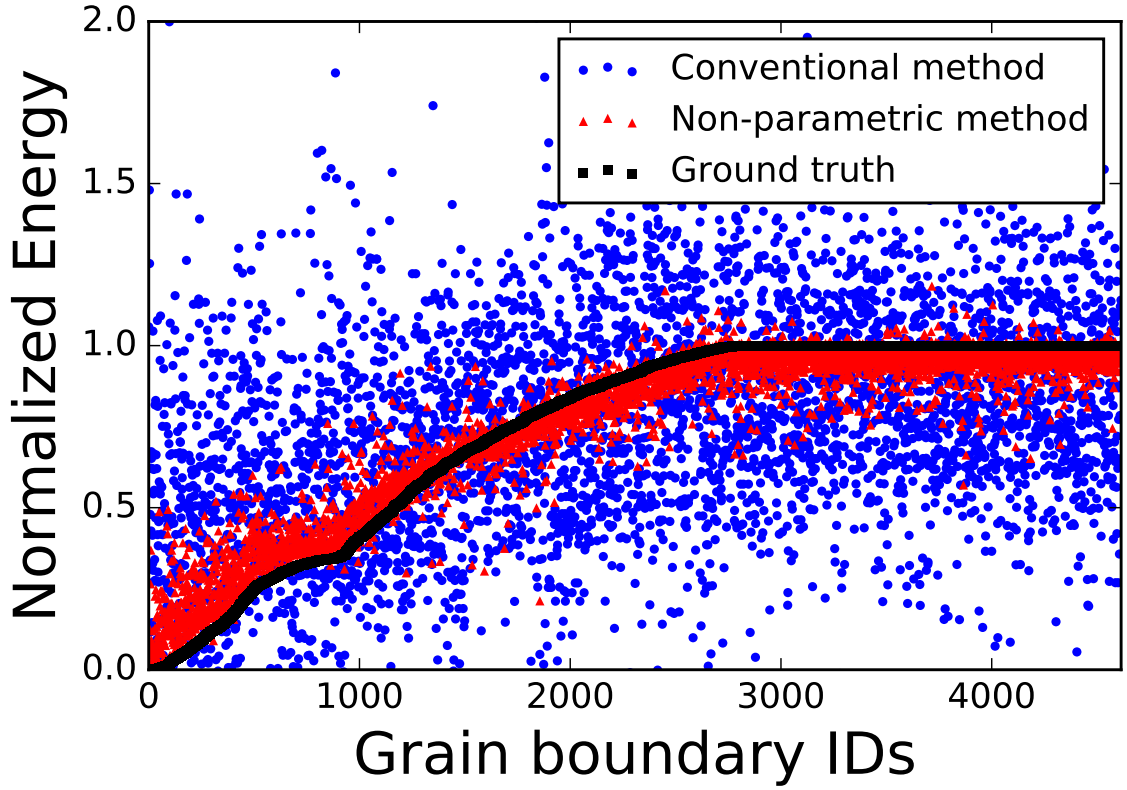

Figure 3.5: Comparison of the conventional method and the non-parametric method reconstruction results of **DB**. All grain boundaries are ordered by their true energy γ_{true} so that smaller grain ID corresponds to lower γ_{true}. Every point represents one grain boundary, blue points are results of the conventional method, red points are results of the non-parametric method, and the ground truth is represented by black points. Reconstructed energies have been normalized so that they have the same average value as the ground truth distribution.

the error in measuring the triple junction geometry, we artificially added noise to **DA06**. For every triple junctions in **DA06**, we applied a rotation $(\delta\phi, \delta\theta, 0)$ to the junction direction, where $\delta\phi$ and $\delta\theta$ are randomly generated from a Gaussian distribution with a zero mean. We tested both the conventional method and the non-parametric method on different noisy datasets with different σ (in units of degrees) as the standard deviation of the Gaussian distribution. Figure 3.8 demonstrates the reconstruction errors.

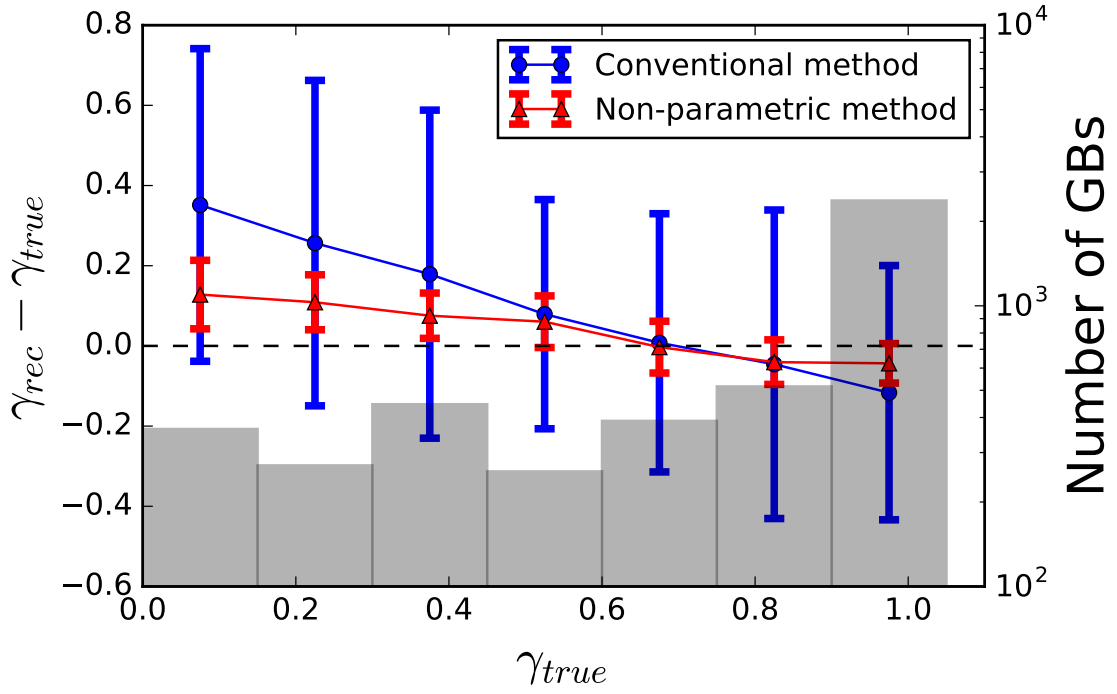

Figure 3.6: Reconstruction results of the conventional method and the non-parametric method on **DB**. We calculated the difference between reconstructed energy and the ground truth $\gamma_{rec} - \gamma_{true}$ for every grain boundary. All grain boundaries are binned by their true energy γ_{true}, and for each bin we calculated the mean value and standard deviation of $\gamma_{rec} - \gamma_{true}$. The gray bars are the number of grain boundaries in the bins.

3.5 Application to a MgO Dataset

To demonstrate the efficacy of this method for analyzing experimental data, we applied the non-parametric approach to data from an MgO ceramic, originally reported in [65]. The details of the sample preparation, experimental procedure, and data acquisition can be found in earlier publications [77, 73, 65]. The three-dimensional orientation data made it possible to determine the geometries of 1.9×10^4 triple junctions and these measurements were used as input for the grain boundary energy reconstruction.

In general, the reconstruction errors depend on the energy models. If we assume that the analysis in Section 3.4.3 and Section 3.4.4 still hold for the real grain boundary energy function of MgO, then the reconstruction error of normalized grain boundary energy is less than 0.05 because, for this experimental data, $k = 1.9$ in Figure 3.7 and $\sigma < 10^\circ$ in Figure 3.8.

Figure 3.9 shows stereographic projections of the reconstructed grain boundary energy distribution (GBED) produced by the new method, the conventional method,

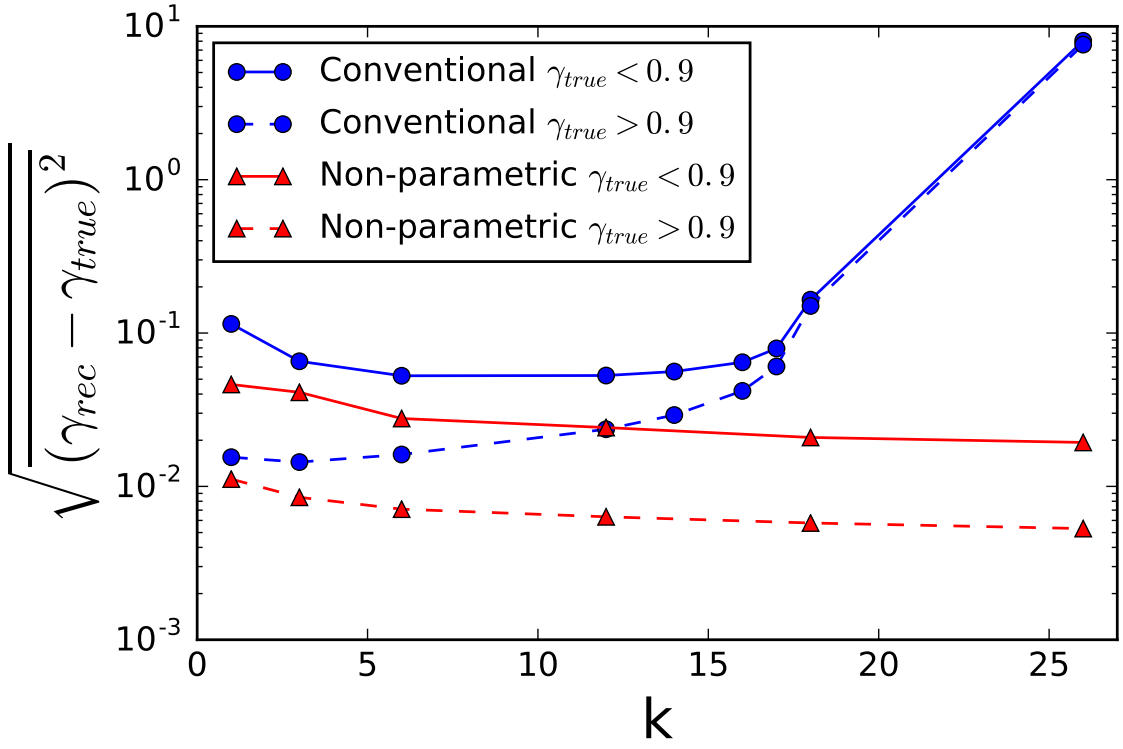

Figure 3.7: Reconstruction errors using only subsets of **DA26** with different sizes ($k \times 10^4$). Based on the ground truth energies, the grain boundaries in each subset are devided into two categories, $\gamma_{true} > 0.9$ (dashed line) and $\gamma_{true} < 0.9$ (solid line), which are outside and inside of cusps, respectively. Blue lines are results of the conventional method, and red lines are results of the non-parametric method.

and grain boundary character distribution (GBCD) for MgO for a misorientation 5° around [1 1 0]. The GBCD and GBED were reported in an earlier publication [65]. The GBCD is presented in units of multiples of a random distribution (relative areas). The two grain boundary energy distributions agree in some places. For example, the maximum energy of both distributions is near the position of twist boundaries (marked by circles). However, they disagree at the position of the symmetric tilt boundary (marked by a square), which has a near minimum energy in the GBED produced by the non-parametric method and is a local maximum in the GBED produced by the conventional method. Note that the GBCD has a maximum at the symmetric tilt position. Based on the well-known inverse correlation between the GBED and the GBCD [12], a minimum energy at this position is expected, consistent with the result of the non-parametric method.

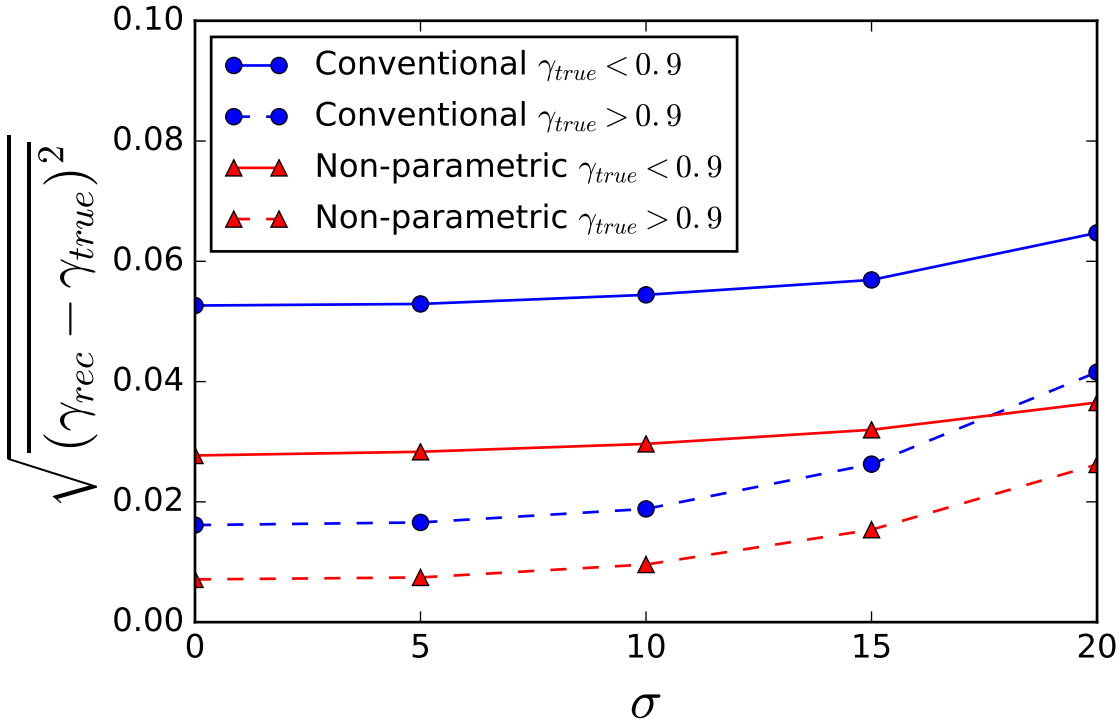

Figure 3.8: Reconstruction errors of the conventional method and the non-parametric method on the dataset **DA06** with noises of different σ values (in units of degrees), which are the standard deviations of the Gaussian noise that were applied to the triple junction directions. Based on the ground truth energies, the grain boundaries in each dataset are devided into two categories, $\gamma_{true} > 0.9$ (dashed line) and $\gamma_{true} < 0.9$ (solid line), which are outside and inside of cusps, respectively. Blue lines are results of the conventional method, and red lines are results of the non-parametric method.

3.6 Discussion

We demonstrated in Figure 3.4 that both the conventional method and the non-parametric method perform well on a normal size dataset **DA06**. For most grain boundaries, the reconstruction errors are less than 0.1. Cusps are smoothed in the reconstruction, i.e. reconstructed energies of grain boundaries in the cusps are biased to be larger than their true energies. Although the measurement error of triple junction geometries depends on the method of data preprocessing, $\sigma < 10^\circ$ is a reasonable estimation. As shown in Figure 3.8, both methods are robust below this level of noise. For the non-parametric method, the reconstruction error is below 0.04 for grain boundaries inside the cusps and below 0.02 outside the cusps.

An advantage of the non-parametric method over the conventional method is that it utilizes the clustered structure in the datasets, so that it can reconstruct

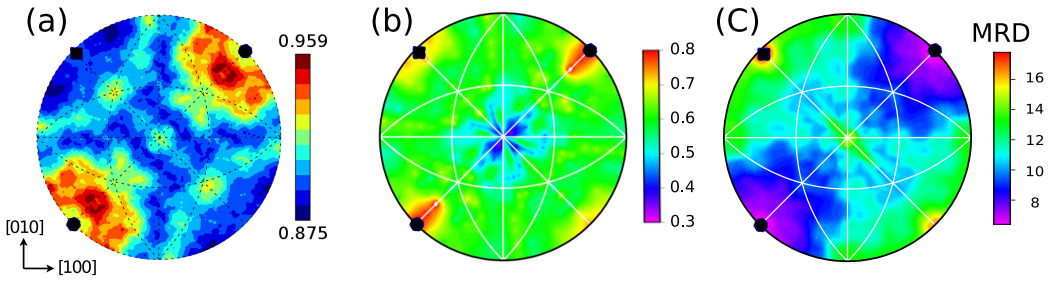

Figure 3.9: Stereographic projections of the (a) GBED reconstructed using the non-parametric method, (b) GBED reconstructed using the conventional method, and (c) grain boundary character distribution (GBCD) for grain boundaries in MgO with a 5° misorientation around [1 1 0]. The GBCD has units of multiples of a random distribution and the GBEDs are normalized energies.

the grain boundary energies of a clustered dataset even if it only contains a small number of triple junctions, which is not possible (without creating a new sub-space for discretization) using the conventional method. As demonstrated by Figure 3.5 and Figure 3.6, the non-parametric method reconstructed the grain boundary energies in **DB** with an error of less than 0.2. Therefore, the energy in that subspace is recovered with reasonable accuracy.

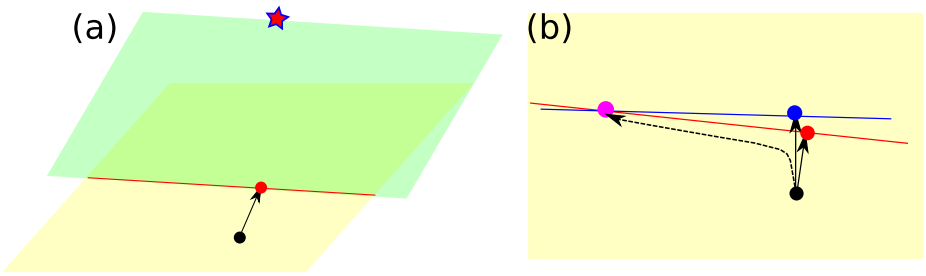

Figure 3.10: Geometric interpretation. (a) Red star is the true solution, yellow plane is the linear span of the basis functions, green plane is the subspace that satisfies all triple junction equilibrium equations, red line is the overlap of yelow plane and green plane, black dot is the iteration starting point, red dot is the approximated solution found in the yellow plane, which is at the red line and close to the black dot. (b) The yellow plane is the linear span of the basis functions, one set of equilibrium equations constrain the solution on the red line, another set of equations constrain the solution on the blue line, black dot is the iteration starting point. If the dataset only contains the first set of equations, then the approximate solution is at red dot; and if the dataset only contains the second set of equations, then the approximate solution is at blue dot. However, if the dataset contains both, then the approximate solution is at purple dot, which is far away from the true solution.

The effect of dataset size is interesting. As shown in Figure 3.7, the reconstruction

error of the conventional method increases when the number of triple junctions increases in some range. A geometric interpretation is presented in Figure 3.10. As we showed above, the conventional method finds the coefficients of a set of basis functions which can span a linear space (yellow plane), and generally the true capillarity vector function (red star) is not in this space, and the solution we find is an approximation (red dot), which satisfies the force balance equations of all the triple junctions. In most cases, the problem is under-determined, so the solution always exists but is not unique. Choosing a good starting point (black dot) for the gradient descent iteration makes the problem converge to a solution (red dot) that can approximate the ground truth (red star). However, if we have more triple junctions, there are more constraints and the solution (purple dot) may not be close to the ground truth anymore. Recently, similar phenomena, called "double descent", are discovered and investigated in statistics and machine learning.

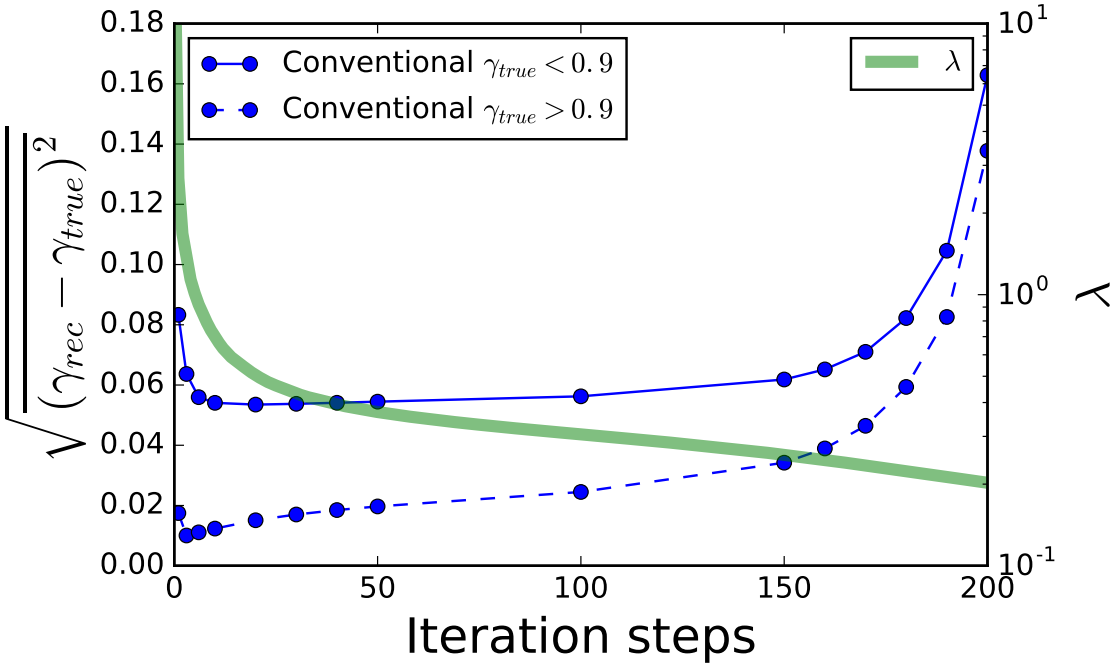

Figure 3.11: Errors of the intermediate reconstruction results using the conventional method on dataset **DA26**. Based on the ground truth energies, the grain boundaries are divided into two categories, $\gamma_{true} > 0.9$ (dashed line) and $\gamma_{true} < 0.9$ (solid line), which are outside and inside of cusps, respectively. The green line is λ, which is defined as $\|\mathbf{AX}\|^2/\|\mathbf{X}\|^2$, where $\mathbf{A}$ and $\mathbf{X}$ are the equation coefficients and variables in Eq. 3.2.

One way to address this problem is to stop the iterative solution before convergence. The conventional method converges after about 2000 iteration steps for the large size dataset **DA26**. Figure 3.11 demonstrates the errors of some intermediate

results in the first 200 iteration steps. As we expected, $\lambda = \|\mathbf{AX}\|^2/\|\mathbf{X}\|^2$ keeps decreasing, where $\mathbf{A}$ and $\mathbf{X}$ are the equation coefficients and variables in Eq. 3.2. The reconstruction errors decrease in a few iteration steps at first, but increase dramatically after about 150 interation steps. Therefore, for the dataset **DA26**, if we stop before 150 iteration steps, the reconstruction results will be close to the ground truth. The grain boundary energy distribution (GBED) for the $\Sigma 11$ misorientation of the intermediate reconstruction is shown in Figure 3.12. After 10 iterations, the conventional approach shows a GBED that is expected for the $\Sigma 11$ misorientation. However, it has not converged yet. After 200 steps, the result deviates from the ground truth. So, the number of iterations is an important hyper-parameter for the conventional reconstruction method. The non-parametric approach does not have the same problem as the conventional method, because it does not limit the solution to a subspace. So, as shown in Figure 3.7, the reconstruction error of the non-parametric method decreases as the number of triple junctions increases, which is as expected.

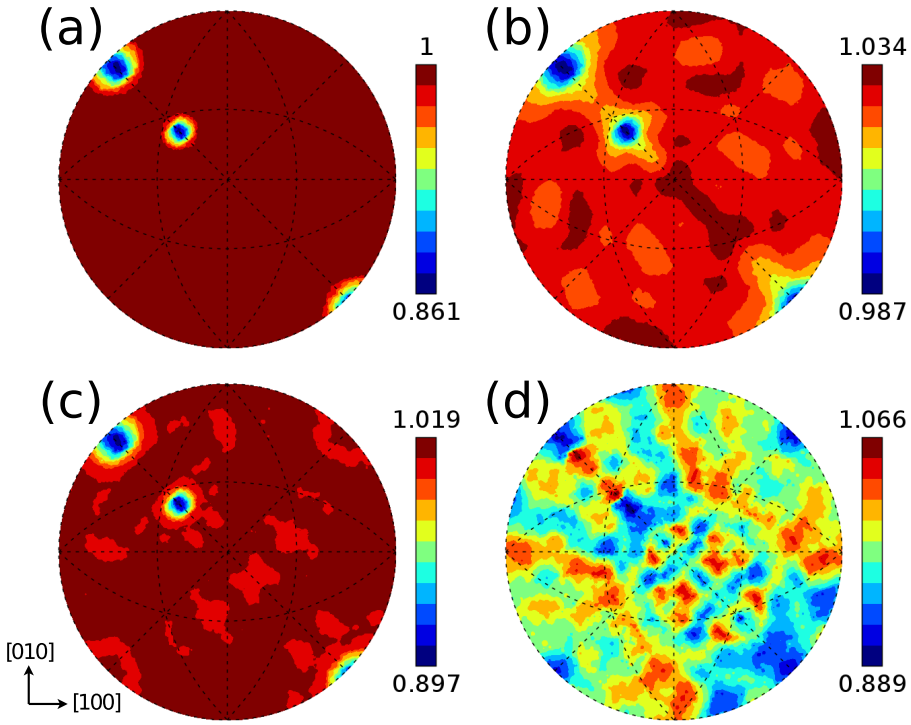

Figure 3.12: Stereographic projections of the GBED for the $\Sigma 11$ misorientation at different iteration steps. (a) Ground truth; (b) step 1; (c) step 10; (d) step 200. (b)-(d) are reconstructed by the conventional approach using dataset **DA26**.

Finally, let us note that in this non-parametric framework, the regularization term is based on the "distance" between grain boundaries. The choice of the metric affects the regularization term and, in consequence, the reconstruction results. The definition of grain boundary distance in Section 3.1.1 follows [64], but other metrics have been

discussed in the literature [78, 79, 80, 81, 82]. Moreover, with $1/\chi_{ij}$ as the weight in the regularization term, the singularity at $\chi_{ij} = 0$ may cause problems on clustered data sets. Testing alternative metrics and regularization terms for the non-parametric framework will be the subject of future research.

Chapter 4

Measuring Intragranular Strain and Orientation with nf-HEDM

4.1 Introduction

Near-field High Energy Diffraction Microscopy (nf-HEDM) generates maps of microstructure by imaging multiple diffracted beams from each crystal orientation in an illuminated sample volume as the sample rotates in a monochromatic, high energy X-ray beam. Far-field HEDM adds grain averaged strain states. Recent reviews of both HEDM variants and combined measurements are available in [83, 84] (as well as in a forthcoming review J. Bernier, R.M. Suter, A.D. Rollett, J. Almer, to be published in Annual Reviews of Materials Research). While standard parlance refers to regions of relatively uniform orientation as "grains", the forward modeling approach to reconstructing the orientation field [24, 4] from nf-HEDM measurements assumes only that a well defined orientation exists within each resolved volume element or voxel. This voxel-by-voxel analysis yields detailed information about intra-granular orientation variations that arise from mechanical deformation [85, 86, 87] and are mitigated by thermal annealing [88]. The far-field measurement yields grain averaged quantities such as orientation, center-of-mass, and elastic strain state.

Substantial difficulties arise in attempting to extract local strain states within grains inside of bulk materials. Recent work at the Spring-8 synchrotron in Japan [89] has succeeded in using a point-focused X-ray beam combined with a conical slit to isolate diffraction from sub-grain sized volume elements, or voxels, and then to extract such strain information. A three dimensional volume was characterized by rastering the sample relative to the slit and the sample rotation axis. Not surprisingly, the measurement found that strain heterogeneity was substantially larger than that implied by grain averaged characterizations. Both the data collection and analysis time are substantial since 3D information requires collecting a 2D raster of diffraction images.

An advantage of nf-HEDM data collection is that it uses a line-focused beam that

illuminates a planar cross-section of the sample so as to parallelize data collection from many voxels. However, with its small (5–15 mm) sample-to-detector distance, the measurement does not have high resolution of scattering angles, 2θ. Nevertheless, it is demonstrated in [90] that fractional changes in lattice constant by $\sim 10^{-3}$ yield significant changes in a completeness or confidence parameter that characterizes the amount of overlap between orientation optimized microstructures and the detector image data sets. Below, we describe systematic studies of voxel-by-voxel strain optimization applied to a synthetic nf-HEDM data set and some preliminary results on a real Ti7Al sample. Sensitivity to strain is obtained by resolving diffraction at small sample rotation intervals, $\delta\omega$ instead of with 2θ resolution.

4.2 Preliminaries

4.2.1 Review of X-ray Diffraction Theory

In this section, we will briefly review the physics model we use for the nf-HEDM experiment setups. Readers should refer to textbooks [91] if they want to learn the scattering physics comprehensively.

Within coherence time and coherence length, the incident X-ray can be approximated by plane wave $\mathbf{E}_i(\mathbf{x}) = E_0 \exp(i\omega t - i\mathbf{k}_i \cdot \mathbf{x})\hat{z}$, where $\mathbf{k}_i$ is the incoming wave vector and $\hat{z}$ is the polarization direction. Under Born approximation, the scattering of an ensemble of electrons, the sample, is simply calculated by summing up all corresponding diffracted spherical waves. Since the detector is far away from the sample comparing to the wavelength, the diffracted X-ray amplitude at $\mathbf{x}$ can also be approximated by the plane wave

$$\begin{aligned}\mathbf{E}_o(\mathbf{x}) &\propto \int \exp\{i\omega t - i\mathbf{k}_i \cdot \mathbf{r} - i\mathbf{k}_o \cdot (\mathbf{x} - \mathbf{r})\}\rho(\mathbf{r})d\mathbf{r}^3 \\ &= \exp(i\omega t - i\mathbf{k}_o \cdot \mathbf{x}) \int \exp\{i(\mathbf{k}_o - \mathbf{k}_i) \cdot \mathbf{r}\}\rho(\mathbf{r})\mathbf{r}^3, \end{aligned} \tag{4.1}$$

where $\mathbf{k}_o$ is the outgoing wave vector, $\mathbf{r}$ is the scattering source position, $\rho(\mathbf{r})$ is the electron density distribution. We define $\mathbf{Q} = \mathbf{k}_o - \mathbf{k}_i$.

For most crystal materials, their atoms are placed in a periodical lattice structure which has the translation symmetry. Its symmetry operators can be represented by three translation vectors, which form the repeating unit called unit cell. For example, the hexagonal unit cell of Ti7Al (used in this work) can be described by following three vectors:

$$\mathbf{a} = a \begin{bmatrix} 1 \\ 0 \\ 0 \end{bmatrix}, \mathbf{b} = a \begin{bmatrix} \cos\frac{2\pi}{3} \\ \sin\frac{2\pi}{3} \\ 0 \end{bmatrix}, \mathbf{c} = c \begin{bmatrix} 0 \\ 0 \\ 1 \end{bmatrix}$$

with a, c being edge lengths. The position of every unit cell can be written as $\mathbf{R}_n = m_1\mathbf{a} + m_2\mathbf{b} + m_3\mathbf{c}$ where $n = (m_1, m_2, m_3)$ are three integers. The reciprocal lattice

vectors (RLV) $\mathbf{a}', \mathbf{b}', \mathbf{c}'$, are calculated in the usual way from the these vectors [92], e.g.

$$\mathbf{a}' = 2\pi \frac{\mathbf{b} \times \mathbf{c}}{\mathbf{a} \cdot (\mathbf{b} \times \mathbf{c})},$$

and cyclic permutations. A general RLV can be defined as $\mathbf{G}_{hkl} = h\mathbf{a}' + k\mathbf{b}' + l\mathbf{c}'$, where the indices $(h\,,\,k\,,\,l)$ are three Miller integers.

For all the calculation in this chapter, there are three different reference frames, lab frame, sample frame and crystal frame. Lab frame is the basic reference frame in which Eq. (4.1) is defined. The sample frame is the reference frame that is fixed to the sample. Crystal frame is the reference frame of the local crystal structure with axes oriented with the convention unit cell. So the vectors $\mathbf{a}, \mathbf{b}, \mathbf{c}, \mathbf{R}_n, \mathbf{a}', \mathbf{b}', \mathbf{c}', \mathbf{G}_{hkl}$ are actually defined in the crystal frame. Vectors in different reference frames can be easily transformed given the relationships of their basis vectors. Therefore, single crystal material will have $\rho(\mathbf{r}) = \rho(\mathbf{r} + \mathbf{R}_n^{\text{lab}})$, and the diffracted X-ray will be

$$\mathbf{E}_o(\mathbf{x}) \propto \exp\left(i\omega t - i\mathbf{k}_o \cdot \mathbf{x}\right) \sum_n \exp\left\{i\mathbf{Q} \cdot \mathbf{R}_n^{\text{lab}}\right\} \int_{\text{unit cell}} \exp\left\{i\mathbf{Q} \cdot \mathbf{r}\right\} \rho(\mathbf{r}) d\mathbf{r}^3. \quad (4.2)$$

in which sum over n is over a large number of unit cells defined by the coherence lengths of the experimental setup and this leads to sharp Bragg peaks when $Q = G_{hkl}^{\text{lab}}$. Therefore, the diffracted X-rays are on the direction of $\mathbf{k}_o = \mathbf{k}_i + \mathbf{G}_{hkl}^{\text{lab}}$. In addition, in the elastic approximation we have the constraint that $\|\mathbf{k}_o\| = \|\mathbf{k}_i\|$.

4.2.2 Deformation Gradient

Nine independent parameters define a crystal of a given phase, three for lattice rotation and six for lattice strain. Following the notation in [93], within a scattering volume, we can approximate the deformation by a linear transformation that takes material vectors in the reference lattice frame to the sample frame:

$$\mathbf{r}' = \mathbf{F} \cdot \mathbf{r} + \mathbf{p}, \quad (4.3)$$

where $\mathbf{r}$ is a material position vector expressed in the local and undeformed crystal frame, $\mathbf{r}'$ is the material vector in the deformed configuration in the sample, including a translation, $\mathbf{p}$, and a tensor, $\mathbf{F}$, describing the deformation gradient. $\mathbf{F}$ can be polar decomposed to a pure rotation (proper orthogonal tensor) and a pure strain (symmetric positive-definite tensor), i.e. $\mathbf{F} = \mathbf{V} \cdot \mathbf{R}$ where $\mathbf{V}$ is symmetric and positive-definite and $\mathbf{R}$ is proper orthogonal. $\mathbf{R}$ is the crystal orientation and $\mathbf{S} = \mathbf{V} - \mathbf{I}$ is the lattice strain.

As described above, the crystal orientation and strain are defined in lab reference frame, which is in real space, however X-ray diffraction measurements are directly related to reciprocal lattice of the crystal lattice. We need to find out how the deformation gradient affects the reciprocal lattice.

In sample frame, a RLV is $\mathbf{G}_{hkl}^{\text{sample}} = \mathbf{D}\bar{\mathbf{O}}\mathbf{G}_{hkl}$, where $\bar{\mathbf{O}}$ is an approximate orientation matrix, and the "distortion" matrix $\mathbf{D} = \mathbf{I} + \delta$ is a small perturbation about the approximate orientation. From last section, we know that $\mathbf{G}_{hkl}^{\text{lab}}$, which can be easily obtained from $\mathbf{G}_{hkl}^{\text{sample}}$, determines the direction of diffracted X-rays. Since we can calculate all $\mathbf{G}_{hkl}$ from the crystal lattice parameters, it is possible to recover the matrix $\mathbf{D}\bar{\mathbf{O}}$ from X-ray diffraction measurements.

For any RLV $\mathbf{a}'$ and its corresponding real-space unit cell vector $\mathbf{a}$, we have the relationship that $[\mathbf{a}']^T\mathbf{a} = 2\pi$. Since this equation holds independent of deformation, we have

$$\begin{aligned}\left[\mathbf{D}\bar{\mathbf{O}}\mathbf{a}'\right]^T[\mathbf{F}\mathbf{a}] &= [\mathbf{a}']^T[\mathbf{a}] \\ \Rightarrow (\mathbf{D}\bar{\mathbf{O}})^T\mathbf{F} &= \mathbf{I} \\ \Rightarrow \mathbf{F} &= (\mathbf{D}\bar{\mathbf{O}})^{-T}\end{aligned}$$

From the X-ray diffraction measurements we can get the value of $\mathbf{D}\bar{\mathbf{O}}$, and then we can do a polar decomposition on $(\mathbf{D}\bar{\mathbf{O}})^{-T}$ to get the strain and orientation.

4.2.3 nf-HEDM Measurements and Forward Modeling

In principle, nf-HEDM is an extension of rotating crystal method, whose experiment setup geometry is shown in Figure 4.1. The incoming X-ray $\mathbf{k}_i$ is in X direction, and the sample along with each RLV, $\mathbf{G}^{\text{sample}}$, is rotated around the Z-axis. Assuming the sample frame is the same as lab frame when $\Omega = 0$, for any specific RVL $\mathbf{G}$ in the sample frame, we can calculate at what Ω values the diffraction will happen. Some important quantities are

$$\begin{aligned}\omega_0 &= \arctan\frac{\mathbf{G}_x}{\mathbf{G}_y}, & \theta &= \arcsin\frac{\|\mathbf{G}\|}{2\|k\|}, & \chi &= \arccos\frac{\mathbf{G}_z}{\|\mathbf{G}\|}, \\ \phi &= \arccos\frac{\sin(\theta)}{\sin(\chi)}, & \eta &= \arcsin\frac{\sin(\chi)\sin(\phi)}{\cos(\theta)}, \\ \omega_a &= \omega_0 + \frac{\pi}{2} - \phi, & \omega_b &= \omega_0 + \frac{\pi}{2} + \phi\end{aligned}$$

The diffraction happens when $\Omega = \omega_a$ and $\Omega = \omega_b$, and the diffracted X-ray direction is

$$\overrightarrow{SDir} = \begin{bmatrix} \cos(2\theta) \\ \sin(2\theta)\sin(\eta) \\ \sin(2\theta)\cos(\eta) \end{bmatrix}$$

What makes nf-HEDM special is its "near field" setup, which does not mean the detector is close to the sample comparing with wave length (called near-field optics) but with sample size. In a typical setup, the incoming X-ray illuminates a

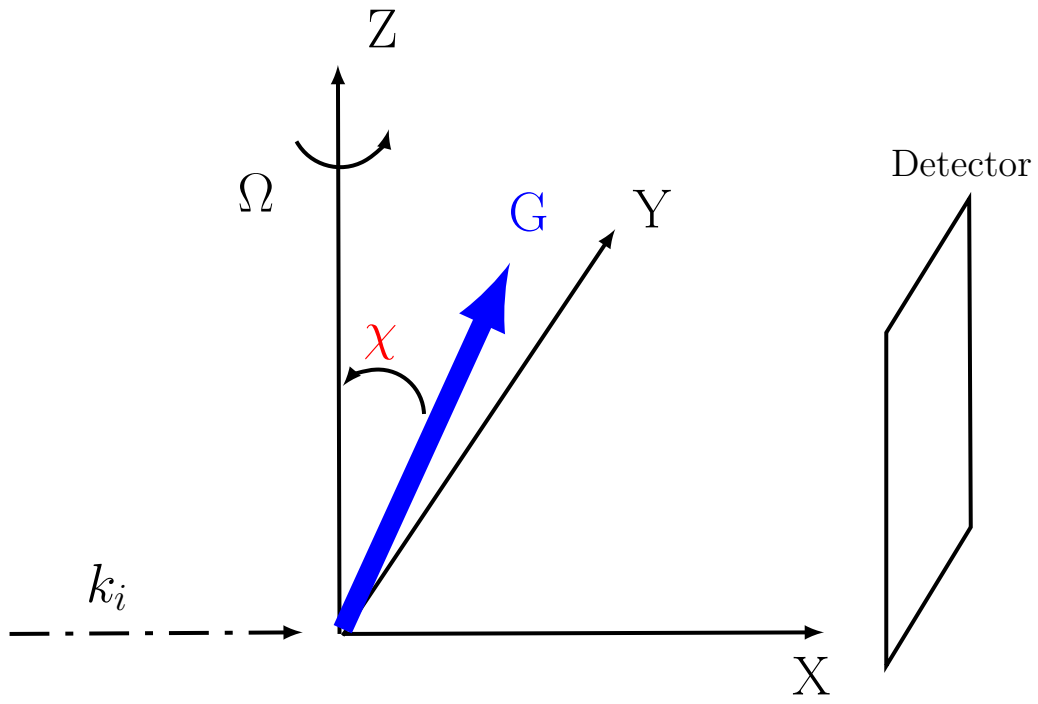

Figure 4.1: The geometry of rotating crystal method. The incoming X-ray $\mathbf{k}_i$ is in X direction. As the sample is rotated around the Z-axis, the RVL $\mathbf{G}^{\text{sample}}$ is also rotated around the Z-axis.

slice of the sample that perpendicular to the rotation axis, the detector to sample distance is $\approx 10\,\text{mm}$, the sample size is $\approx 1\,\text{mm}$, the wave length is $\lesssim 1\,\text{Å}$, and the coherence length is $< 1\,\mu\text{m}$. Therefore an appropriate way to model the scattering process is: discretizing the illuminated region into voxels (or grid), each voxel has its own crystal orientation (and even strain), the X-ray diffracted from each voxel can be approximated by geometric optics (represented by a straight line), the X-ray diffracted from different voxels within a grain are incoherent so their intensities on the detector pixel can directly summed up.

Assuming a voxel is at (x, y, z) in the sample frame, the detector origin is at $\mathbf{O}$ in the lab frame and its normal direction is $\hat{e}_n$, the row and column direction of pixels on the detector are $\hat{e}_J$ and $\hat{e}_K$. From previous calculation, while diffracting, the distance between the scattering voxel and the detector is

$$Dist = \hat{e}_n \cdot (\mathbf{O} - \begin{bmatrix} \cos(\omega_{a(b)})x - \sin(\omega_{a(b)})y \\ \cos(\omega_{a(b)})y + \sin(\omega_{a(b)})x \\ z \end{bmatrix}).$$

The diffracted X-ray intersects the detector plane at

$$\overrightarrow{XPos} = \frac{Dist}{\hat{e}_n \cdot \overrightarrow{SDir}} \overrightarrow{SDir} + \begin{bmatrix} \cos(\omega_{a(b)})x - \sin(\omega_{a(b)})y \\ \cos(\omega_{a(b)})y + \sin(\omega_{a(b)})x \\ z \end{bmatrix}.$$

So the hit pixel on detector plane has the coordinate

$$\begin{aligned} J &= \hat{e}_J \cdot (\overrightarrow{XPos} - \mathbf{O}) \\ K &= \hat{e}_K \cdot (\overrightarrow{XPos} - \mathbf{O}) \end{aligned} \tag{4.4}$$

The collected data from nf-HEDM is the set of diffraction images at successive Ω steps, the typical integration interval for each frame is $\delta\omega = 1^\circ$ and total of 180 frames are collected. The forward modeling method [24, 4] is used for reconstructing microstructure from these diffraction images. The basic idea is:

Step 1: Binarizing the diffraction images so that every pixel is either hit or not hit at each Ω frame.

Step 2: For a voxel, testing different crystal orientations and use Eq. (4.4) to calculate the hit pixels for all G_{hkl}, choosing the orientation whose hit ratio with the binarized experimental images is the highest.

Step 3: Repeat Step 2 for every voxel.

Readers can refer to [34, 4, 94, 38] for more details.

4.2.4 Motivation for Strain Reconstruction

Previous nf-HEDM reconstructions have been based on nominal, unstrained lattice parameters meaning that $\mathbf{D}$ and $\mathbf{V}$ are identity matrices and therefore $\mathbf{R} = \bar{\mathbf{O}}$. However, in some sample states, the effects of elastic strain have been noted as a reduction in overlap between optimized simulated diffraction and the measurements [90, 85, 95]. The effect is made more dramatic by changing the sample rotation integration interval from the traditional $\delta\omega = 1^\circ$ to 0.25° (as is now conventional) or to 0.05°. As shown in Fig. 4.2, for a Ti7Al sample under 200 MPa tensile load, different parts of an example diffraction peak separate and appear in three successive $\delta\omega$ frames while prior measurement of the same peak under low load exhibits a single peak in a single frame. The grain image splitting is interpreted as a sign of intra-granular strain and/or orientation variation. This chapter presents a scheme for reconstructing these voxel-by-voxel variations from the > 100 Bragg peaks collected from each grain over a rotation range of $\Delta\omega = 180^\circ$. Tests are performed using a simulated data set based on the Ti7Al crystal structure.

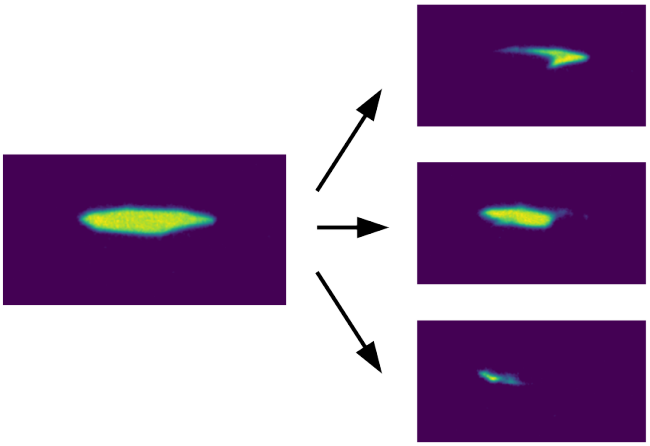

Figure 4.2: An example of a diffraction peak from a single grain in a Ti7Al polycrystal under low (left) and 200 MPa (right) load. Each frame corresponds to a $\delta\omega = 0.05^\circ$ sample rotation interval. At left, the entire grain projects intensity within a single frame whereas under load, the projected image is split between three adjacent images indicating a variation in the local unit cell orientation and/or strain.

4.3 Intragranular Deformation Gradient Field Reconstruction

The goal of our reconstruction code is to reconstruct $\mathbf{D}\bar{\mathbf{O}}$. We use the reconstruction result from the standard forward modeling method, $\bar{\mathbf{O}}$, as the "initial guess" and try to reconstruct the distortion $\mathbf{D}$ that can correctly reproduce the intensity profile of every diffraction peak. The use of observed intensities in this reconstruction goes beyond both the binary intensity patterns used in standard orientation reconstructions and the observed splitting of peaks between successive detector frames as seen in Fig. 4.2.

4.3.1 Preprocessing

In contrast to the standard forward modeling method, we do not binarize the diffraction images but instead use a filter to remove the constant background and hot spot noise. To ensure the reconstruction quality, we make four assumptions:

- Most peaks do not overlap others. This is almost always satisfied if we use a small ω step size.
- We know the detector geometry to a very good accuracy. The accuracy should be $<5\,\mu$m based on the analysis in Section 4.5.1.
- We can reconstruct the grain shapes to a very good accuracy from the standard nf-HEDM reconstruction, which determines orientations based on binary detector images. More discussion is in Section 4.5.2.

- The peak intensity is much higher than the detector image noise. The effects of the image noise are discussed in Section 4.5.3.

The grain that we want to reconstruct is already voxelized from standard nf-HEDM, and it has, say, M voxels. Assuming the total number of peaks is K, then the intensity profile of every Bragg peak can be represented by

$$I_k(\mathbf{x}) = M_k Q_k(\mathbf{x}), \quad k = 1 \cdots K,$$

where $\mathbf{x}$ is the pixel coordinate on the detector, M_k is a normalization constant and $Q_k(\mathbf{x})$ can be regarded as the normalized intensity, which is a probability distribution with $\int Q_k(\mathbf{x}) d\mathbf{x} = 1$. This implies that all observed peaks contribute equally and only intensity variations within peaks contribute to the optimization; various factors (e.g., the structure, Debye-Waller, Lorentz, and form factors) vary from peak-to-peak but these play no role here.

The reconstruction process consists of two stages, in the first stage we get an approximate solution and then refine it in the second stage.

4.3.2 Reconstruction Stage One

In stage one, we reconstruct every voxel independently. At every voxel position, (x, y), and for a given distortion matrix $\mathbf{D}(x, y)$, we calculate the trajectories of the diffracted X-rays emanating from the position of the voxel at each Bragg sample orientation ω_B to find the detector pixel coordinates $\{\mathbf{x}^{(k)}\}_{k=1}^{K}$ that are struck using Eq. (4.4). We define the hit score as $\sum_{k=1}^{K} Q_k(\mathbf{x}^{(k)})$, and try to find the $\mathbf{D}(x, y)$ that can maximizes the hit score. This $\mathbf{D}(x, y)$ will be an approximate solution. We use the *Cross Entropy Method* [96] to find the maximum score; details are shown in Algorithm 2. The basic procedure for every voxel is that, start with generating N random trials of $\mathbf{D}(x, y)$ around the initial guess $\mathbf{I}$ using a multivariate Gaussian distribution with $\sigma^2\mathbf{I}$ as the covariance, then compute the score for each trial and pick the top n trials with the highest score, calculate the mean and covariance of these n trials and generate new N trials, repeat this circle until convergence (covariance is small enough) or finish after the maximum number of iterations ($MaxIter$). Empirically, we can choose $MaxIter = 100, N = 10^4, n = 100, \sigma^2 = 10^{-5}$ as the parameter values, where N, n are determined by the dimension and complexity of the optimization problem, σ controls the exploration range of the algorithm, which should be approximately the magnitude of the strain.

4.3.3 Reconstruction Stage Two

Using the approximate solution $\mathbf{D}(x, y)$ from stage one, we can simulate the peak intensity profiles by counting the pixel hits, $I_k^s(\mathbf{x})$, of diffracted X-rays from all voxels in

Algorithm 2: strain reconstruction stage 1

parameters: $MaxIter$, N, n, σ^2
input : $\mathcal{V} = \{(x, y)|\text{voxels of the grain}\}$, $\bar{\mathbf{O}}$
output : $\mathbf{D}(x, y)$

for $(x, y) \in \mathcal{V}$ **do**
  $mean \leftarrow \mathbf{I}$;
  $cov \leftarrow \sigma^2\mathbf{I}$;
  for $t \leftarrow 1$ **to** $MaxIter$ **do**
    $\{s_i\}_{i=1}^{N} \leftarrow$ `Gaussian`$(mean, cov)$;
    for $i \leftarrow 1$ **to** N **do**
      $h_i \leftarrow$`HitScore`$(x, y, s_i, \bar{\mathbf{O}})$;
    end for
    $\mathcal{J} = \{j|h_j$ is n highest hit score$\}$;
    $mean \leftarrow$ `Mean`$(s_{j\in\mathcal{J}})$;
    $cov \leftarrow$ `Covariance`$(s_{j\in\mathcal{J}})$;
  end for
  $\mathbf{D}(x, y) \leftarrow mean$;
end for

the grain, determined using Eq. (4.4). The peak intensity profiles can be represented as

$$I_k^s(\mathbf{x}) = M_s P_k(\mathbf{x}), \quad k = 1 \cdots K,$$

where $\mathbf{x}$ is the pixel coordinate, normalization constant M_s equals the number of voxels M, and $P_k(\mathbf{x})$ can be regarded as a probability distribution with $\int P_k(\mathbf{x}) d\mathbf{x} = 1$.

Algorithm 3: strain reconstruction stage 2

parameters: $InnerIter$, $OuterIter$, N, n,σ^2
input : $\mathcal{V} = \{(x, y)|\text{voxels of the grain}\}$, $\mathbf{D}(x, y)$, $\bar{\mathbf{O}}$
output : $\mathbf{D}(x, y)$

for $t \leftarrow 1$ **to** $OuterIter$ **do**
  for $(x, y) \in \mathcal{V}$ **do**
    $mean \leftarrow \mathbf{D}(x, y)$;
    $cov \leftarrow \sigma^2 \mathbf{I}$;
    for $tt \leftarrow 1$ **to** $InnerIter$ **do**
      $\{s_i\}_{i=1}^N \leftarrow$ `Gaussian(`$mean, cov$`)`;
      for $i \leftarrow 1$ **to** N **do**
        $c_i \leftarrow$ `GlobalCost(`$x, y, s_i, \bar{\mathbf{O}}$`)`;
      end for
      $\mathcal{J} = \{j|c_j$ is n lowest GlobalCost$\}$;
      $mean \leftarrow$ `Mean(`$s_{j\in\mathcal{J}}$`)`;
      $cov \leftarrow$ `Covariance(`$s_{j\in\mathcal{J}}$`)`;
    end for
    $\mathbf{D}(x, y) \leftarrow mean$;
  end for
end for

In stage two, we need to optimize all voxels together to minimize the difference between $I_k^s(\mathbf{x})$ and $I_k(\mathbf{x})$. A global cost function is needed so that we can quantify that difference. The global cost function we choose is

$$\begin{aligned}
&\sum_{k=1}^{K} \int I_k^s(\mathbf{x}^{(k)}) \ln \frac{I_k^s(\mathbf{x}^{(k)})}{I_k(\mathbf{x}^{(k)})} d\mathbf{x}^{(k)} \\
&= M_s \sum_{k=1}^{K} \int P_k(\mathbf{x}^{(k)}) \ln \frac{P_k(\mathbf{x}^{(k)})}{Q_k(\mathbf{x}^{(k)})} d\mathbf{x}^{(k)} + M_s \sum_{k=1}^{K} \ln \frac{M_s}{M_k},
\end{aligned}$$

which is directly related to the sum of the Kullback–Leibler divergence [97] between simulated intensity profile and the ground truth of each peak. It is easy to calculate the change of this global cost function if we change only one voxel's distortion matrix $\mathbf{D}(x, y)$. (see Section 4.3.4 for more details) So, a computationally efficient way to minimize the global cost function is to perform minimization at each

voxel while iterating through all voxels several times. The details are shown in Algorithm 3. Basically, we loop through all voxels $OuterIter$ times, each time for each voxel, we use the cross entropy method and iterate $InnerIter$ times to find a better $\mathbf{D}(x, y)$ to minimize the global cost function. Empirically, we can choose $InnerIter = 3, OuterIter = 10, N = 10^4, n = 50, \sigma^2 = 10^{-6}$ as the parameter values. Comparing to stage one, slightly smaller σ value is chosen because the initial guesses are already close to the true values, good results can be obtained after a few iterations.

4.3.4 GPU Implementation

Both stage one and stage two reconstructions require large amount of computing power, but fortunately both algorithms can easily be implemented in parallel to exploit the power of Graphics Processing Unit (GPU). In our current implementation, the work of inner-most for loops in Algorithm 2 (line $6 \sim 8$) and Algorithm 3 (line $7 \sim 9$) are distributed to all threads. That is to say, for Algorithm 2, each thread computes the function **HitScore** with different s_i values at the same time; and for Algorithm 3, each thread computes the function **GlobalCost** with different s_i values at the same time.

First difficulty we encountered was the limit of GPU memory. Since extremely small rotation steps ($\delta\omega = 0.05^\circ$) are used, it is not easy to save all diffraction images ($2048 \times 2048 \times 3600 \approx 2 \times 10^{10}$ pixels) into the GPU memory. Given that the reconstruction is performed on each grain individually, we can extract windows around every peak from the grain of interest, and only save the pixel values within those windows and the positions of those windows to the GPU memory. Currently, we use $\Delta J = 300$ pixels, $\Delta K = 160$ pixels, $\Delta\Omega = 45$ frames as the window size, and there are ≈ 100 peaks for each grain, so in total we need to save about $300 \times 160 \times 45 \times 100 \approx 2 \times 10^8$ pixels, which dramatically reduces the memory requirement. Current choice of window size is ad-hoc, which should depend on the grain size and the degree of deformation.

The computation of **HitScore** is straightforward, just using Eq. (4.4) to calculate the pixel coordinates that are struck in simulation and then calculating the hit score as its definition. However, the computation of **GlobalCost** is a bit tricky. Naively calculating as the definition is extremely expensive, because the forward simulation of the whole grain is needed every time we calculate the global cost. Fortunately, in Algorithm 3 we only update the $\mathbf{D}(x, y)$ for one voxel at a time, and the value changing on global cost function is easy to calculate if only one voxel changes its $\mathbf{D}(x, y)$. Specifically, assume that $I^s_{k,b}(\mathbf{x})$ and $I^s_{k,a}(\mathbf{x})$ are two simulated peak intensity profiles from before changing the voxel strain value and after changing the voxel strain value respectively. Then the differences between $I^s_{k,b}(\mathbf{x})$ and $I^s_{k,a}(\mathbf{x})$ are only on two pixels, the one was hit before the change and the one is hit after the change, and we name them $\mathbf{b}^{(k)}$ and $\mathbf{a}^{(k)}$ respectively. If these two pixel coordinates are the same,

then there is no difference between $I^s_{k,b}(\mathbf{x})$ and $I^s_{k,a}(\mathbf{x})$; if they are different, then the differences will be:

$$\begin{aligned} I^s_{k,a}(\mathbf{b}^{(k)}) &= I^s_{k,b}(\mathbf{b}^{(k)}) - 1 \\ I^s_{k,a}(\mathbf{a}^{(k)}) &= I^s_{k,b}(\mathbf{a}^{(k)}) + 1 \end{aligned} \tag{4.5}$$

As a result, difference between the global cost before and after changing one voxel will be:

$$\begin{aligned} &\text{GlobalCost}_a - \text{GlobalCost}_b \\ &= \sum_{k=1}^{K} \left(I^s_{k,a}(\mathbf{a}^{(k)}) \ln \frac{I^s_{k,a}(\mathbf{a}^{(k)})}{I_k(\mathbf{a}^{(k)})} + I^s_{k,a}(\mathbf{b}^{(k)}) \ln \frac{I^s_{k,a}(\mathbf{b}^{(k)})}{I_k(\mathbf{b}^{(k)})} \right) - \\ &\quad \sum_{k=1}^{K} \left(I^s_{k,b}(\mathbf{a}^{(k)}) \ln \frac{I^s_{k,b}(\mathbf{a}^{(k)})}{I_k(\mathbf{a}^{(k)})} + I^s_{k,b}(\mathbf{b}^{(k)}) \ln \frac{I^s_{k,b}(\mathbf{b}^{(k)})}{I_k(\mathbf{b}^{(k)})} \right) \\ &= \sum_{k=1}^{K} \left((I^s_{k,b}(\mathbf{a}^{(k)}) + 1) \ln \frac{(I^s_{k,b}(\mathbf{a}^{(k)}) + 1)}{I_k(\mathbf{a}^{(k)})} + (I^s_{k,b}(\mathbf{b}^{(k)}) - 1) \ln \frac{(I^s_{k,b}(\mathbf{b}^{(k)}) - 1)}{I_k(\mathbf{b}^{(k)})} \right) - \\ &\quad \sum_{k=1}^{K} \left(I^s_{k,b}(\mathbf{a}^{(k)}) \ln \frac{I^s_{k,b}(\mathbf{a}^{(k)})}{I_k(\mathbf{a}^{(k)})} + I^s_{k,b}(\mathbf{b}^{(k)}) \ln \frac{I^s_{k,b}(\mathbf{b}^{(k)})}{I_k(\mathbf{b}^{(k)})} \right). \end{aligned} \tag{4.6}$$

Therefore, if the simulated peak intensities are saved and updated on each iteration based on Eq. (4.5), the global cost can be efficiently calculated from Eq. (4.6).

4.4 Results on Synthetic Data

A 3D synthetic Ti7Al microstructure was generated using *Dream3D* [1] with spatially resolved strain simulated using an open source code called Micromechanical Analysis of Stress-Strain Inhomogeneities using FFTs (MASSIF) [98, 99]. MASSIF uses spectral method, in that it solves the stress equilibrium equations in Fourier space by taking the Discrete Fourier Transform (DFT) of the material grid using the (Fast Fourier Transform) FFT algorithm. The stiffness parameters used were

$$\begin{bmatrix} 162400 & 92000 & 69000 & 0.0 & 0.0 & 0.0 \\ 92000 & 162400 & 69000 & 0.0 & 0.0 & 0.0 \\ 69000 & 69000 & 180700 & 0.0 & 0.0 & 0.0 \\ 0.0 & 0.0 & 0.0 & 46700 & 0.0 & 0.0 \\ 0.0 & 0.0 & 0.0 & 0.0 & 46700 & 0.0 \\ 0.0 & 0.0 & 0.0 & 0.0 & 0.0 & 35200 \end{bmatrix},$$

[1] http://dream3d.bluequartz.net/

and the plastic parameters (using a modified-Voce hardening law [99]) were set high enough that no plasticity occurred in the simulations. Uniaxial tension was applied with a macroscopic strain of 1×10^{-2}, and the result of the MASSIF code is the strain and orientation field on a $128 \times 256 \times 256$ grid (with grid size of $2\,\mu m \times 2\,\mu m$). [2]

The input to the reconstruction code is a set of diffraction pattern images based on one slice of the virtual Ti7Al sample; images are simulated using the forward modeling software and the patterns are convolved with a Gaussian filter to mimic the total effects of the point spread function of the detector and scintillator, and the X-ray energy spread. The "virtual detector" is set at 7.145 mm away from the rotation axis, with 2048×2048 pixels with the size of $1.454\,\mu m$; these numbers characterize the current near-field detector used at the 1-ID beamline at the Advanced Photon Source. The virtual experiment operates with 52 keV X-rays and the rotation range is $\Delta\omega = 180°$ with images integrated over $\delta\omega = 0.05°$. Using the ground truth grain averaged orientations as the $\bar{\mathbf{O}}$'s, we recovered the distortion matrix $\mathbf{D}$ on a 256×256 grid with the resolution of $2\,\mu m \times 2\,\mu m$. The reconstruction took about 6 hours on a single GPU (GeForce GTX 1080). Fig. 4.3 shows the reconstructed cross section colored by the z direction (loading direction) strain tensor component values. The heterogeneous reconstructed strain component field (right) is in good agreement with the ground truth (left).

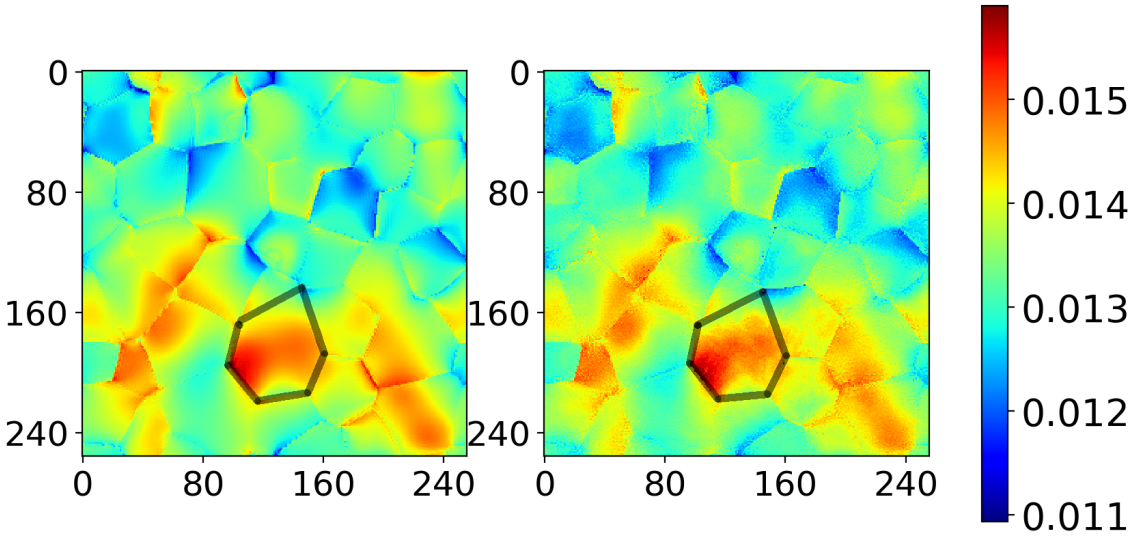

Figure 4.3: Left: the ground truth of S_{zz} strain component. Right: reconstructed result. The grain in black boundaries will be studied in detail.

Figure 4.4 shows the reconstruction error distribution, a histogram of point-by-point differences between the reconstruction and the input ground truth, for each strain component. Note again that the macroscopic applied strain was 10^{-2} in the

[2]The MASSIF simulation was performed by Christopher Kantzos

z-direction. Clearly, the strain reconstruction captures the heterogeneous strain variations that are seen in Fig. 4.3. One observation is that, in general, strain in the loading direction S_{zz} and shear strains have better relative accuracy than S_{xx} and S_{yy}. This is because the diffraction direction is more sensitive to S_{zz} and shear strains under this experiment setup. The small difference between S_{xx} and S_{yy} may due to statistic error introduced by the small amount of grains.

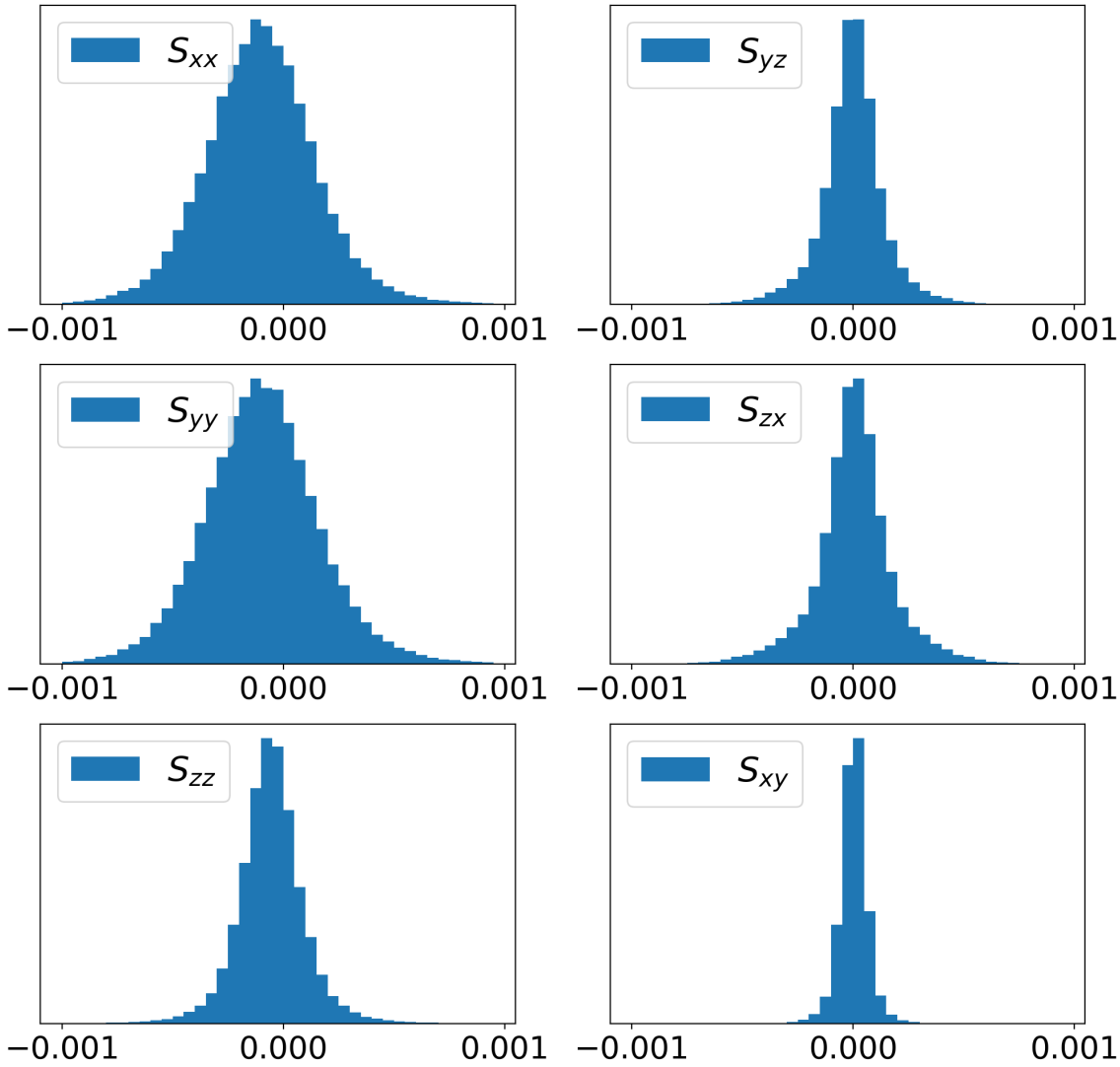

Figure 4.4: The reconstruction error for each strain component over the whole sample.

To discuss the reconstruction result in more detail, we focus on the big grain in the center, which is marked by black boundaries in Fig. 4.3. The reconstruction result for every component of strain $\mathbf{S}$ and the ground truth are shown in Fig. 4.5. $\mathbf{S}_{zz}$ is in the direction of both the applied strain and the rotation axis. We find that $\mathbf{S}_{xx}$

and $\mathbf{S}_{yy}$ have worse reconstruction accuracy compared to $\mathbf{S}_{zz}$ and the off-diagonal components, which is consistent with Fig. 4.4.

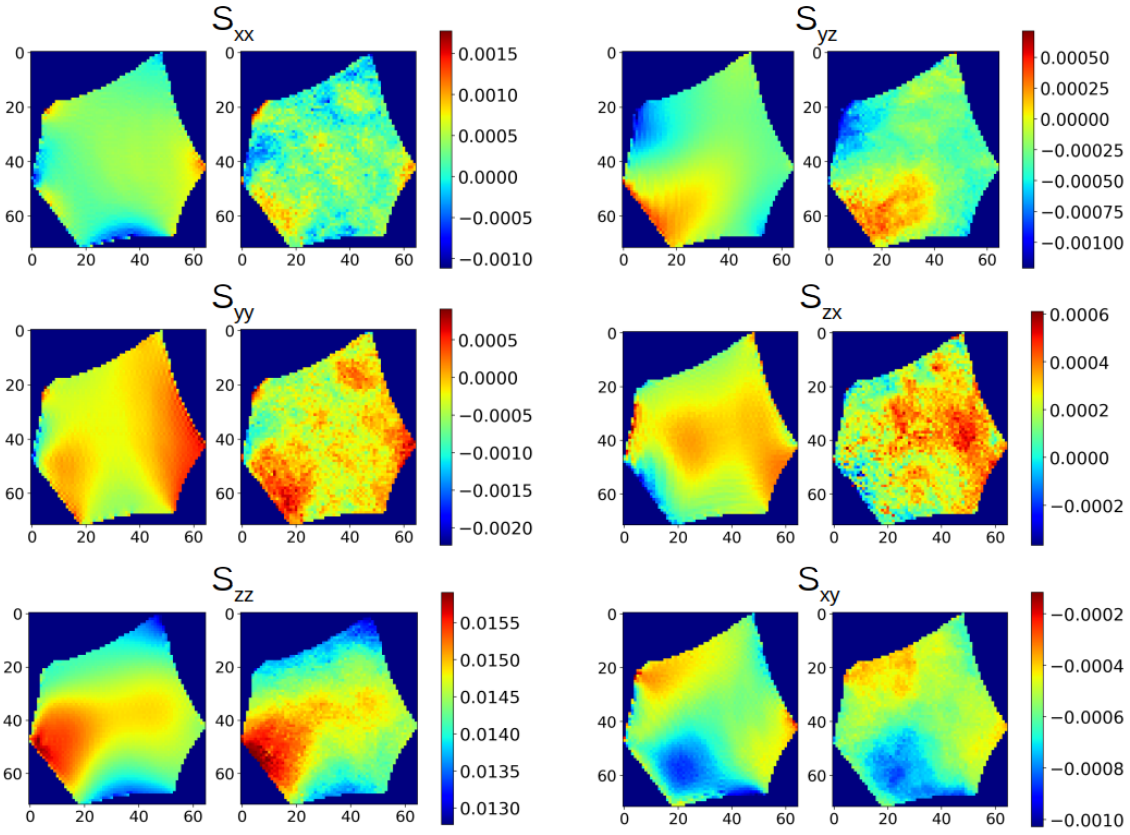

Figure 4.5: Maps of each strain tensor component over a single grain. In each pair of maps, the ground truth is on the left and reconstruction results are on the right. Axis scales are in millimeters.

The reconstruction also yields corrected Euler angles (in ZXZ convention) for each voxel. These are shown in the histograms of Fig. 4.6. It is evident that the error on each Euler angle is $\sim 0.02^{\circ}$.

An example of a simulated peak at no strain and at finite macroscopic elastic strain are shown in Fig. 4.7, along with the peak that was used as the input for the reconstruction. As we can see, the simulated peak from reconstructed strain recovers the peak separation phenomenon in the input images.

We can also look at the simulated peaks from the reconstruction stage one and stage two. Figure 4.8 shows the middle frame of Figure 4.7, the left figure is the "ground truth" pattern which is the input for our reconstruction algorithms, the middle plot in Fig. 4.8 is the simulation result after the reconstruction stage one, the right plot is the result after the stage two. As we expected, reconstruction stage one

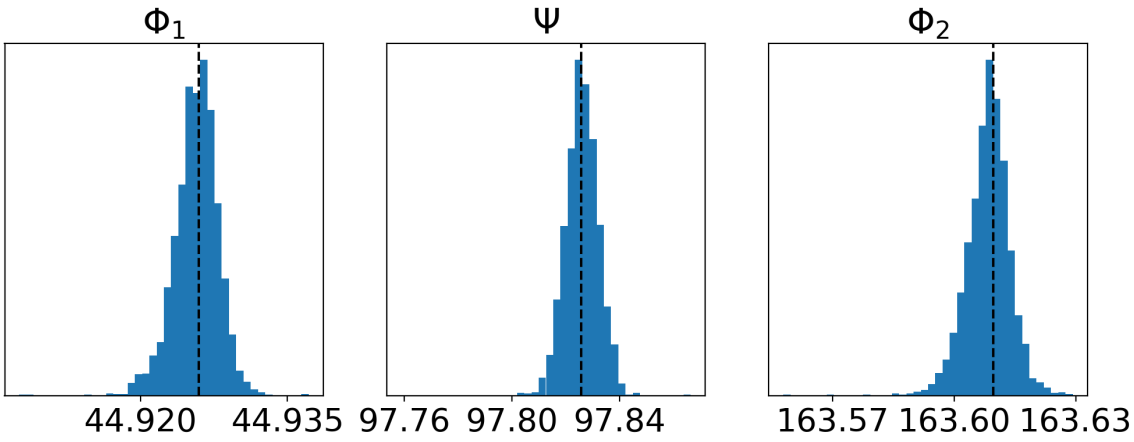

Figure 4.6: Histogram of Euler angles of each voxel within one grain. Dashed lines are the values of the ground truth.

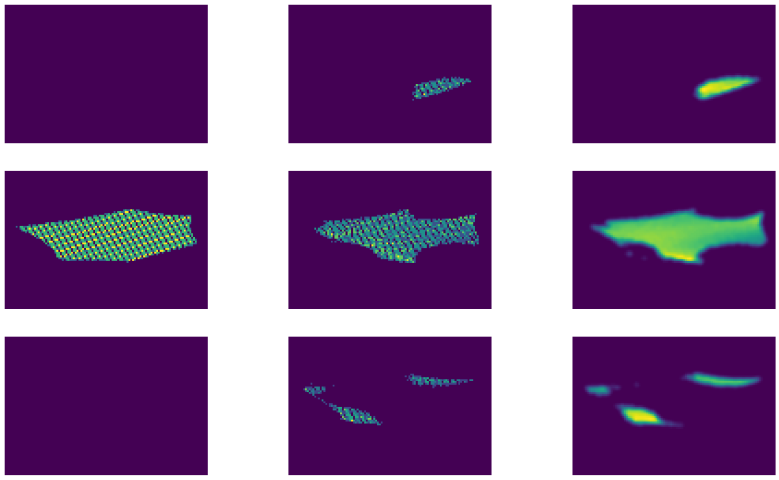

Figure 4.7: Left: the simulated peak without intragranular strain variation, every voxel has the same grain averaged strain. Middle: simulated peak with reconstructed strain. Right: peak used as the input for reconstruction algorithm. The three rows represent three successive ω frames. The stripes in the simulated Bragg peaks result from the mesh size $2\,\mu m \times 2\,\mu m$, which is slightly larger than the pixel size.

correctly reproduced the peak splitting phenomenon, but it is biased to high intensity region so it has higher maximum pixel intensity than others. As for the result after stage two, the reproduced peak has a closer intensity distribution to the ground truth.

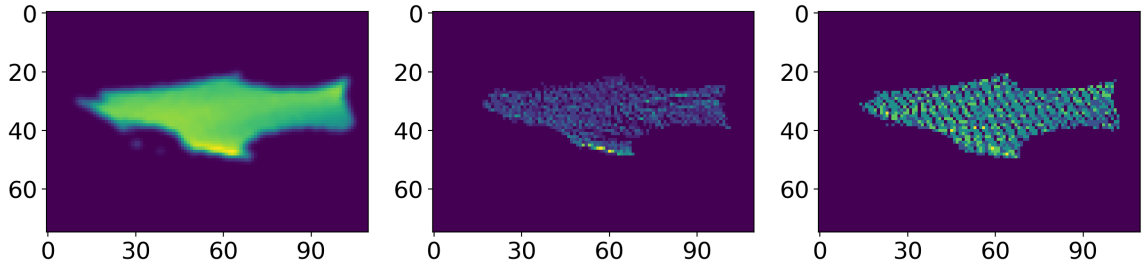

Figure 4.8: Left: one example of the peaks used as the input for reconstruction algorithm. (the middle right image in Fig. 4.7.) Center: the peak intensity simulated from stage one result. Right: the peak intensity simulated from stage two result.

4.5 Sensitivity Analysis

It is important to know how the reconstruction results are influenced by noise and uncertainties in real experimental data. The following results show that the proposed reconstruction method is robust against small purturbations.

4.5.1 Geometry Uncertainty

For this experiment setup, there are three important geometry parameters, the distance between detector and the sample rotation axis (L), the relative horizontal position of sample rotation axis on the detector (J), and the relative vertical position of X-ray beam plane on the detector (K). In addition to the reconstruction in Section 4.4 (with no error on these three parameters), we also did three reconstructions with the following geometry errors:

- $\Delta J = 3$ pixels, $\Delta K = \Delta L = 0$
- $\Delta K = 1$ pixel, $\Delta J = \Delta L = 0$
- $\Delta L = 5\,\mu\text{m}$, $\Delta J = \Delta K = 0$

The S_{zz}, S_{yy}, S_{xy} component of reconstruction results are shown in Fig. 4.9. As we can see, the geometry uncertainty introduces systematic errors but the strain pattern and scale are maintained. However, the reconstruction of S_{yy} (and S_{xx}, which exhibited similar behavior) is obviously more sensitive to geometry errors than S_{zz}, S_{xy}. Together with Fig. 4.4 and Fig. 4.5, we find that nf-HEDM is better at measuring S_{zz} and the shear strains than S_{xx} and S_{yy}.

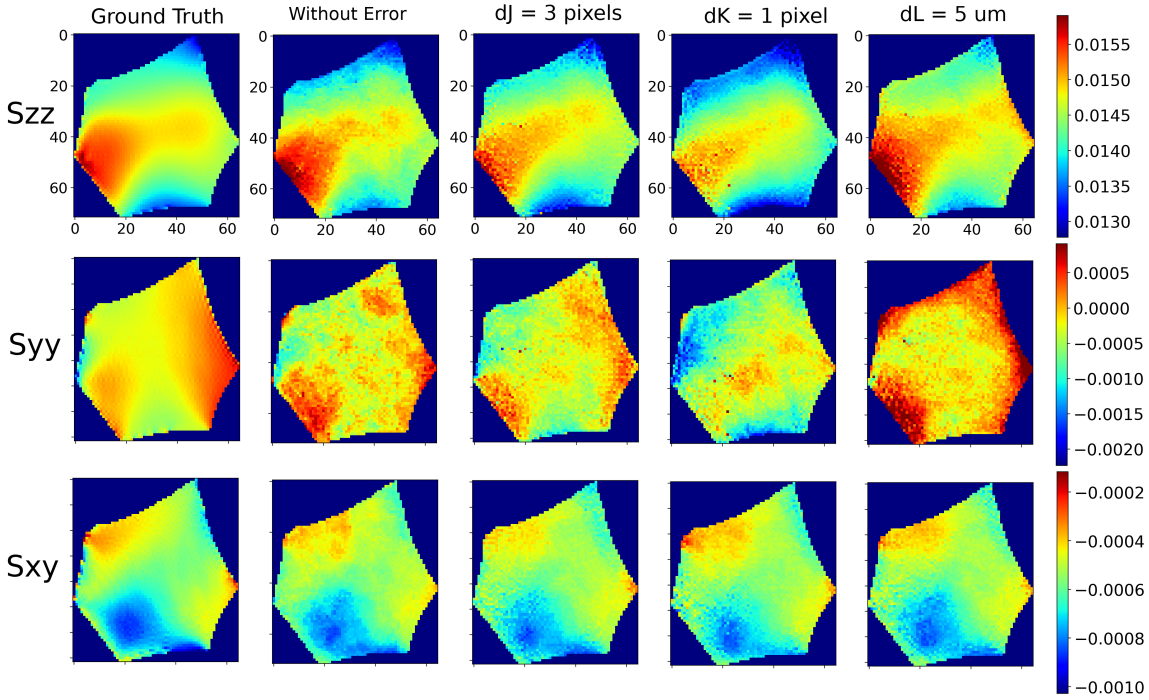

Figure 4.9: The ground truth of S_{zz}, S_{yy}, S_{xy} strain components and the reconstruction results with different geometry errors.

4.5.2 Grain Shape Uncertainty

Another uncertainty is inherited from the standard nf-HEDM reconstruction. There may be some error in the grain boundary positions. We investigated this problem by reconstructing the strain with an "eroded" region of the original grain. By "erode", we mean removing all voxels that are within a certain distance from the grain boundary. The reconstruction results are shown in Fig. 4.10. Again, the reconstruction using an eroded region preserves the strain pattern while introducing deviations from the ground truth. This is important since the uncertainty in grain boundary positions are intrinsic to the experimental data.

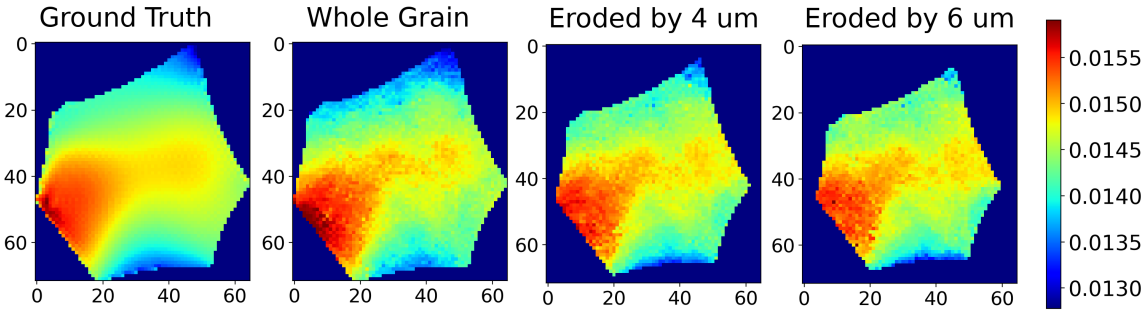

Figure 4.10: Effects of grain boundary positions.

4.5.3 Image Noise

Detector images contain Poisson noise due to finite counting statistics. Since accurately modeling the image noise is beyond the scope of this work, here we applied Poisson noise and "salt and pepper" noise to the images. Mathematically, the noisy pixel intensity is modeled as:

$$I_{noisy} = P(\lambda_1 I_0)/\lambda_1 + B_\rho \lambda_2 P(1),$$

where $P(\cdot)$ is the Poisson distribution, I_0 is the pixel intensity of noiseless image, λ_1 controls the Poisson noise on the signal, B_ρ is a random variable that is 1 with probability $\rho \in [0, 1]$ and otherwise is 0, and λ_2 represents the strength of "salt and pepper" noise.

We tested our reconstruction method under two noise levels:

- Noise level A: $\lambda_1 = 0.5, \lambda_2 = 8, \rho = 0.7$
- Noise level B: $\lambda_1 = 0.1, \lambda_2 = 40, \rho = 0.7$

The level of noise can be demonstrated by the images. An example of the noise effects on the diffraction patterns is shown in Fig. 4.11. The corresponding reconstruction

results are shown in Fig. 4.12. Again, the overall reconstruction results are qualitatively independent of added noise but directly reflect the noise due to the intensity matched nature of the algorithm.

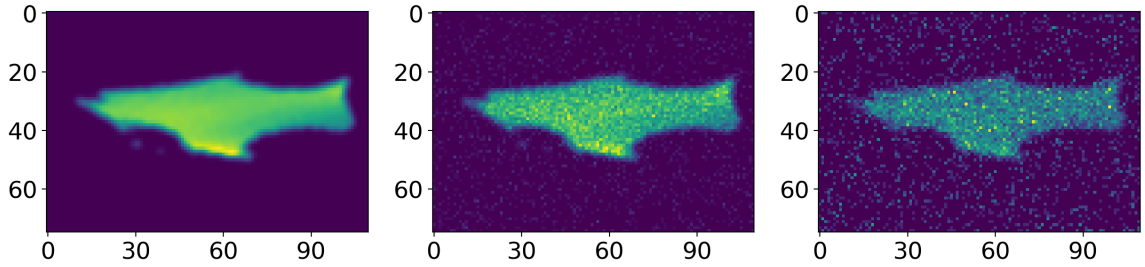

Figure 4.11: Left: noiseless pattern. Center: pattern with noise level A. Right: pattern with noise level B.

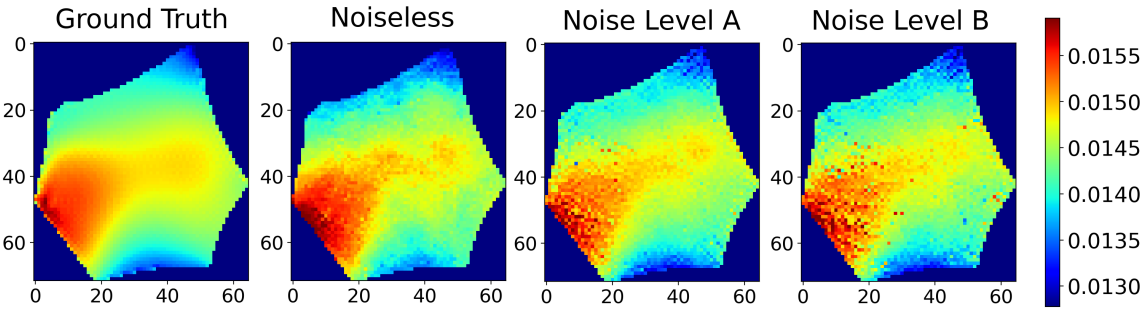

Figure 4.12: The ground truth of S_{zz} strain component and the reconstruction result with different noise levels.

4.6 Application to a Ti7Al Sample

4.6.1 Experiment Overview

A dedicated nf-HEDM measurement for the strain reconstruction was performed at the Advanced Photon Source sector 1 in Argonne National Laboratory.[3] A high-resolution-monochromator (HRM) was used to get a narrower energy profile, $dE/E \approx 10^{-4}$, of the incoming X-ray beam so that the strain signal won't be overwhelmed by

[3]Data collection was performed in July 2013 by J. Lind, K. Chatterjee, R.M. Suter, and A. Beaudoin with assistance from APS Sector 1 staff including S. Shastri who ran the HRM. A detailed description of experiment procedure is given in [100]. While a variety of preliminary analysis based on far-field HEDM and conventional orientation reconstructions have been performed, this is the first quantitative test of local strain extraction.

the energy noise. The sample was a Ti7Al cylinder with diameter of about 0.8 mm, and the diffraction images were collected with integration interval of 0.05°.

In the initial state, there is no load on the sample, then it was pulled with a load gradually increased to 18.3 pounds. During the loading, the sample was slightly bent; in response to tensile loading, the sample straightened causing compression on one side and tension on the other. The bending is unintentional but beneficial because it increases the intragranular strain heterogeneity and it gives us a clear qualitative trend to verify with the strain reconstruction result.

The standard nf-HEDM reconstruction results of the initial state (before loading) and the state under 18.3 pounds load are shown in the confidence maps of Fig. 4.13. The color shows the confidence of the standard reconstruction. The cross section of the loaded state appears shifted because the sample was bent. Note the reduction in the confidence values in the loaded state. As shown below in Fig. 4.14, the right side of the sample underwent tensile strain while the left side was under compression whereas the reconstruction used the same lattice constants as used for the unloaded state. The reduced confidence values in both regions indicate near-field strain sensitivity. The current analysis focuses on the numbered grains which are in the region where the stain appears least and the orientation reconstruction is most reliable; it attempts to extract strain variations within these individual grains. In the grains on the tensile (right) side, we might expect larger average strains to reflect those in far-field HEDM analysis; these would probably have scaled larger variations too. In Section 4.6.2 we will use the small grain circled by red line in the loaded state image to calibrate the geometry parameters of the experiment setup. Then we will reconstruct the intragranular strain of the numbered grains in Section 4.6.3.

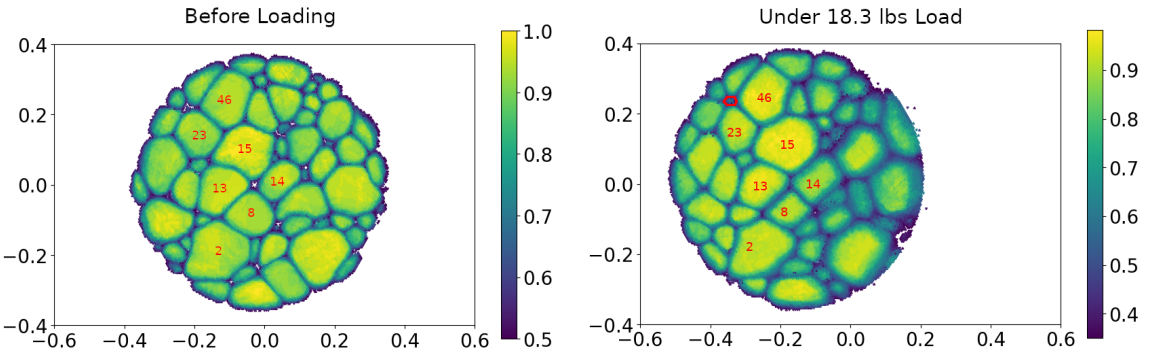

Figure 4.13: The standard nf-HEDM reconstruction results of the state before the loading and under 18.3 lbs load. The color shows the confidence of the standard reconstruction performed by J. Lind using IceNine software. [4]. The intragranular strain reconstruction in Section 4.6.3 are performed on the grains with IDs, the grain circled by red line is used for calibration in Section 4.6.2.

We also have the grain averaged strain values reconstructed from far-field HEDM

(ff-HEDM) [93], as shown in Fig. 4.14. This figure is slightly shifted and rotated comparing to Fig. 4.13, but the overall trend of the grain averaged strains is consistent with the bending direction evident here.

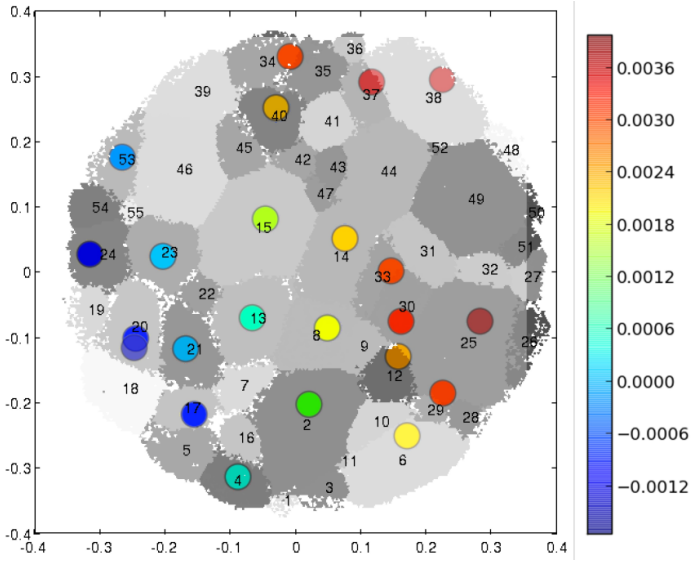

Figure 4.14: S_{zz} values of the grain averaged strain reconstructed from ff-HEDM superposed on the nf-HEDM grain map for the loaded state. Note the clear gradient moving from left (compressive) to right (tensile). Thanks to K. Chatterjee and A. Beaudoin for this analysis and figure.

4.6.2 Geometry Parameters Calibration

As we mentioned in Section 4.5.1, it is crucial to have the value of experimental geometry parameters within small uncertainty. The geometry parameters include: the distance between detector and the sample rotation axis (L), the relative horizontal position of sample rotation axis on the detector (J), the relative vertical position of X-ray beam plane on the detector (K), and the orientation of the detector (ϕ_1, ψ, ϕ_2) which expressed as Euler angles in ZXZ convention. Unfortunately, current nf-HEDM instruments can't give us those numbers, so some calibration process is needed.

The "rigorous" way of calibration is to reconstruct those unknown parameters along with the whole deformation gradient field, however it is computationally unrealistic. Instead, we pick a small grain (red circled in Fig. 4.13), treat it as a point scattering source and reconstruct its deformation gradient and the center of mass (x, y) along with those 6 unknown parameters. So, in total we have $6 + 9 + 2 = 17$ unknowns, while we have $\sim 10^2$ diffraction peaks for that grain, which means the calibration is an over-determined problem.

For the loaded state, we have the initial guess that results from the standard nf-HEDM calibration and reconstruction:

$$\begin{aligned} J^0 &= 1182.19, & K^0 &= 2026.27, & L^0 &= 7.145, \\ \phi_1^0 &= 89.1588, & \psi^0 &= 87.5647, & \phi_2^0 &= 0.2786, \\ x^0 &= -0.3459, & y^0 &= 0.2387, & \mathbf{D}^0 &= \mathbf{I} \end{aligned}$$

where J, K are in the unit of number of pixels, L, x, y are in the unit of millimeter, ϕ_1, ψ, ϕ_2 are in the unit of degree. (x^0, y^0) are the center of mass of that grain. The reconstructed Euler angles of that grain is $(147.248, 81.8513, 217.515)$. We choose 76 of its diffraction peaks, obtain the position (pixel coordinates and ω values) of their center. The calibration is just to find the values of the parameters so that the simulated peak positions (using Eq. (4.4)) are as close as possible to the real peaks. The cost function we used is the weighted sum of squares, the weights are inverse of the approximated uncertainties when we measure the position of real diffraction peaks (we choose 0.05° for Ω, 5 pixels for J, 1 pixel for K). The minimization algorithm we used is Broyden–Fletcher–Goldfarb–Shanno algorithm (BFGS) [101]. After calibration, the parameters for the loaded state we get are:

$$\begin{aligned} J &= 1180.24, & K &= 2022.76, & L &= 7.056, \\ \phi_1 &= 89.6934, & \psi &= 90.0441, & \phi_2 &= 0.1904 \end{aligned}$$

Fig. 4.15 shows the position difference between the 76 simulated peaks and corresponding experimental peaks before and after calibration. It is clear that after calibration, the difference between simulated peak positions and real experimental peak positions are very small, within the uncertainties of real experimental peak position estimations.

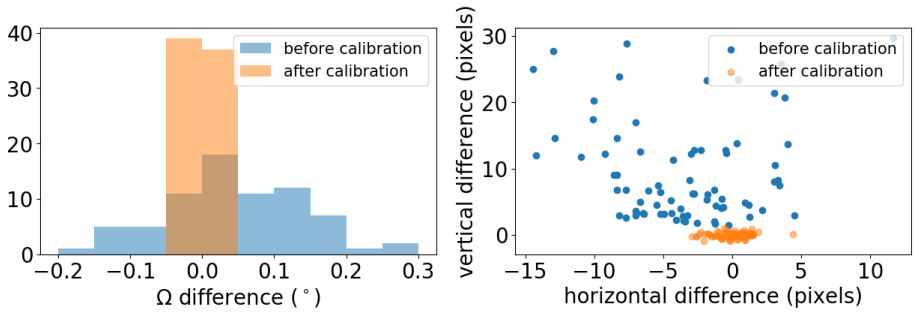

Figure 4.15: The position difference between the 76 simulated peaks and corresponding experimental peaks. The simulations from parameters before calibration are shown in blue, after calibration are shown in orange. On the left is the histogram of Ω differences with binning size of 0.05°. On the right is the differences of pixel position in the unit of number of pixels.

The same calibration procedure was also performed on the initial state with the same grain, and the parameters we get are very similar with the loaded state ($\Delta J < 2$ pixels, $\Delta K < 1$ pixel, $\Delta L < 5\,\mu$m). For the reconstruction of both states in Section 4.6.3, we used the parameters calibrated from the loaded state.

4.6.3 Reconstruction Results

We reconstructed grains $2, 8, 13, 14, 15, 23, 46$ in Fig. 4.13 for both states, all of them are on a grid with size of $2\,\mu\text{m} \times 2\,\mu\text{m}$, the results are shown in Fig. 4.16. The reference lattice constants we used for calculating the strains are:

$$a = b = 2.9254\,\text{Å}, \qquad c = 4.674\,\text{Å},$$

which is used in [93] and the standard nf-HEDM reconstructions.

As we can see, in the initial state the intragranular S_{zz} values for every grain are relatively small, most of them are within $\pm 1 \times 10^{-3}$ range. As we pulled the sample, strain was building up. For these seven grains, the intragranular strains ranging from -1×10^{-3} to 3×10^{-3}, and the overall trend is consistent with the bending direction and the approximated grain averaged values also match with the ff-HEDM results in Fig. 4.14. One caveat is that, the reconstructed strain near the grain boundaries

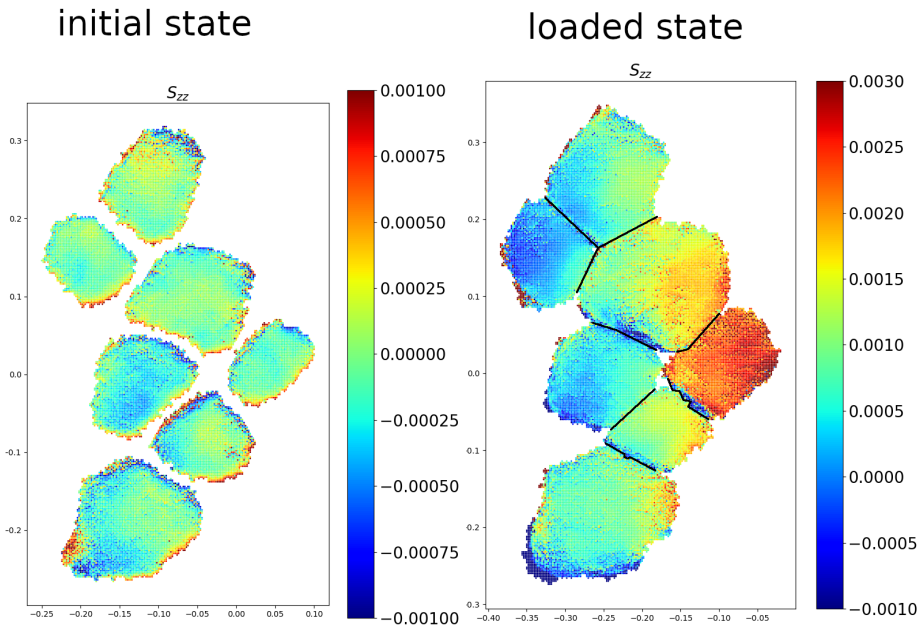

Figure 4.16: The reconstructed intragranular S_{zz} strain component for grain with IDs in Fig. 4.13. In the loaded state, black lines indicate the grain boundaries from the standard nf-HEDM reconstruction.

(indicated by black lines in Fig. 4.16) are not necessary accurate, since they are more

sensitive to the errors in the experiment geometry parameters. Therefore, we did not reconstruct the voxels near boundaries in the initial state. Moreover, the boundary position may not be accurate either. Although the grain boundary position accuracy of standard nf-HEDM reconstruction in undeformed sample is $\sim 1\,\mu m$ [39], we don't know its accuracy for deformed sample yet. Further analysis is needed to get more accurate values at boundaries, e.g. by fine tuning the geometry parameters and boundary positions to get better fit between simulated peak and real peak.

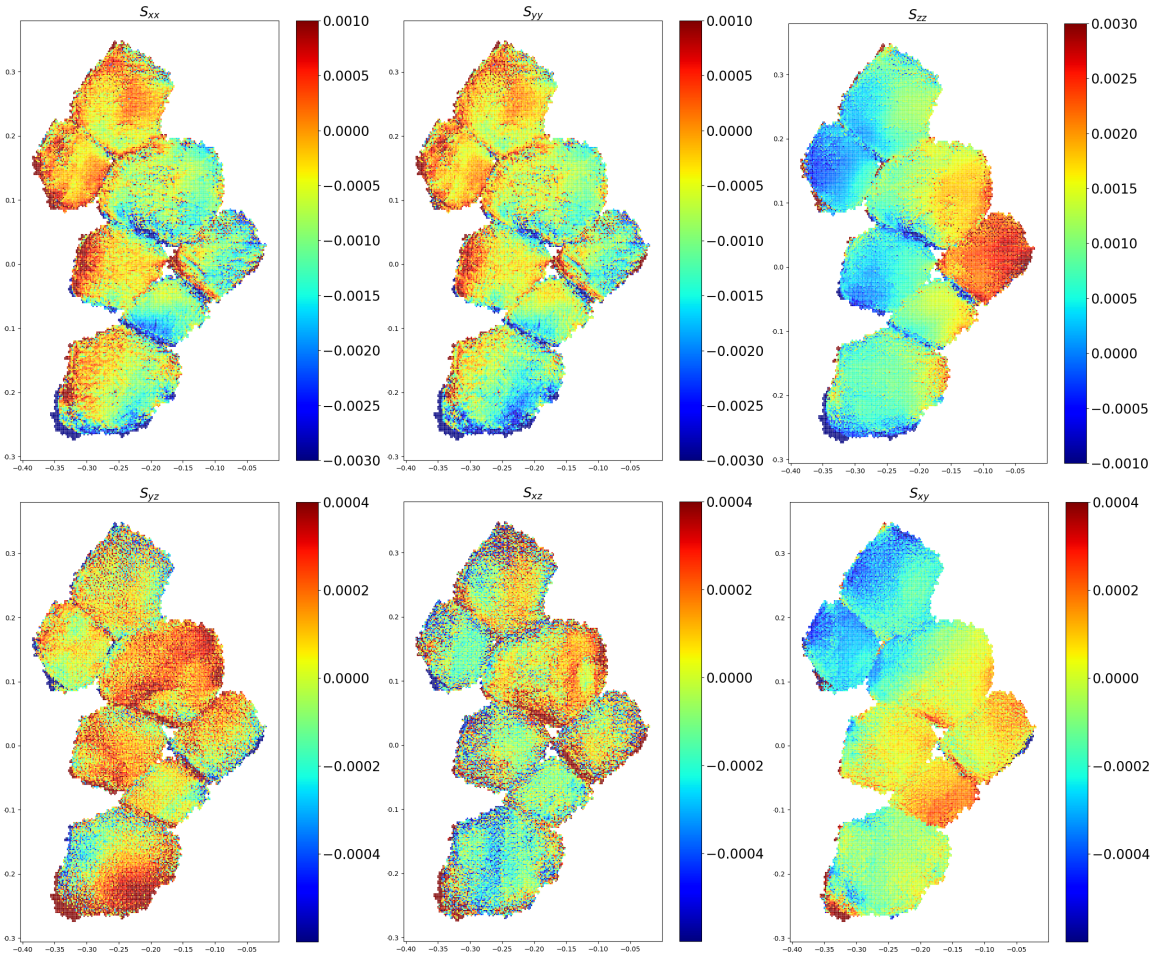

Figure 4.17: The reconstructed results for all strain components in loaded state.

The reconstructed result of all strain components for loaded state is shown in Fig. 4.17. As we expected, the patterns of components S_{zz} and S_{xy} are cleaner than other components, and all of them have reasonable magnitudes. Using the same stiffness matrix we used in Section 4.4, we can calculate the stress tensor from the strain values. The results are shown in Fig. 4.18. All diagonal stress components are noisy because of the relatively low quality of the reconstruction of S_{xx} and S_{yy}. Improving the reconstruction quality and analyzing the reconstruction results are

needed in future work.

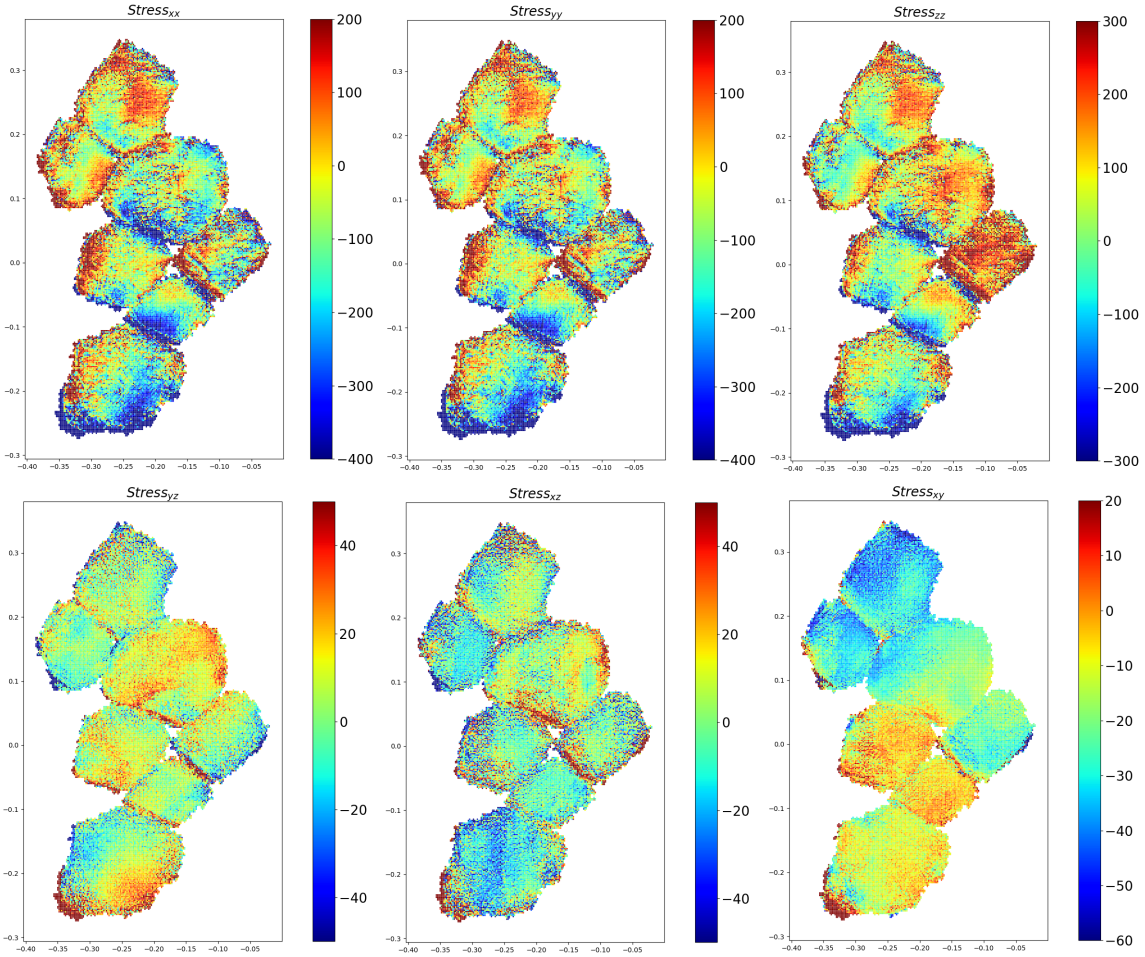

Figure 4.18: The values of stress components in loaded state calculated from the strain values and the stiffness matrix in Section 4.4.

4.6.4 Diffraction Patterns Comparison

One straightforward way to check the validity of reconstructions is to compare the X-ray diffraction patterns. Because there are about one hundred peaks from each grain collected by the nf-HEDM measurement, it is tedious and not necessary to demonstrate all of them in this thesis. In this section, we will show several diffraction patterns and corresponding simulated patterns from Grain 15 for both initial and loaded states. The same Bragg peaks in initial and loaded states are found by their Miller indices (h, k, l).

One observation is that all simulated peaks match very well with corresponding real diffraction peaks. We noticed that most of the diffraction peaks are similar to

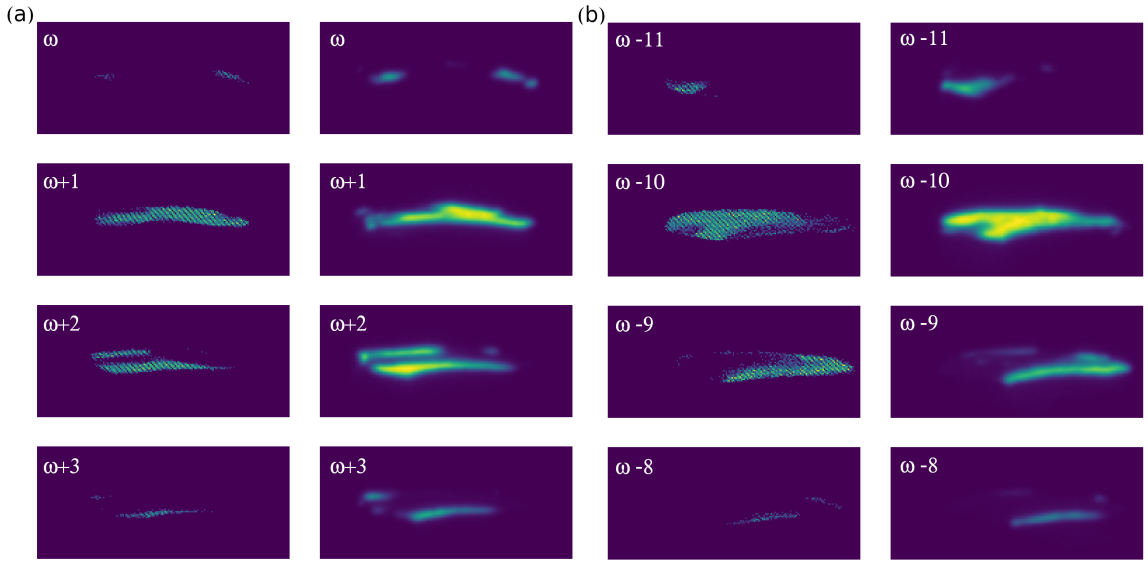

Figure 4.19: Diffraction Peak A, Miller indices $(h, k, l) = (1, 1, 2)$. (a) Initial state, left column is simulated from the reconstructed strain field, right column is the real diffraction pattern, different rows are successive rotation frames; (b) Loaded state, left column is simulated from the reconstructed strain field, right column is the real diffraction pattern, different rows are successive rotation frames. Left and right rows of (a) and (b) do not represent the same rotation frames, there is a shift which reflects an average strain change. The ω values in the images indicate the relative differences of rotation frame indices.

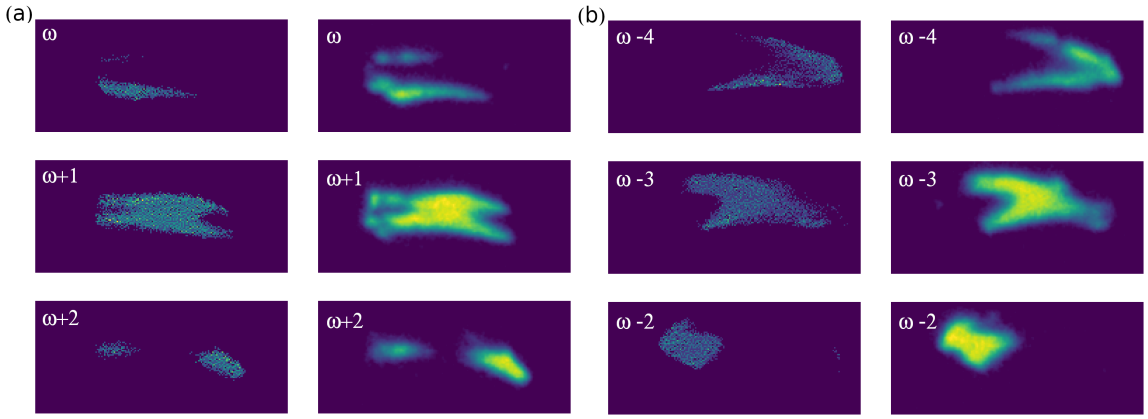

Figure 4.20: Diffraction Peak B, Miller indices $(h, k, l) = (3, 1, 1)$. (a) Initial state, left column is simulated from the reconstructed strain field, right column is the real diffraction pattern, different rows are successive rotation frames; (b) Loaded state, left column is simulated from the reconstructed strain field, right column is the real diffraction pattern, different rows are successive rotation frames. Left and right rows of (a) and (b) do not represent the same rotation frames, there is a shift which reflects an average strain change. The ω values in the images indicate the relative differences of rotation frame indices.

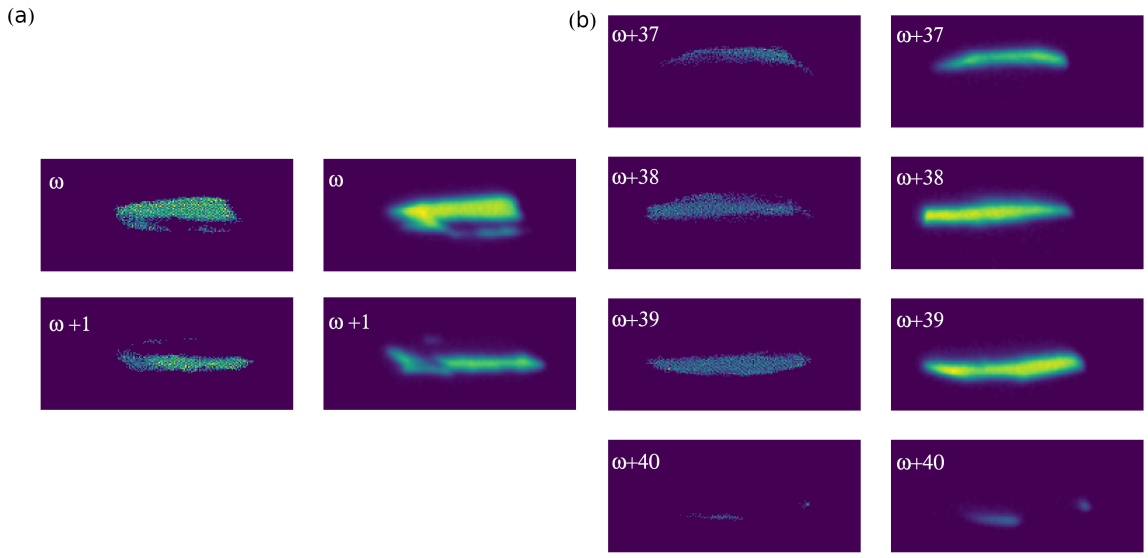

Figure 4.21: Diffraction Peak C, Miller indices $(h, k, l) = (1, 2, 1)$. (a) Initial state, left column is simulated from the reconstructed strain field, right column is the real diffraction pattern, different rows are successive rotation frames; (b) Loaded state, left column is simulated from the reconstructed strain field, right column is the real diffraction pattern, different rows are successive rotation frames. Left and right rows of (a) and (b) do not represent the same rotation frames, there is a shift which reflects an average strain change. The ω values in the images indicate the relative differences of rotation frame indices.

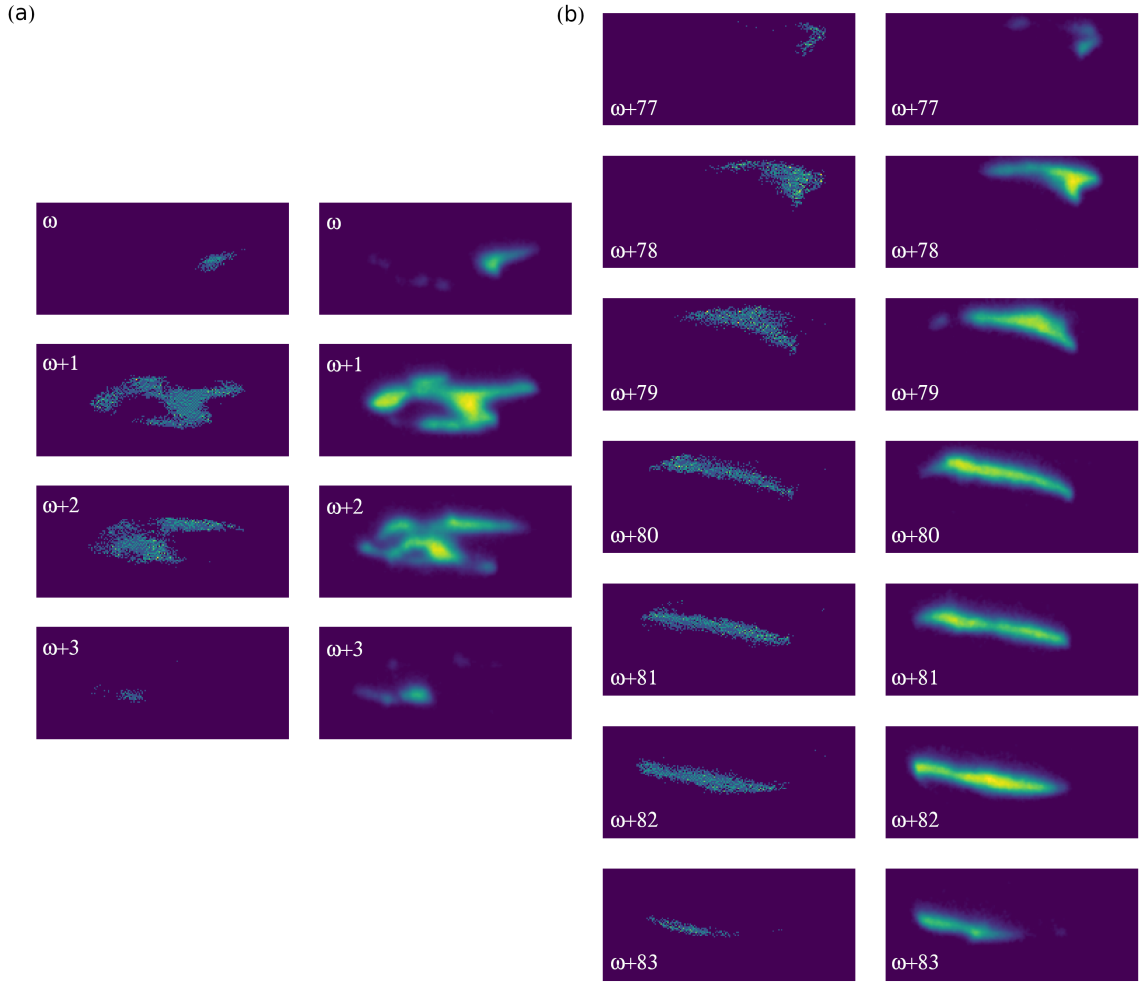

Figure 4.22: Diffraction Peak D, Miller indices $(h, k, l) = (2, 2, 2)$. (a) Initial state, left column is simulated from the reconstructed strain field, right column is the real diffraction pattern, different rows are successive rotation frames; (b) Loaded state, left column is simulated from the reconstructed strain field, right column is the real diffraction pattern, different rows are successive rotation frames. Left and right rows of (a) and (b) do not represent the same rotation frames, there is a shift which reflects an average strain change. The ω values in the images indicate the relative differences of rotation frame indices.

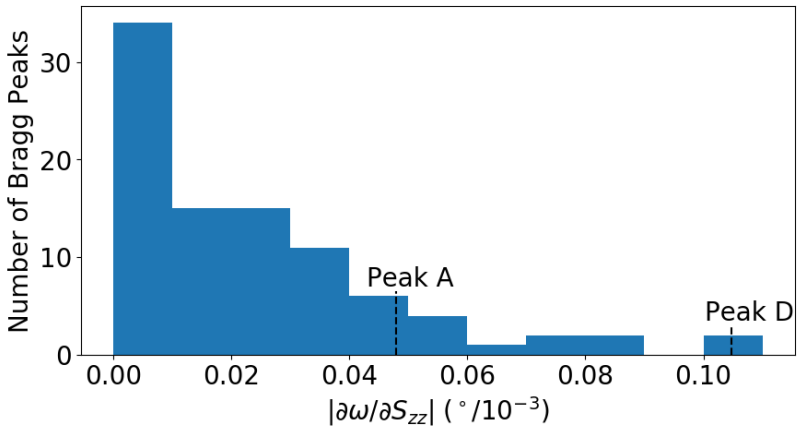

Figure 4.23: Histogram of the values of Eq. (4.7) for all collected Bragg peaks from grain number 15.

peak A, peak B and peak C in Fig. 4.19, Fig. 4.20 and Fig. 4.21, they are split into successive rotation frames with similar number of frames in both initial state and loaded state. However, a few peaks are like peak D in Fig. 4.22, the number of frames in loaded state is much more than the initial state, and the peak seems to be stratified into successive frames.

The sensitivity of the ω_a and ω_b for each reciprocal lattice vector to the strain component S_{zz} can be calculated from their expression in Section 4.2.3. We have

$$|\frac{\partial\omega_a}{\partial S_{zz}}| = |\frac{\partial\omega_b}{\partial S_{zz}}| = \frac{2\mathbf{G}_z^2}{\sqrt{(4\|k\|^2 - 2\mathbf{G}_z^2 - \mathbf{G}_x^2 - \mathbf{G}_y^2)(\mathbf{G}_x^2 + \mathbf{G}_y^2) - \mathbf{G}_z^4}}. \tag{4.7}$$

In nf-HEDM experiments, $\|k\|$ is usually larger than any component of $\mathbf{G}$, therefore larger $\mathbf{G}_z$ with smaller $\mathbf{G}_x$ and $\mathbf{G}_y$ would have larger sensitivity to S_{zz}. We calculated the numerical values of Eq. (4.7) for all collected Bragg peaks from grain number 15, the histogram is shown in Fig. 4.23, the positions of peak A and peak D are annotated.

Therefore, a possible explanation of the peak splitting phenomenon is as following: with and without loading, the change of the intragranular heterogeneity of most strain components are small except the component S_{zz}, so the splitting levels are determined by $|\frac{\partial\omega}{\partial S_{zz}}|$. As a result, the number of split frames are unchanged for most peaks (e.g. peak A and peak B), only a few peaks with large values of $|\frac{\partial\omega}{\partial S_{zz}}|$ (e.g. peak D) are stratified into much more rotation frames under loading.

Chapter 5

Electron Backscatter Diffraction Indexing using Convolutional Neural Networks

5.1 Introduction

Spatial microstructural heterogeneities at the mesoscale ($\sim$1-100 μm), including grain boundaries, phase boundaries, dislocations, defect structures, and chemical segregation, directly control macroscopic material properties and behavior. Currently, the lack of understanding of the complex collective response of mesoscale features to external stimuli poses fundamental challenges in predicting materials' microstructure evolution [102, 103]. This is critical for engineering new materials with tailored properties. Experimental techniques have advanced significantly in the last two decades enabling destructive and non-destructive characterization of material microstructures and their evolution at high spatial and temporal resolutions [104, 105, 106]. With increasing data collection rates and sizes of data sets per sample reaching tens of TBs, there is considerable interest in exploring how efficiently analysis methods based on machine learning can be applied to the reconstruction process. In this work, we show how convolution neural networks (CNNs) can be used as "surrogate" models for solving the inverse problem of reconstructing microstructures from diffraction data.

Electron backscatter diffraction (EBSD) is the most extensively used technique for 2D and/or 3D spatially resolved microstructure characterization of relatively large (0.1-10 mm) polycrystalline samples [75, 107]. EBSD provides orientation maps at sub-grain spatial resolution ($\sim$200 nm) and high crystal orientation resolution ($<$0.5 deg). During an EBSD measurement, an electron beam is focused onto a spot on the sample surface and a diffraction pattern is recorded. Top of the line commercially available orientation imaging microscopes (OIM) can make one such measurement in less than 1 ms [108]. When optimizing for speed, the pattern quality degrades, which results in reduced orientation indexing fidelity with conventional reconstruc-

tion methods [109]. In contrast, the state-of-the-art dictionary method significantly improves the orientation reconstruction accuracy from highly noisy EBSD patterns [109]. Although scan speeds are incredibly high, real-time orientation indexing using dictionary learning approach is not yet feasible, limiting it to be an off-line method [110].

Fast orientation indexing from noisy patterns is crucial for in-situ microstructure evolution [107, 109] and other quantitative studies that require statistically significant volume measurements at high spatial resolution [104]. In spite of progress towards fast data collection times and computation, there is a need for new methods to accelerate the orientation indexing from noisy EBSD patterns, especially if we are to make progress towards real time in-situ studies and 3D microstructure characterization.

Recently, deep convolutional networks have been utilized for a range of imaging techniques from automated image segmentation [111, 112] to image reconstruction for magnetic resonance imaging [113]. While CNNs have demonstrated immense success for problems related to image classification [114] and detection [115], only a few studies have utilized CNNs to address regression problems [116, 117] for improving the performance of a forward model.

Liu et *al*. [118] demonstrated the first application of convolutional neural networks for EBSD orientation indexing from simulated diffraction patterns. Separate CNN models were trained to predict individual components of the crystal orientation. Jha et *al*. [110] extended this approach to predict the full crystal orientation using a deep CNN network, employing mean disorientation in the loss function to account for the non-linearity of the orientation space. However, the implementation of complicated loss functions led to relatively long training times. In both the studies, the models were only trained and tested on simulated EBSD patterns, in contrast to real experimental diffraction patterns; therefore, the effects of measurement noise was not considered. In our research we have found that utilizing simulation-trained CNNs for experimental data can result in low prediction accuracy. In this work, we demonstrate the efficacy of the neural network approach for experimentally measured data with varying noise levels. We present two convolutional neural networks based EBSD reconstruction techniques that are applicable to experimental diffraction patterns and robust towards measurement noise.

5.1.1 Summary of main results

In this work, we utilize the existing physics-based model to generate a large number of training sets that span the entire space for developing faster surrogate models based on convolutional neural networks for predicting crystal orientations from simulated diffraction patterns. Since the simulation trained model cannot be directly used on measured data, the novelty of this work is in the demonstration that a simulation trained model can instead be used as an initial guess or estimate for re-training a separate neural network that only requires a small number of expensive experi-

mentally measured data (300K simulated versus 1K measured patterns). We also demonstrate that the re-training with a straight forward loss function is relatively fast. The robustness of the CNN methods to the measurement noise is demonstrated by collecting experimental data with different exposure times relating to noise levels in the diffraction patterns. Because our techniques are robust to noise, they have the potential to enable higher scan speeds, which are currently limited in part by the fact that the signal to noise ratio drops as the scan speed is increased. The CNN based reconstruction method takes as little as 1 ms for orientation indexing, matching the highest scan rates, enabling real-time orientation indexing. We also demonstrate that a quaternion norm metric provides a good confidence measure for assessing the quality of the reconstruction, without requiring ground truth information.

To the best of our knowledge, this is the first demonstration of the potential of neural network based methods for experimentally measured EBSD diffraction patterns with measurement noise for microstructure reconstructions. The CNN based approach demonstrated here is directly applicable to solving the inverse problems faced by multiple modalities such as transmission electron microscopy, tomography, high-energy X-ray diffraction microscopy, and coherent diffractive imaging for enabling mesoscale microstructure characterization and reconstruction at high rates.

5.1.2 Outline

The basic principle of EBSD (measurements and simulations) is presented in Section 5.2. A brief background on CNNs is reviewed in Section 5.3, and their application to EBSD is presented in Section 5.4. In Section 5.5, we summarize our key findings related to the model's sensitivity to image noise and experimental parameters, and discuss the computational cost of the proposed methods.

5.2 Electron backscatter diffraction

A diffraction pattern (intensity distribution) on a detector, $\mathbf{X} = \mathbf{X}(x, y)$, where (x, y) is pixel location, can be expressed as a function of crystal orientation represented as a quaternion $\mathbf{q} = (q_1, q_2, q_3, q_4)$, of the form:

$$\mathbf{X} = \mathcal{P}(\mathbf{f}(\mathbf{q}|\mathcal{M}, \mathcal{C}, \mathcal{G})), \tag{5.1}$$

where we use symbols $\mathcal{M}$ to parameterize the microscope, $\mathcal{C}$ to denote the crystallography of the sample, $\mathcal{G}$ to represent the geometry of the setup and $\mathcal{P}(\lambda)$ to represent a random Poisson sample drawn from a Poisson distribution with mean λ. Like many other diffraction-based measurement methods, reconstructing a crystallographic orientation from an electron backscatter diffraction (EBSD) pattern is achieved by solving an inverse problem, i.e. finding the inverse function which maps a given diffraction pattern to an orientation: $\mathbf{g}(\mathbf{X}) = \mathbf{q}$.

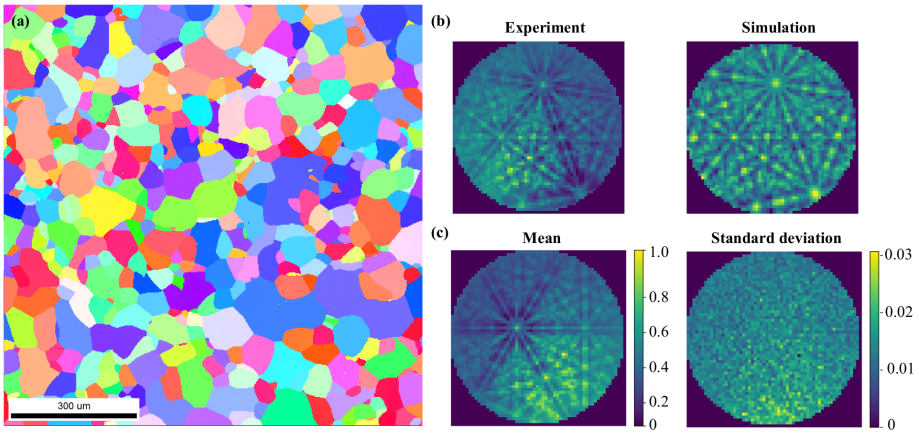

Figure 5.1: (a) Inverse pole figure map of the Ta sample. (b) Measured (left) and simulated (right) diffraction patterns, and (c) mean (left) and standard deviation (right) of the experimental patterns associated with the same crystal orientation. The standard deviation of every pixel intensity is about 0.03, which is the estimated noise in the experimental patterns.

The most commonly used approach for orientation indexing from measured EBSD patterns utilizes image processing techniques including Gaussian filtering, Hough transforms, butterfly convolution, and peak detection for extracting Kikuchi bands [119, 120]. Crystal orientations are reconstructed by comparing the parameters of the measured Kikuchi bands (i.e. angles between lines) with a pre-computed database. Recently, Chen et. *al*. [121] proposed a dictionary indexing (DI) method for microstructure reconstruction based on dictionary generation and pattern matching. A physics-based forward model developed by Callahan et. *al*. [122] was used for the dictionary generation, where the forward model are tuned to the parameters of the experiment and the crystal structure of the sample. Chen et. *al*. simulated a dictionary of diffraction patterns corresponding to a set of orientations that uniformly covered the fundamental zone. In the DI approach, the reconstruction is performed by calculating inner products between an experimental pattern and every simulated pattern in the dictionary. The crystal orientation is then estimated using "k nearest neighbors", by determining k largest inner products. The computational complexity of the dictionary method to index one pattern is $O(dn)$, where d is the dictionary size and n is the number of pixels for each diffraction image, assuming $k \ll d$ [121]. Typically, $n = 60 \times 60$ and $d \sim 3 \times 10^5$ for cubic symmetry materials.

5.2.1 Simulations

The approach presented here utilizes the forward model developed by Callahan et. *al*. [122] to generate a dictionary of a large set of simulation data. We generated a "uniform grid" of 1.5° resolution on the cubic crystallographic orientation fundamen-

tal zone, and simulated the diffraction pattern for each orientation using the *EMsoft* software package [123]. The geometrical parameters for the simulations were obtained from the known detector and sample angles as well as the OIM analysis software fit pattern center corresponding to the central scan point. Further minor refinement of the pattern center parameters was performed using EMsoftWorkbench software provided by the EMsoft package [123]. In total, 333227 pairs of orientations and diffraction patterns were generated.

5.2.2 Measurements

Experimental EBSD diffraction patterns were collected from an annealed tantalum sample with 35 μm average grain size. A 1 mm $\times$ 1 mm area was scanned with 2 μm step size using a FEI Inspect scanning electron microscope equipped with an EDAX Hikari Super camera. The electron beam accelerating voltage was 20 kV, the beam aperture diameter was 50 μm, and the nominal working distance was 20 mm. A diffraction pattern was collected at each sample position, for a total of 501$\times$501 = 251001 diffraction patterns. The inverse pole figure (IPF) map obtained from the OIM analysis software is shown in Figure 5.1(a).

The original detector image was collected at a 1$\times$1 binning and had 480 $\times$ 480 pixels; however, software binning (8 $\times$ 8) was applied on the raw images to yield the 60 $\times$ 60 pixel images used for the CNN modeling. It should be noted that the software binning results in a larger readout noise component compared to CCD hardware binning (in this case approximately eight times larger readout noise). However, for the high signal levels at the long exposure times considered here, the proportion of readout noise, and therefore the difference between hardware and software binning, is expected to be minimal. The measured (left) and simulated (right) diffraction patterns for the same orientation and instrument settings are shown in Figure 5.1(b).

As an approximation, we also estimated the intensity noise in the experimental patterns. Distinct grain orientations in the experimentally measured sample were determined. In an ideal case for ordered samples, the diffraction patterns obtained from orientations corresponding to the same grain should be identical and any deviation from the average value of any given pixel in the diffraction pattern would be due to random noise. Note that the tantalum sample used in this study was well annealed; therefore, it is expected to have low intra-granular misorientations; therefore, this noise calculation procedure (albeit unrepresentative of experimental noise) is reasonable to use in this case. An example of the 2D intensity maps of the mean (left) and standard deviation (right) for a given grain is shown in Figure 5.1(c). We measured the standard deviation of each pixel intensity associated with a given grain orientation and found that the normalized pixel intensities had a standard deviation of approximately 0.03.

The same sample was also used to study the robustness of the CNN model towards the presence of experimental noise. For this purpose, a 1 mm $\times$ 1 mm area of the Ta

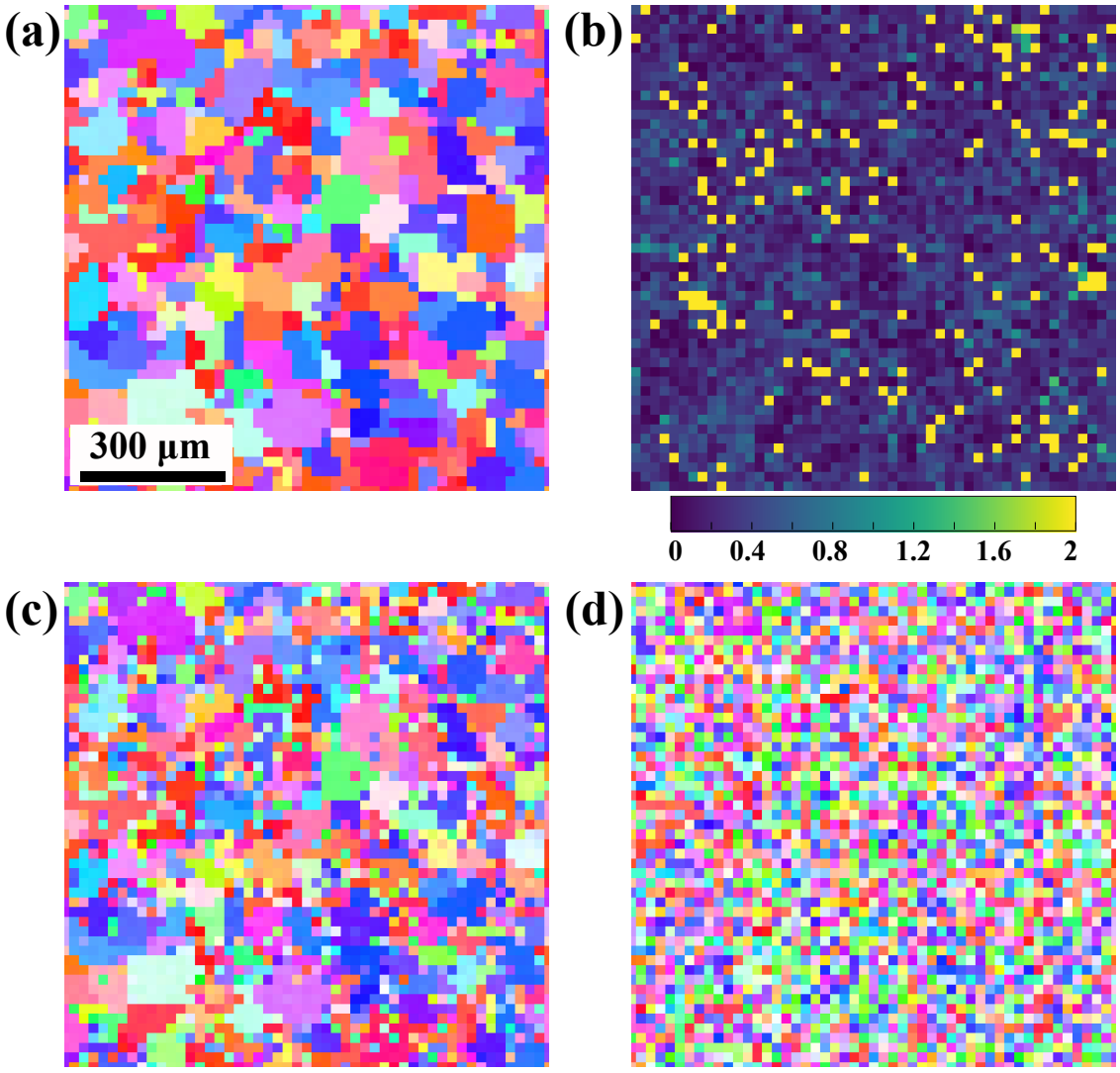

Figure 5.2: EBSD orientation maps of the same region acquired with different exposure times. (a) The first scan acquired with 30 *ms* exposure. (b) Misorientation map showing difference in measured orientations for the first and the last scans, both acquired with 30 *ms* exposure times. The orientation maps acquired with (c) 2 *ms* and (d) 1 *ms* exposure times. Hough transform method produced lower fidelity orientation reconstructions as the noise levels in the diffraction patterns increased with decreasing exposure times.

plate was scanned repeatedly with a 20 μm step size. Different scans were recorded using various exposures ranging from 30 ms to 1 ms per point. The area scanned was identical, and a final scan at the end of the experiment was conducted again at 30 ms exposure to ensure that sample drift was not significant during exposure (i.e. the points scanned and orientations were similar across all datasets). The orientation

maps for 30, 2, and 1 ms exposures are shown in Figures 5.2(a), 5.2(c), and 5.2(d), respectively. Figure 5.2(b) shows the misorientation map showing the difference in orientations between the initial and the final 30 ms exposure time scans. The random distribution of low misorientation angles between the initial and the final 30 ms scan points suggest that sample drift was not an issue.

5.3 Convolutional neural network

5.3.1 Convolutional Neural Network Basics

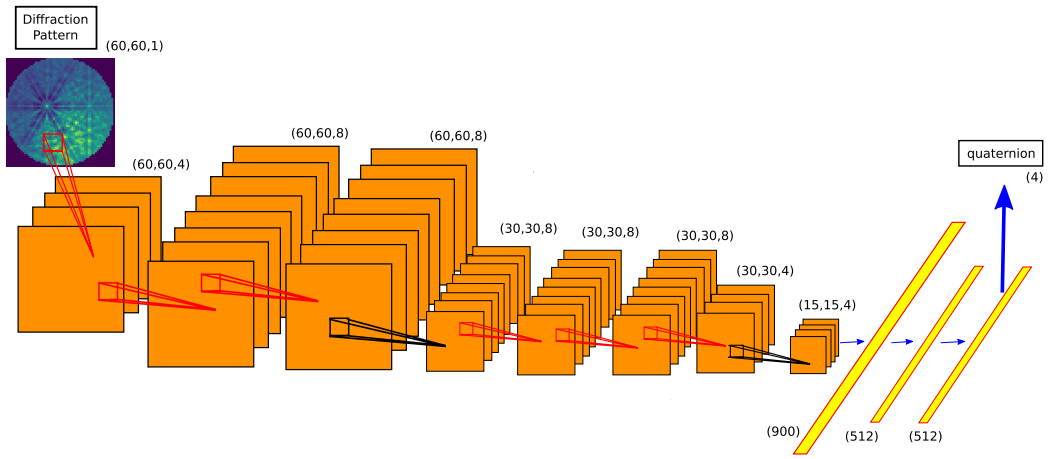

Figure 5.3: Convolutional neural network architecture. The input is a diffraction pattern, which goes through several convolutional layers and then the fully connected layers. The output is four real-valued numbers corresponding to quaternion components that represent a crystal orientation. Numbers in the parentheses show the dimensions of each step. The convolutional operations are shown in red, max pooling operations are shown in black, full connections are shown in blue.

Multilayer feed forward networks have proved to be universal function approximators to learn or estimate a mapping or function between inputs (or features) and outputs (objectives) (e.g. y = f(x)) [124, 125, 126]. In particular, the convolutional neural network has become a key tool for the state-of-the-art methods in computer vision [114]. Unlike deep neural networks where each neuron is connected to all the neurons in the previous layer, the CNN limits such spatial connectivity through a restricted region of activated neurons (receptive field) with shared weights [126]. Taking advantage of such an architecture allows CNNs to have fewer degrees of freedom than traditional multi-layer fully connected neural networks and make convolutional networks more efficient for solving problems related to high-dimensional images.

A convolutional layer can be written as:

$$h^l_{(i,j),c} = \sum_{m=-s}^{s} \sum_{n=-s}^{s} \sum_{c'} w_{(m,n),c,c'} a^{l-1}_{(i-m,j-n),c} + b_{c,c'} \tag{5.2}$$

which is followed by the activation function

$$a^l_{(i,j),c} = ReLU\left(h^l_{(i,j),c}\right) = \max\left\{0,\ h^l_{(i,j),c}\right\},$$

where $h^l_{(i,j),c}$ and $a^l_{(i,j),c}$ are the feature map intensity and activation value at (i,j) pixel coordinates, s is the kernel size and c is the channel index in layer l. The $w_{(m,n),c',c}$ are the convolutional kernel weights between channel c and channel c' of neighboring layers and $b_{c,c'}$ is the bias term.

In our work, we used a 3×3 kernel for all convolutional layers with $s = 1$, the range of m and n was $m, n \in \{-1, 0, 1\}$, and zero padding was employed. The filter numbers (i.e. number of channels) were $4, 8, 8$ in order. After these three convolutional layers, we applied a max pooling layer with a pooling size of 2 and stride of 2, in which all the feature maps were divided into 2×2 non-overlapping units and every unit was assigned an intensity equal to the maximum pixel intensity inside of that unit. The outputs of these layers were new feature maps half the size of the input feature maps.

Next, three convolutional layers and one max pooling layer were applied again, the number of filters for these three convolutional layers were $8, 8, 4$ in order. After that, the feature maps were flattened into a 1D vector and two fully connected layers were applied with each one followed by a $ReLU(x)$ activation function. 512 neurons were used in the fully connected layers. The output layer was similar to the fully connected layer without applying the activation function. The four output neurons corresponded to the four quaternion components representing the crystal orientation.

When fitting a complex model to a small dataset, there is a high chance of overfitting. An overfitted model can describe well the particular dataset that it is trained on, but fails with a comparable level of prediction on unseen data. This lack of generalizability of the trained model can be alleviated to some extent through regularization. We used the mean absolute loss as the objective function, and L2 regularization for the weights of convolutional layers to prevent overfitting. L2 regularization adds the sum of square of weights to the loss function, so that large weights are penalized, effectively making the model "smoother". The total loss function is given by:

$$L = \left\|\hat{\mathbf{g}}(\mathbf{X}) - \mathbf{q}\right\|_1 + \lambda \left\|\mathbf{W}\right\|_2$$

where $\hat{\mathbf{g}}(\mathbf{X})$ represents the feed forward processing of our CNN model and λ is the penalty weight (in our model $\lambda = 0.0001$). The Adaptive Moment Estimation (Adam) algorithm [127], a variant of stochastic gradient descent (SGD), was used as an optimizer to train our model, finding the weights $\mathbf{W}$ and biases $\mathbf{b}$ that minimized the total loss on the training set consisting of $(\mathbf{X_i}, \mathbf{q_i})$ pairs. An approximate smooth

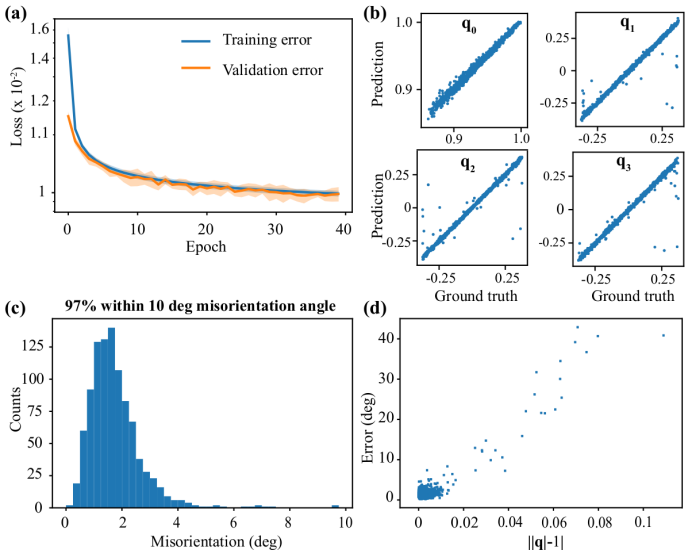

Figure 5.4: Results of the trained CNN model utilizing the simulated EBSD data. (a) Training history: Both training and validation errors converge to about 0.01 after 40 epochs. The shadow area is the standard deviation of 10 runs. (b) Predicted quaternion components of the testing set, where most of predicted orientations (97%) compare well with the ground truth, except for a few outliers. (c) The distribution of misorientation angle between the prediction and the ground truth. (d) The misorientation angle versus deviation from unity of the quaternion norm.

function $\hat{\mathbf{g}}(\mathbf{X_i}) \approx \mathbf{q_i}$ was determined, which well approximated the inverse function $\hat{\mathbf{g}} \approx \mathbf{g}$ for orientation reconstruction from diffraction pattern. Representing crystal orientations as quaternions afforded a good way of estimating the "confidence" metric for model predictions. Any deviation of the norm of a quaternion from one indicated the inaccuracy in model prediction.

5.3.2 Pre-training the CNN using simulated data

We developed a CNN based regression model trained end to end to approximate the mapping from EBSD diffraction patterns to crystallographic orientations. First, the simulated diffraction patterns and the corresponding crystal orientations were used for model training, validation, and testing. Note that the training sets are used for updating the weights of neural network, while the validation set are used for evaluating the performance during the training process. Test set is unseen by the neural network during the training process too and is used to evaluate model accuracy and ensure that the model is not overfitting. All input images were normalized so that pixel intensity ranged between 0 and 1. Figure 5.3 shows the CNN architecture used. A detector image with 60 $\times$ 60 pixels with one channel for intensity was used as input to the CNN. The dimensions of the convolution filters and the fully connected layers

are also shown in Figure 5.3. As described in Section 5.3.1, the detector image passes through a convolutional layer which gets transformed into a feature map which then passes through a non-linear rectified linear unit ($ReLU(x) = \max\{0, x\}$) activation function [128]. The loss function we used for training our neural network is the mean absolute error (MAE) between each quaternion component of the prediction and the ground truth. Empirically, MAE performs better than using mean squared error (MSE) as the loss function on our data set. Pooling layers are also employed occasionally to reduce the size of the feature map and the computational cost. In addition, pooling layers make the network less sensitive to small local features, and help control overfitting to some degree. Finally the outputs of the convolutional and pooling layers go through the fully connected layers, which estimate the final output crystal orientations corresponding to the input detector images. After several convolutional layers and then the fully connected layers, the output of our CNN is four real-valued numbers which represent quaternion components.

We utilized a repeated random sub-sampling validation method, also known as Monte Carlo validation [129]. More specifically, we trained the model several times and each time we randomly split the dataset into training and validation sets, and the errors were estimated by averaging over runs. In each split, we used 1000 pairs for validation, and the remaining 332227 pairs for training. We also randomly generated a separate 1000 pairs of orientations and diffraction patterns from the cubic fundamental zone, which were then used for testing.

The results from 10 separate trainings are shown in Figure 5.4. Figure 5.4(a) shows the training history, where the shaded area is the standard deviation over 10 runs. The plot illustrates that both validation and training errors converged after fewer than 40 epochs, which means that the neural network passed through all the training samples 40 times to update the network weights. Figure 5.4(b) shows the ground truth and prediction of each quaternion component.

Figure 5.4(c) shows the distribution of test error, where misorientation between predicted orientations and ground truth is used as a metric for quantifying the "goodness" of the prediction. As we can see, the peak is about 2° and 97% of the predictions are below 10° misorientation. Note that to employ a simple loss function, crystallographic orientations were represented by quaternions instead of Euler angles, as previously used in the work by Liu et *al*. and Jha et *al*. [118, 110]. By predicting all four quaternion components, we are allowing the quaternions to change in all four directions, while a crystal orientation has only three rotational degrees of freedom. Since all the training data sets have quaternions with unit norm, the training process in effect should penalize the outputs that are far from unity to some degree. This can be observed from reasonably good agreement between the predicted and ground truth orientations shown in Figure 5.4(c). However, to ensure accurate orientation prediction, one could impose explicit constraints that enforces unit norm for output quaternions.

Figure 5.4(d) shows a strong correlation between misorientation angle and the

deviation from unity of the quaternion norm. However, large deviation from unity is an obvious artifact of our CNN model. An interesting observation was that all the outliers had at least one quaternion component close to the cubic fundamental zone boundaries ($\approx \pm 0.383$). An alternative approach to improve the prediction of crystal orientations at the boundary are discussed in the following sub-section.

5.3.3 Outliers near the Fundamental Zone boundaries

One of the difficulties to apply CNN to diffraction images is the outliers near the fundamental zone boundaries, which are caused by the crystallographic symmetry. In a specific fundamental zone, two points at the boundary may be far from each other but physically equivalent. This means that if we use the quaternions in a specific fundamental zone as the ground truth and the MAE as the loss function, the boundary points will not be dealt properly by the CNN model. Physically equivalence implies that the diffraction patterns are the same but the output quaternions look very different. It is therefore not surprising that the CNN model are not trained very well for points near the fundamental zone (FZ) boundary. This is easier to understand in a simpler one-dimensional case. Assuming all crystal orientations are along the same axis and there is no crystallographic symmetry, the neural network are trying to find the map from diffraction pattern to a single angle e. We can constrain $e \in [0, 2\pi)$, which is effectively a "fundamental zone". There will be problems for the neural network near the fundamental zone boundaries. For example, the diffraction patterns from $e = 0.001$ and $e = 1.999\pi$ are very similar, but during the training process the neural network is forced to predict very different angle values for these diffraction patterns. So, the neural network can not be trained very well at the boundaries. One solution is to train another neural network to map diffraction patterns to $e \in [\pi, 3\pi)$. $[\pi, 3\pi)$ is a new "fundamental zone" and it overlaps with $[0, 2\pi)$, and they don't have the same boundaries. This new neural network performs bad at angles near $e = \pi$, but it performs well on angles near $e = 0$. By combining these two neural networks, we can predict every angle very well.

Jha et *al*. [110] accounted for the near boundary points in their CNN model by implementing an averaged disorientation angle based loss function. Although this complex loss function can yield improved reconstructions near FZ boundary, it significantly deteriorates the reconstruction speed. An alternative approach while using a simple MAE loss function to address this problem is to train several CNNs on different fundamental zones. Those fundamental zones are overlapped so that almost no point is at the boundaries of all the fundamental zones. More specifically, since we only have unity norm quaternions, we can use scatter plots in 3D to represent the quaternions where x, y, z axis are three quaternion components q_1, q_2, q_3. Fig. 5.5 (a) is one of its projection, each point represents a quaternion in the test set, and we labeled all the reconstruction outliers with red dots. In this figure (and other projections not shown here) you we find that the original fundamental zone is close

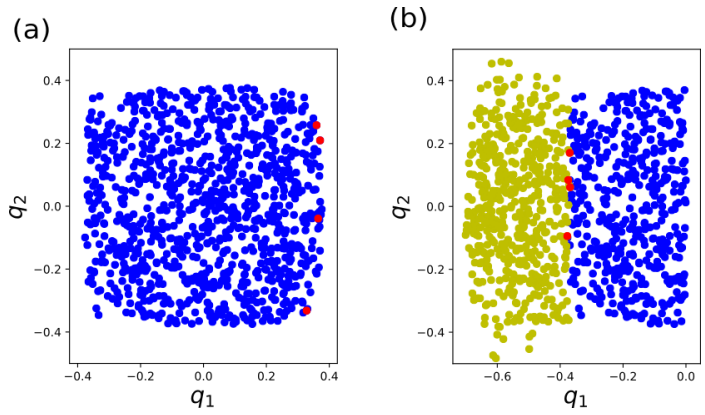

Figure 5.5: (a) q_1, q_2 projection of the 3D scattering plot of normalized test quaternions in the original fundamental zone, red dots are reconstruction outliers. (a) q_1, q_2 projection of the 3D scattering plot of normalized test quaternions in a transformed fundamental zone, yellow dots are transformed quaternions and red dots are the original outliers.

to a cubic with rounded corners and curved edges, and all outliers are at the boundary ($q_1, q_2, q_3 \approx -0.38$). For those quaternions whose $q_1 > 0$, we applied a transform $m = \begin{bmatrix} 1 & 0 & 0 \\ 0 & 0 & 1 \\ 0 & -1 & 0 \end{bmatrix}$ (one of the cubic symmetry operation) to their rotation matrix, so we get new quaternion representations of those orientations, then the scatter plot for all orientations is shown in Fig. 5.5 (b), in which the yellow dots are the transformed quaternions, blue dots are the quaternions not have been transformed and the red dots are original outliers. We use these quaternions as the training label to train another CNN. For this new "fundamental zone", quaternions whose $q_1 \approx -0.38$ are not at the boundary anymore, so this CNN can perform well on these quaternions. Similar transformations can be applied to get other two fundamental zones which can cover the outliers around $q_2 \approx -0.38$ and $q_3 \approx -0.38$, and two more CNN are training on those transformed fundamental zones.

The predicted orientation of a diffraction pattern is then chosen based on the deviations from unit norm of the predicted quaternions from all four models. To demonstrate the effectiveness of this idea, we trained four CNNs on the same diffraction patterns but the quaternion labels are transformed to different fundamental zones that overlap with each other.

Figures 5.6(a) and 5.6(b) show the model prediction at the end of the training process for the single and multiple CNN methods, respectively. For the training and validation sets (333227 data points), the original model had 4307 (1.29%) outliers and the multiple-FZ approach had 191 (0.05%) outliers, where outliers are defined as quaternions with larger than 10° misorientation angle with the ground truth. Similar comparison for the test set using the multiple CNN method is shown in Figure 5.6(c)

and the error versus deviation of the predicted quaternion norm from unity is shown in Figure 5.6(d). For the test set (1000 data points), the original model had 22 outliers and the multiple-FZ approach had 1 outlier. The results in Figure 5.6 demonstrates significant improvement in orientation predictions from CNNs trained on multiple fundamental zones as opposed to a single one.

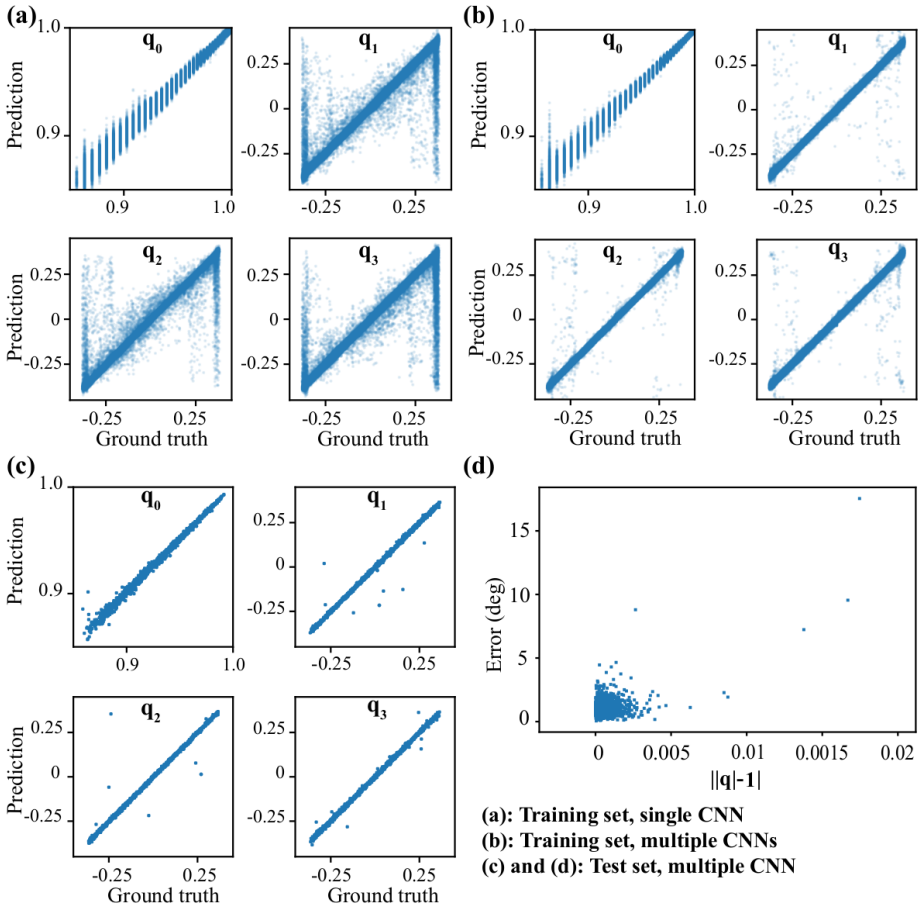

Figure 5.6: The predicted quaternion components versus the ground truth for training data set from (a) a single CNN model and (b) combination of four CNNs. The four models are trained on four different fundamental zones, and for each orientations, quaternion with the smallest deviation from the unit norm is chosen. Finally, all the predicted quaternions are transformed to the original fundamental zone. (c) The comparison between the ground truth and the predicted quaternions from the multiple CNNs and (d) the misorientation angle versus deviation from unity of the quaternion norm for the test data sets.

5.4 Application of CNNs to experiment

Due to inherent assumptions in the forward model, differences between the simulated and experimental diffraction patterns are expected. Two approaches based on adaptive learning were utilized to apply the CNN initially trained on the simulated patterns to experimentally measured EBSD data. 1) Domain transform: This method is based on training a separate model that maps the experimental patterns to the simulation patterns, so that the originally trained CNN model could be utilized for orientation reconstruction. 2) Transfer learning: This method used a portion of the experimental patterns for retraining the parameters of the convolutional layers in the CNN model trained on simulated data, while fixing the parameters of the fully connected layers of the original network. These two methods are described in more detail in in the following sections.

5.4.1 Domain transform using U-Net

Transformation of experimental patterns to simulated patterns was achieved through the U-Net architecture shown in Figure 5.7(a). The U-Net employs a stack of convolutional layers to encode the high level information from the input patterns and then uses a stack of "deconvolutional" layers that decode the spatial information [130]. The loss of details during the down sampling in the encoder is accounted for by the U-Net through "skip-layer" connections between the encoder and the decoder. In our U-Net, the first convolutional layer had a 3×3 kernel size, 16 filters and stride 1. It was followed by two convolutional layers with kernel size 5×5, 32 filters and stride 2, which effectively downsized the feature maps by 2. A feature map refers to the spatial information regarding the distinct activation of neurons after applying a convolution filter across the previous layer (image). After these three convolutional layers, three deconvolutional layers were applied. The first two deconvolutional layers had kernel size 5×5, 32 filters and stride 2, which expanded the feature maps by a factor of 2. The final deconvolutional layer had kernel size 3×3, 1 filter and stride 1, which generated the output images. The "skip-layer" connections concatenated the feature maps from the same level of encoder and decoder layers, and then used it as the input for the next decoder level. We used mean absolute loss as the objective function, and L2 regularization for the weights to minimize the risks of overfitting.

Since the simulated patterns were already very similar to the corresponding experimental patterns, a small training set was adequate to train the U-Net. We randomly picked 1000 pairs of experimental and simulation patterns for training out of the total 251001 patterns, and another 100 pairs for testing. The training data and testing data were chosen from different regions of the sample, to ensure no overlap. Figure 5.7(b) shows one example of experiment pattern, simulation pattern, U-Net transformed pattern, and the difference between simulation and U-Net transformed patterns (left to right). The lack of any discernible features in the difference plot suggests that

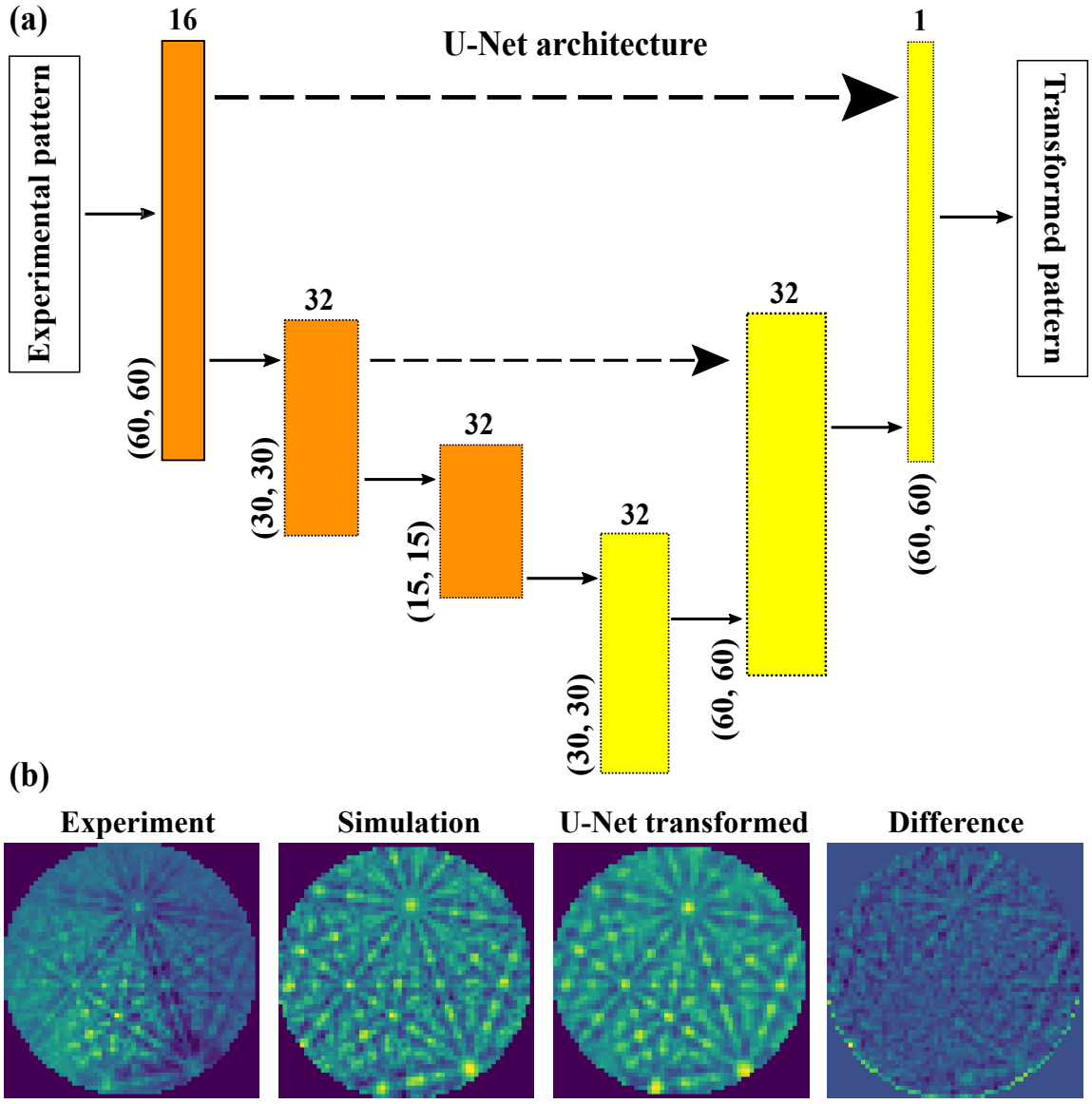

Figure 5.7: (a) U-Net architecture. The numbers in parentheses are the dimensions of feature maps, and the numbers on top of each layer corresponds to the number of filters. Dashed arrows denote the "skip-layer" connections. The measured diffraction pattern is input to the network and the output is the transformed pattern, which resembles the simulated pattern. (b) An example of transformed image. From left to right is the experiment pattern, simulated pattern, U-Net transformed pattern, and the difference between simulated and U-Net transformed pattern.

the difference between the simulated and U-Net transformed images are very small, which means the U-Net transformed patterns are appropriate to use as the input for the pre-trained CNN on simulated patterns.

5.4.2 Transfer learning via re-training

The second method was inspired by retraining via "fine tuning" as used in machine learning [131]. Transfer learning refers to the idea of exploiting the learned information in one setting to be adapted for another similar setting. That is, given a CNN trained for one purpose or data set, only a few samples are needed to train it for another purpose, while keeping some of the weights fixed. In our case, we had a CNN model that was trained on the simulated data, and we assumed that the convolutional layers learned the low level features of the images, and the fully connected layers learned the high level concepts, i.e., the inverse function. We therefore retrained the convolution layers in the original CNN model using the experimental patterns, while keeping the weights of the fully connected layers fixed. A similar idea has been applied to cross modal learning [132].

5.5 Results and Discussion

5.5.1 Implementation on experimental data

Figure 5.8 shows the results of applying U-Net and re-trained CNN methods for EBSD measurements of the 1mm $\times$ 1 mm tantalum sample shown in Figure 5.1. The orientations were reconstructed from diffraction patterns using the Hough transform method and were used as the ground truth. Figures 5.8(a) and 5.8(d) display the misorientation maps between the prediction and the ground truth. The red dots correspond to the sample location from which the diffraction patterns were taken for training the network. Although many grains were not covered by the training set, most of the orientation reconstructions for the unseen data were accurate within 10 degrees misorientation. Note that a low misorientation angle between the prediction and the ground truth indicates accurate prediction. High misorientation angle is observed for the grain boundary pixels, for which the Hough transform exhibits low fidelity reconstructions. Figures 5.8(b) and 5.8(e) show the spatial distributions of the deviation of the predicted quaternion norm from unity. The misorientation and quaternion norm plots indicate that large misorientation corresponds to quaternion norm that deviates away from the ideal value of 1. Therefore, the norm of the output quaternion provides a metric for quantifying the prediction error. This is very important for real applications, where ground truth information is not available. The same training and testing sets were used for both domain transform and transfer learning methods. The testing error distributions are shown in Figure 5.8(c) and 5.8(f) from U-Net and re-trained models, respectively. Slightly larger spread in misorientation distributions were observed for experimental images in comparison to the misorientation distribution predicted for simulation patterns, as seen in Figure 5.4.

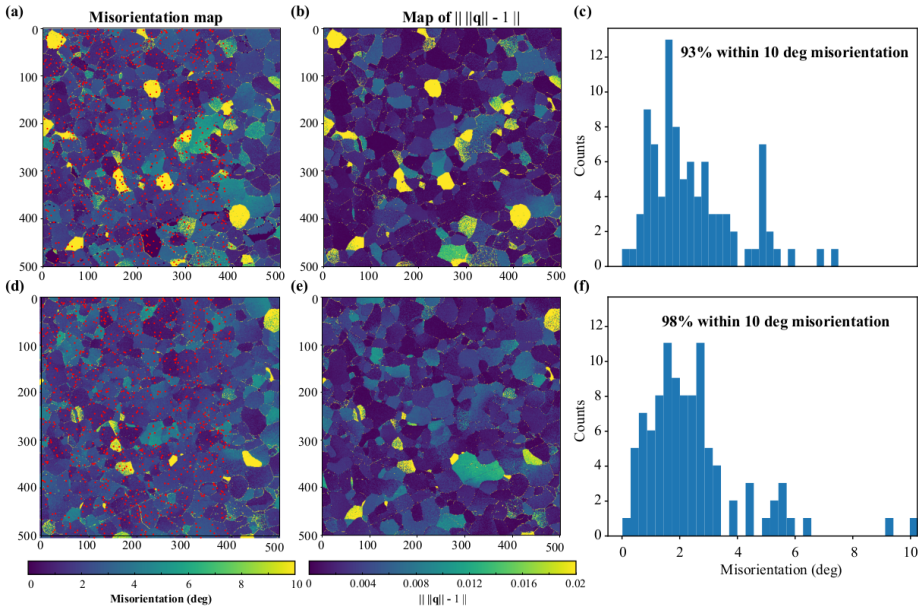

Figure 5.8: (a), (d) The misorientation map between the predicted and the ground truth crystal orientations. The red points correspond to the positions from which measured diffraction pattern and crystal orientation pairs were used for training the U-Net and the re-trained networks. (c), (f) Misorientation distribution calculated for the 100 measured patterns, randomly chosen from the right most side of the sample (unseen during training), used as a testing set for the two models. The measured diffraction patterns from the remaining Ta sample positions were used for orientation prediction. Low misorientation angle indicates good agreement. (b), (e) Norm of the predicted quaternion map indicate the quality of the reconstruction. Higher norm indicates higher prediction error.

5.5.2 Robustness to pattern noise

To study the robustness to measurement noise, we used the same area scan of the Ta sample with different exposure times shown in Figure 5.2. The orientations from diffraction patterns acquired with 30 ms exposure were reconstructed using the Hough transform method and were used as the ground truth. In total, $51 \times 51 = 2601$ pairs of orientations and diffraction pairs were measured, where 2000 pairs were used as a training set and the remaining 601 pairs were used for testing. FusionNet [112] architecture was used for orientation reconstruction. FusionNet like U-Net can learn the transformation from the real experimental patterns to the simulated patterns, while demonstrating higher accuracy, especially, for images with high noise levels.

Figure 5.9(a) shows the results of applying FusionNets to the experimental patterns of the same orientation but different exposure times. The top row is the experimentally measured patterns and the bottom row corresponds to the transformed patterns. The pattern quality significantly degraded with decreasing exposure times.

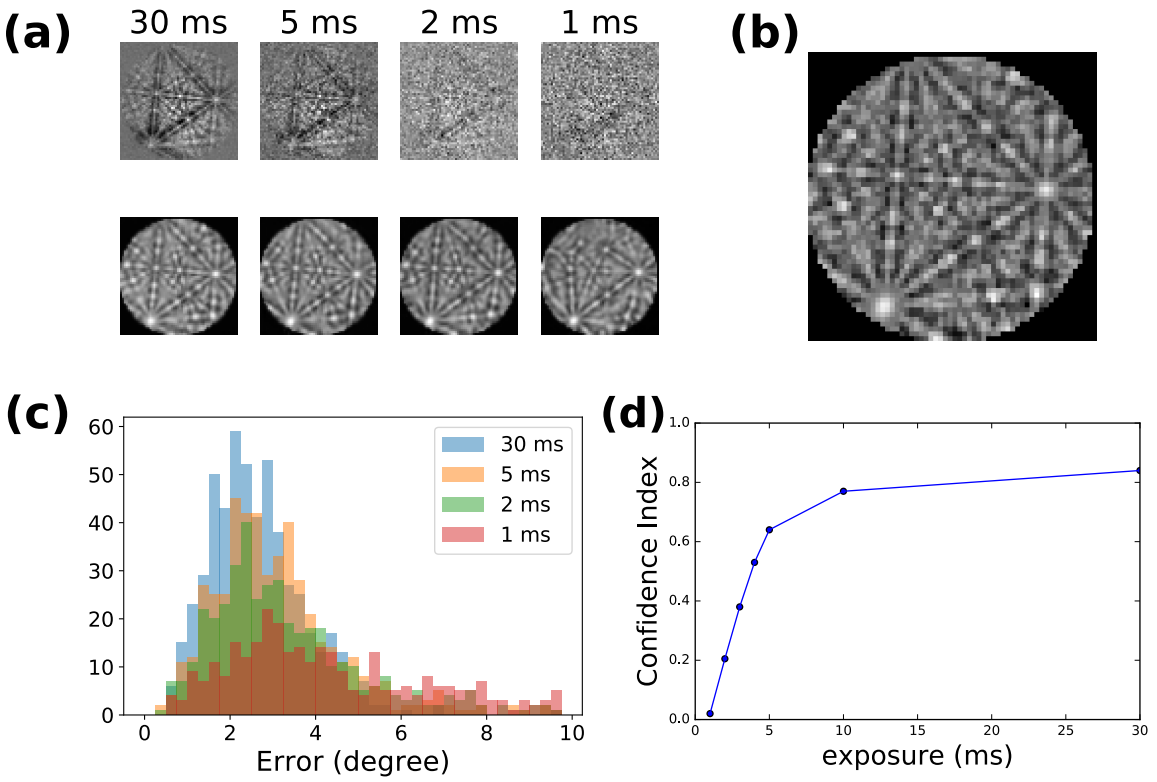

Figure 5.9: The robustness of model prediction to noise was investigated by scanning the same area of the Ta sample with different exposure times. The results of diffraction pattern with different exposure times. (a) Diffraction patterns with different exposure times of a same example orientation. The first row is the raw images and the second row is the transformed images that were used as the input for our CNN model. (b) The simulated pattern corresponding to the same orientation in (a). (c) The error distribution of different exposure times. The percentages of orientations that have errors less than 10° are 95%,85%,71%,53% for exposure time 30 ms, 5 ms, 2 ms, and 1 ms, respectively. (d) Averaged confidence index for Hough transform reconstruction of different exposure time.

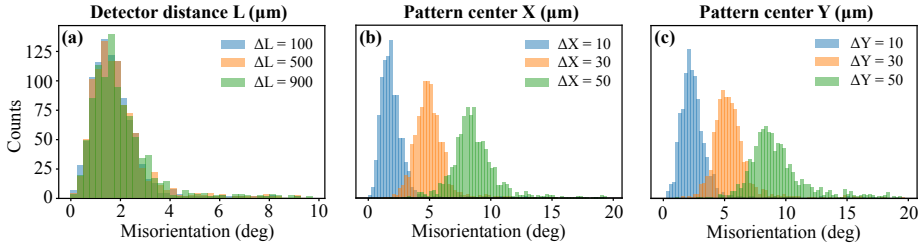

Figure 5.10: The misorientation distributions when the training and testing patterns are generated under different detector parameter setups. (a) The sample to detector distance is different for training and testing data, where the offset unit is μm. (b) The pattern center X coordinate on detector are different for training and testing data. (c) The pattern center Y coordinate on detector are different for training and testing data. The offset units for X and Y are given in number of pixels (pixel size is 71.4 μm).

With shorter exposure times, the reconstructed pattern is more deformed, but many features are retained in the transformed image. Figure 5.9(b) shows the simulated pattern corresponding to the same orientation in 5.9(a). Misorientation distributions between the measured and the predicted orientations are shown in Figure 5.9(c). The results demonstrate that the CNN approach can to a degree learn to index very low-quality diffraction images. The confidence index of the orientations reconstructed using the OIM software is shown in Figure 5.9(d) for comparison. Although, decrease in reconstruction accuracy for images with high level of noise was observed for both CNN and Hough transform methods, Figure 5.9 demonstrates that neural networks are robust to noise in diffraction patterns, and does not require pre-processing step when dealing with noisy data.

Recent studies have also demonstrated CNNs' robustness to noisy data [133, 134]. This is not surprising because convolutional layers have been shown to be capable of learning the features from the training data to recover a clean image from a noisy observation [135, 136, 137]. Moreover, CNNs can learn high level features automatically and are very robust to local noise, which makes them outperform traditional methods based on handcrafted features, which involve pre-determining characteristic regions or descriptors of an image, utilized in many computer vision tasks [113, 114, 115, 138].

5.5.3 Effects of experiment parameters uncertainty

Another challenge always encountered in experiments is the uncertainty in experimental setup parameters. We conducted a parametric study to investigate the effect of instrument setup uncertainty on model prediction. For that purpose, we trained our model with simulated images generated from one set of detector parameters, and tested it on the images that were generated using different setup parameters. The results are shown in Figure 5.10. In Figure 5.10(a), we only changed the distance

between the detector and the sample, keeping everything else fixed. As long as the distance offset was smaller than 900 μm, the results were not strongly influenced. Figures 5.10(b) and 5.10(c) show the effects of X and Y translation, which caused the error to shift towards the right suggesting poor prediction. The extent of this shifting was dependent on the choice of the experimental setup, and in our case, it was about 4° per 20 pixels (pixel size is 71.4 μm). This was expected because detector translation and crystal rotation have approximately the same effect on the EBSD pattern. Therefore, similar to Hough transform and dictionary methods, the proposed CNN based approach also requires determination of the experimental setup parameters before reconstruction. Note that a correction for the orientation error induced by the pattern center shift across a large area EBSD scan can be applied using the method described in Singh et al. [139]. While we do not use this correction factor here, as we are primarily interested in demonstrating that large reconstruction errors can be reduced through re-training (shown in Figure 5.8), accounting for the pattern center shift as a function of scan position may further reduce the low misorientations shown in Figure 5.8(f).

5.5.4 Computational cost

Compared to a dictionary approach, one advantage of using neural networks is increased computational performance. Reducing computation time is an important consideration in designing a network architecture. As we can see from Equation 5.2, the computation time for each pixel in the convolutional layer is proportional to the kernel size and the number of filters, which is related to the number of computations performed by the network. Thus, reducing the number of layers and keeping the kernel size and filter numbers managable for the convolutional layers will increase the performance. However, a CNNs' ability to approximate complex functions depends on the network size [140, 141], and the prediction power will decrease with decreasing network size.

The network architectures of the CNN and U-Net used in this work were optimized for both computational performance and prediction accuracy, and we demonstrated that the models generalized well for both unseen simulated and experimental data sets. Using the network structure described here, the U-Net method took about 17 minutes to reconstruct the 1×1 mm^2 scanned region (251001 data points) on the sample (i.e. 4 ms per pattern) on a MacBook Pro with a 2.8 GHz Intel Core i7 processor, and the retrained CNN took about 5 minutes (i.e. 1 ms per pattern). Furthermore, there are many neural network frameworks (e.g. tensorflow [142]) that can utilize GPUs to further speed up the reconstruction without changing the code.

5.5.5 Combining CNN with the dictionary approach

Both Liu et *al*. [118] and Jha et *al*. [110] reported the dictionary indexing approach to be slower than the CNN method. In this work, we have demonstrated that the CNN-based method is very fast and can enable real-time reconstructions during the scanning process. However, the CNN method is not as accurate as the dictionary approach, which can reconstruct noisy data with high accuracy. This can be addressed by combining the two approaches: first apply CNN-based regression to obtain preliminary predictions and a measure of confidence for each location given by the norm of the predicted quaternion. For locations with high confidence reconstructions, run the pattern matching only in the neighborhood (e.g. 10°) of the preliminary results in the dictionary. For those with low confidence, run the full dictionary search.

5.5.6 Regularization

Regularization is important for reducing the chance of overfitting. We used L2 regularizations for our models without using dropout [143]. Dropout is a common regularization technique used in most CNN classification problems. It randomly forces the neuron activations to be zero in training, but does nothing in testing. Previous studies have shown that dropout can improve the performance of a particular CNN-based regression model. For example, Kendall et. *al*. [144] used dropout in their model to infer camera positions from a picture taken by that camera, and saw improved predictions. We tried two dropout ratios $(0.3, 0.5)$ in our CNN models, but they resulted in lower fidelity predictions. However, without dropout, we obtained validation errors that were already as low as the training error, as seen in Figure 5.4(a). The reconstruction accuracy (mean error and variance of error) of our model for unseen data and for training data was similar, indicating that overfitting was not taking place.

5.5.7 Microstructure reconstruction

Experimental EBSD data reconstruction was performed by employing two adaptive learning networks. One of the reasons for not training another CNN model from scratch was due to the lack of labeled experimental patterns that spanned the entire orientation space (fundamental zone) for a given material crystal structure. We observed that both the domain transform and transfer learning methods improved the accuracy of the experimental data reconstruction. This improvement can be understood by looking at the activation map of the last convolutional layer, which after max pooling is the input to the fully connected layer.

Figure 5.11 shows one such example from the test data set. Four feature maps are shown, one for each of the four filters in the layer. The first row is the simulation image and the filter outputs of the original CNN. We can see that some features related to Kikuchi bands have been learned. The second shows the results of inputing

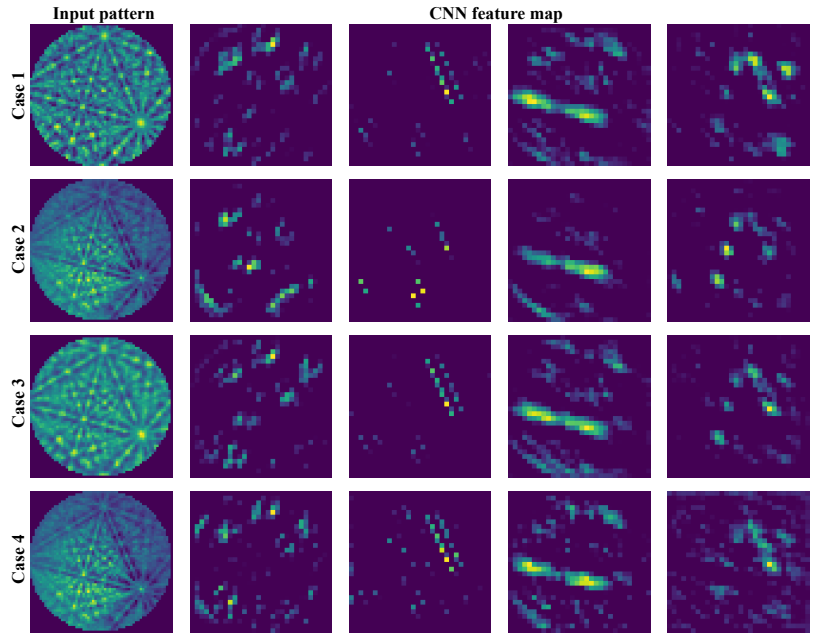

Figure 5.11: Activation maps for the last convolutional layer. Case 1: simulated pattern as input to the original CNN. Case 2: experimental pattern as an input to the original CNN. Case 3: U-Net transformed pattern as an input to the original CNN. Case 4: experimental pattern as input to the re-trained CNN.

experimental data into the CNN model which has been trained on simulations only. Clearly the original CNN will respond differently to experimental and simulation patterns. The difference was significant enough that the original CNN was unable to accurately predict quaternions for experimental patterns.

The third row shows the filter outputs after a U-Net transformed image is fed into the original CNN; the activation maps look very similar to those shown in the first row, which were generated from the simulated image. In the fourth row, we retrained the CNN so that the weights of convolutional layers were adapted to the experimental images. We can see that the activation maps are also very similar to those in the first row, which supports our assumption that differences between simulation and experimental patterns are low level features and they can be learned solely by convolutional layers.

The two approaches presented here for experimental pattern indexing are simple and robust. Similar studies have being conducted on transfer learning and domain transforms [145]. One such example is a generative adversarial networks (GAN) [146] that is utilized to transform images from one domain to another [147, 148]. Essentially, the generative networks are learning the metric for measuring similarity between images produced from different modalities, which is similar to our approach utilizing the U-Net and FusionNet to transform experimental patterns to simulated patterns.

Chapter 6

Conclusions and Future Work

In this thesis, we have presented several numerical methods for polycrystalline microstructure reconstruction and analysis. These computational tools are still under development and they will keep improving our characterization techniques and extract more scientific merits from the data.

6.1 Grain Coarsening in the α-phase Iron

New X-ray probes of three dimensional grain geometries and evolution which study significant volumes of microstructure are leading to improvements in understanding of grain coarsening phenomena. The summary statement at this point is that averages over topological classes follow expected behavior based on isotropic models of curvature driven evolution, but that individual grains deviate by large amounts from this simplified model.

In future work, Euler relation can be used for testing the reliability of our code for counting the number of grain faces (neighbors), edges (triple lines), and vertices (quad points). The theoretical study of the relation between excess face number and the averaged total curvature is also important and it can give us some clues that under what conditions and circumstances this relationship holds. It may be valuable for grain coarsening theories.

Further understanding can be expected based on the combination of improved experimental methods and facilities and on the use of modern numerical methods. For example, it appears to now be practical to extract grain boundary energies from geometries of very large numbers of triple junctions [48] such as measured here. This approach may then provide a means for separating the roles of energy and mobility. It has also been suggested that this separation may be possible through purely experimental observations of boundary motions. [5]

6.2 Determining Grain Boundary Energies

In this work, a new framework for reconstructing grain boundary energy from triple junction geometry is demonstrated. This new framework gives good reconstruction results with 6×10^4 triple junctions, even when the data are noisy. With more data, the reconstruction results have smaller error. In addition, the performance on a small clustered dataset is also good enough to give information about the grain boundary energy function.

Future research will study the performances of this non-parametric reconstruction framework on different energy function models and with different forms of regularization terms. Along with numerical experiments, theoretical analyses are also needed to provide the uncertainty of the determined grain boundary energies.

6.3 nf-HEDM for Intragranular Strain

The non-destructive nature of nf-HEDM makes it an attractive method to measure the in-situ evolution of material microstructures. In this work we demonstrate a potential expansion of the output to include spatially resolved intragranular elastic strains. Based on sensitivity analysis in Section 4.5, high signal to noise ratio diffraction images and accurate experimental geometry determination are crucial for a reliable strain reconstruction.

The strain levels used in this proof-of-principle demonstration are higher than many materials can sustain (10^{-2}). Because in the MASSIF simulation we applied a uniform load perpendicular to the cross section, the macroscopic strain must be as high as 10^{-2} so that the intragranular strain heterogeneity is large enough to be measured. Fortunately our Ti7Al sample was bent under loading, which generated larger level of heterogeneity.

Higher sensitivity may be obtainable by using yet smaller $\delta\omega$ integration intervals; of course, this increases the computational burden. As $\delta\omega$ is reduced, we get more resolution on the Bragg angle (ω_a, ω_b), and therefore better resolution of strain components, however, other experimental sources of broadening need to be carefully considered. Another possible way to improve the reconstruction is adding the regularization for strain field smoothness in **GlobalCost** in Algorithm 3, which should reduce the noise in the reconstruction. As shown in Section 4.6.3, the reconstruction near the grain boundaries may not be correct due to the residual uncertainty of geometry parameters and boundary positions. However, the strains near boundaries usually draw researcher's interests. One possible solution is to define a "combined global cost function" which measures the goodness-of-fit of simulations from a group of neighboring grains to their diffraction patterns, and then fine-tune the geometry parameters and boundary positions based on this "combined global cost function". Further, experimental intensity patterns within diffraction spots may reflect phenomena beyond the strain induced re-direction of diffracted intensity. One example is

intensity modulation due to local defect distributions. These considerations will be the subject of future work.

Our intragranular strain reconstruction algorithm is in its infancy. To make it easier for the reconstruction and comparison with modes, samples with minimal orientation gradients, relatively large elastic strains and large grain size ($\sim 100\,\mu m$) are preferred. The property of strong X-ray scattering is also beneficial since it decreases the measurement time.

Extracting micron scale strain tensor resolution inside materials is attractive since it can aid in model development and validation. A recent work [149] about reconstructing sub-grain elastic strain with Diffraction Contrast Tomography has been done, which used a very similar experiment setup as ours. Recent work of Hayashi et al [89] demonstrates both an alternate approach and the strong motivation for such measurements. Their measurements were performed with the presence of plastic strain, and the result showed unexpected large off-diagonal strain and stress values. With improved sensitivity and upgraded synchrotrons, nf-HEDM can extract similar information over larger volumes (due to requiring only one dimensional scanning of the sample), further research can be done for the comparison between this two approaches.

6.4 CNN for EBSD Indexing

This work demonstrated the effectiveness of two CNN approaches for microstructure reconstruction from measured EBSD patterns. Both approaches initially trained the CNN with a large number of easily generated simulation data and then utilized a relatively small number of expensive experimentally measured patterns to either retrain several convolutional layers or transform experimental patterns into simulated patterns. Both methods were successfully demonstrated on a tantalum sample with a body centered cubic crystal structure. The proposed CNNs demonstrated robustness to real experimentally measured data with varying noise levels (achieved by changing exposure times during data collection) and reconstructed orientation while matching the highest EBSD scanning rates. The proposed quaternion norm as a measure of confidence was demonstrated to be a strong indicator for assessing the reliability of the reconstructions. This will be crucial for determining the quality of reconstructions for real applications, when the ground truth is not available.

Our study demonstrated generalizability of the CNN method to experimental data in the presence of noise, but also revealed that the current method is still not at a state where it can outperform the conventional reconstructions on noisy data that is possible either through Hough transform or dictionary learning. However, the CNN based orientation indexing methods presented here, if combined with the dictionary search method has the potential to accelerate the reconstruction and improve the reconstruction quality, beyond what is currently possible. Rigorous studies of hyper-parameters and network architecture optimization along with implementa-

tion of physical loss functions can further reduce the computation cost and minimize prediction outliers. Until the effectiveness of this reconstruction method is fully established, the work here clearly illustrates the limitations of CNNs to this problem when applied to experimentally measured data with high noise levels. Future work also entails testing the proposed method on different material systems and various experiment setups.

Bibliography

[1] J. K. Mackenzie. Second paper on statistics associated with the random disorientation of cubes. *Biometrika*, 45:229–240, 1958.

[2] D. A. Aboav. The arrangement of grains in a polycrystal. *Metallography*, 3:383–390, 1970.

[3] D. Weaire. Some remarks on the arrangement of grains in a polycrystal. *Metallography*, 7:157–160, 1974.

[4] SF Li and RM Suter. Adaptive reconstruction method for three-dimensional orientation imaging. *Journal of Applied Crystallography*, 46(2):512–524, 2013.

[5] S. Maddali. *Computational mining of meso-scale physics from high-energy X-ray data sets*. PhD thesis, Carnegie Mellon University, 2016.

[6] J.Wang, A.V. Nguyen, and S. Farrokhpay. A critical review of the growth, drainage and collapse of foams. *Advances in Colloid and Interface Science*, 228:55–70, 2016.

[7] S. Hilgenfeldt, S.A. Koehler, and H.A. Stone. Dynamics of coarsening foams: Accelerated and self-limiting drainage. *Phys. Rev. Lett.*, 86:4704–4707, 2001.

[8] S.A. Magrabi, B.Z. Dlugogorski, and G.J. Jameson. Bubble size distribution and coarsening of aqueous foams. *Chemical Engineering Science*, 54:4004–4022, 1999.

[9] Robert D. MacPherson and David J. Srolovitz. The von neumann relation generalized to coarsening of three-dimensional microstructures. *Nature*, 446(7139):1053, 2007.

[10] J Von Neumann. Metal interfaces. *Cleveland Ohio: American Society for Metals*, page 108, 1952.

[11] William W Mullins. Two-dimensional motion of idealized grain boundaries. *Journal of Applied Physics*, 27(8):900–904, 1956.

[12] Gregory S Rohrer. Grain boundary energy anisotropy: A review. *Journal of Materials Science*, 46(18):5881, 2011.

[13] E O Hall. The deformation and ageing of mild steel: III discussion of results. *Proceedings of the Physical Society. Section B*, 64(9):747, 1951.

[14] NJ Petch. The cleavage strength of polycrystals. *Journal of the Iron and Steel Institute*, 174:25–28, 1953.

[15] Kwai S. Chan. Roles of microstructure in fatigue crack initiation. *International Journal of Fatigue*, 32:1428 – 1447, 2010.

[16] Cyril Stanley Smith. Grain shapes and other metallurgical applications of topology. *Metal Interfaces*, pages 65–113, 1952.

[17] Cyril Stanley Smith. Some elementary principles of polycrystalline microstructure. *Metallurgical Reviews*, 9(1):1–48, 1964.

[18] ME Selleck, K Rajan, and ME Glicksman. Organic materials as an experimental model system for grain growth studies. *Simulation and Theory of Evolving Microstructures*, pages 79–84, 1989.

[19] MP Anderson and AD Rollett. Simulation and theory of evolving microstructures. *The Minerals, Metals and Materials Society, TMS Publication*, 1990.

[20] G Abbruzzese, I Heckelmann, and K Lücke. Statistical theory of two-dimensional grain growth i. the topological foundation. *Acta Metallurgica et Materialia*, 40(3):519–532, 1992.

[21] G. Gottstein, A.D. Rollett, and L.S. Shvindlerman. On the validity of the von neumann–mullins relation. *Scripta Materialia*, 51(6):611–616, 2004.

[22] MA Palmer, VE Fradkov, ME Glicksman, and K Rajan. Experimental assessment of the mullins-von neumann grain growth law. *Scripta Metallurgica et Materialia*, 30(5):633–637, 1994.

[23] Erik M Lauridsen, Søren Schmidt, RM Suter, and Henning Friis Poulsen. Tracking: a method for structural characterization of grains in powders or polycrystals. *Journal of Applied Crystallography*, 34:744–750, 2001.

[24] RM Suter, D Hennessy, C Xiao, and U Lienert. Forward modeling method for microstructure reconstruction using X-ray diffraction microscopy: Single-crystal verification. *Review of Scientific Instruments*, 77(12):123905, 2006.

[25] H.F. Poulsen. *Three-Dimensional X-ray Diffraction Microscopy*, volume 205. Springer Tracts in Modern Physics, Berlin, 2004.

[26] W. Ludwig, S. Schmidt, E.M. Lauridsen, and H.F. Poulsen. X-ray diffraction contrast tomography: a novel technique for three-dimensional grain mapping of polycrystals. i. direct beam case. *J. Appl. Cryst.*, 41:302–309, 2008.

[27] Wenge Yang, BC Larson, JZ Tischler, GE Ice, JD Budai, and W Liu. Differential-aperture x-ray structural microscopy: a submicron-resolution three-dimensional probe of local microstructure and strain. *Micron*, 35(6):431–439, 2004.

[28] J. Zhang, Y. Zhang, W. Ludwig, D. Rowenhorst, P.W. Voorhees, and H.F. Poulsen. Three-dimensional grain growth in pure iron. part i. statistics on the grain level. *Acta Materialia*, 156:76–85, 2018.

[29] IM McKenna, SO Poulsen, EM Lauridsen, W Ludwig, and PW Voorhees. Grain growth in four dimensions: A comparison between simulation and experiment. *Acta Materialia*, 78:125–134, 2014.

[30] J. Sun, A. Lyckegaard, Y.B. Zhang, S.A. Catherine, B.R. Patterson, F. Bachmann, N. Gueninchault, H. Bale, C. Holzner, E. Lauridsen, and D. Juul Jensen. 4d study of grain growth in armco iron using laboratory x-ray diffraction contrast tomography. In *IOP Conf. Ser: Mater. Sci. Eng*, volume 219, 2017, 2017.

[31] S.A. McDonald, P. Reischig, C. Holzner, E. M. Lauridsen, P.J. Withers, A.P. Merkle, and M. Feser. Non-destructive mapping of grain orientations in 3d by laboratory x-ray microscopy. *Scientific Reports*, 5:14665.1–11, 2015.

[32] CM Hefferan, SF Li, J Lind, and RM Suter. Tests of microstructure reconstruction by forward modeling of hedm data. *Advances in X-ray Analysis*, 53, 2009.

[33] U. Lienert, S.F. Li, C.M. Hefferan, J. Lind, R.M. Suter, J.V. Bernier, N. Barton, M. Brandes, M. Mills, M.P. Miller, B. Jakobsen, and W. Pantleon. High-energy diffraction microscopy at the advanced photon source. *JOM*, 63:70–77, 2011.

[34] S.F. Li. *Imaging of Orientation and Geometry in Microstructures: Development and Applications of High Energy X-ray Diffraction Microscopy.* PhD thesis, Carnegie Mellon University, 2011.

[35] C. M. Hefferan. *Measurement of Annealing Phenomena in High Purity Metals with Near-field High Energy X-ray Diffraction Microscopy.* PhD thesis, Carnegie Mellon Univeristy, 2012.

[36] M. Syha. *Microstructure Evolution in Strontium Titanate.* PhD thesis, Karlsruher Institut für Technologie (KIT), 2014.

[37] S. Schmidt, S.F. Nielsen, C. Gundlach, L. Margulies, X. Huang, and D. Juul Jensen. Watching the growth of bulk grains during recrystallization of deformed metals. *Science*, 305:229–232, 2004.

[38] J. Lind, A.D. Rollett, R. Pokharel, C.M. Hefferan, S.F. Li, and R.M. Suter U. Lienert. Image processing in experiments on, and simulations of, plastic deformation of polycrystals. In *IEEE International Conference on Image Processing (ICIP)*, IEEE International Conference Image Processing, pages 4877–4881, 2014.

[39] D. B. Menasche, P. A. Shade, and R. M. Suter. Accuracy and precision of near-field high-energy diffraction microscopy forward-model-based microstructure reconstructions. *Journal of Applied Crystallography*, 53(1):107–116, Feb 2020.

[40] Michael A. Groeber and Michael A. Jackson. Dream.3d: A digital representation environment for the analysis of microstructure in 3d. *Integrating Materials and Manufacturing Innovation*, 3:5, Apr 2014.

[41] DJ Rowenhorst, AC Lewis, and G Spanos. Three-dimensional analysis of grain topology and interface curvature in a β-titanium alloy. *Acta Materialia*, 58(16):5511–5519, 2010.

[42] V. Yadav and Nele Moelans. Analysis of grain topology and volumetric growth rate relation in three-dimensional normal grain growth. *Acta Materialia*, 156:275–286, 2018.

[43] WW Mullins. The statistical self-similarity hypothesis in grain growth and particle coarsening. *Journal of Applied Physics*, 59(4):1341–1349, 1986.

[44] Xiaoting Zhong, David J. Rowenhorst, Hossein Beladi, and Gregory S. Rohrer. The five-parameter grain boundary curvature distribution in an austenitic and ferritic steel. *Acta Materialia*, 123:136 – 145, 2017.

[45] Sutatch Ratanaphan, D.L. Olmsted, V.V. Bulatov, E.A. Holm, A.D. Rollett, and G.S. Rohrer. Grain boundary energies in body-centered cubic metals. *Acta Materialia*, 88:346–354, 2015.

[46] B. Lin, Y. Jin, C.M. Hefferan, S.F. Li, J. Lind, R.M. Suter, M. Bernacki, N. Bozzolo, and G.S. Rohrer A.D. Rollet and. Observation of annealing twin nucleation at triple lines in nickel during grain growth. *Acta Materialia*, 99:63–68, 2015.

[47] Aditi Bhattacharya, Yu-Feng Shen, Christopher M Hefferan, Shiu Fai Li, Jonathan Lind, Robert M Suter, and Gregory S Rohrer. Three-dimensional

observations of grain volume changes during annealing of polycrystalline ni. *Acta Materialia*, 167:40–50, 2019.

[48] Yu-Feng Shen, Xiaoting Zhong, He Liu, Robert M Suter, Adam Morawiec, and Gregory S Rohrer. Determining grain boundary energies from triple junction geometries without discretizing the five-parameter space. *Acta Materialia*, 166:126–134, 2019.

[49] Oliver K. Johnson and Christopher A. Schuh. Texture mediated grain boundary network design in three dimensions. *Mechanics of Materials*, 118:94 – 105, 2018.

[50] H Kokawa, M Shimada, M Michiuchi, ZJ Wang, and YS Sato. Arrest of weld-decay in 304 austenitic stainless steel by twin-induced grain boundary engineering. *Acta Materialia*, 55(16):5401–5407, 2007.

[51] Gary S Was, Visit Thaveeprungsriporn, and Douglas C Crawford. Grain boundary misorientation effects on creep and cracking in Ni-based alloys. *JOM*, 50(2):44–49, 1998.

[52] William T Read and W Shockley. Dislocation models of crystal grain boundaries. *Physical Review*, 78(3):275, 1950.

[53] MF Ashby, F Spaepen, and S Williams. The structure of grain boundaries described as a packing of polyhedra. *Acta Metallurgica*, 26(11):1647–1663, 1978.

[54] HJ Fecht and H Gleiter. A lock-in model for the atomic structure of interphase boundaries between metals and ionic crystals. *Acta Metallurgica*, 33(4):557–562, 1985.

[55] Dieter Wolf. A broken-bond model for grain boundaries in face-centered cubic metals. *Journal of Applied Physics*, 68(7):3221–3236, 1990.

[56] Dieter Wolf and Sidney Yip. *Materials Interfaces: Atomic-level Structure and Properties*. Springer Science & Business Media, 1992.

[57] Paul Lacombe and Nicolas Yannaquis. la corrosion intercristalline de l'aluminium de haute pureté et ses conséquences au sujet de la nature des joints de grains. *Revue de Métallurgie*, 45(3-4):68–77, 1948.

[58] GJ Wood, WM Stobbs, and David J Smith. Methods for the measurement of rigid-body displacements at edge-on boundaries using high-resolution electron microscopy. *Philosophical Magazine A*, 50(3):375–391, 1985.

[59] KL Merkle and David J Smith. Atomic structure of symmetric tilt grain boundaries in NiO. *Physical Review Letters*, 59(25):2887, 1987.

[60] KL Merkle. Rigid-body displacement of asymmetric grain boundaries. *Scripta Metallurgica;(USA)*, 23(9), 1989.

[61] Vasily V Bulatov, Bryan W Reed, and Mukul Kumar. Grain boundary energy function for fcc metals. *Acta Materialia*, 65:161–175, 2014.

[62] D Wolf. A Read-Shockley model for high-angle grain boundaries. *Scripta Metallurgica*, 23(10):1713–1718, 1989.

[63] David L. Olmsted, Stephen M. Foiles, and Elizabeth A. Holm. Survey of computed grain boundary properties in face-centered cubic metals: I. grain boundary energy. *Acta Materialia*, 57(13):3694 – 3703, 2009.

[64] A Morawiec. Method to calculate the grain boundary energy distribution over the space of macroscopic boundary parameters from the geometry of triple junctions. *Acta Materialia*, 48(13):3525–3532, 2000.

[65] David M. Saylor, Adam Morawiec, and Gregory S. Rohrer. The relative free energies of grain boundaries in magnesia as a function of five macroscopic parameters. *Acta Materialia*, 51(13):3675 – 3686, 2003.

[66] Jia Li, Shen J. Dillon, and Gregory S. Rohrer. Relative grain boundary area and energy distributions in nickel. *Acta Materialia*, 57(14):4304 – 4311, 2009.

[67] Shen J Dillon and Gregory S Rohrer. Characterization of the grain boundary character and energy distributions of Yttria using automated serial sectioning and EBSD in the FIB. *Journal of the American Ceramic Society*, 92(7):1580–1585, 2009.

[68] Hossein Beladi and Gregory S Rohrer. The relative grain boundary area and energy distributions in a ferritic steel determined from three-dimensional electron backscatter diffraction maps. *Acta Materialia*, 61(4):1404–1412, 2013.

[69] Hossein Beladi, Noel T Nuhfer, and Gregory S Rohrer. The five-parameter grain boundary character and energy distributions of a fully austenitic high-manganese steel using three dimensional data. *Acta Materialia*, 70:281–289, 2014.

[70] Conyers Herring. Surface tension as a motivation for sintering. *The Physics of Powder Metallurgy*, 27(2):143–179, 1951.

[71] David W Hoffman and John W Cahn. A vector thermodynamics for anisotropic surfaces: I. Fundamentals and application to plane surface junctions. *Surface Science*, 31:368–388, 1972.

[72] Jl Cahn and Dl Hoffman. A vector thermodynamics for anisotropic surfaces II. Curved and faceted surfaces. *Acta Metallurgica*, 22(10):1205–1214, 1974.

[73] David M Saylor, Adam Morawiec, and Gregory S Rohrer. Distribution of grain boundaries in magnesia as a function of five macroscopic parameters. *Acta Materialia*, 51(13):3663–3674, 2003.

[74] Krzysztof Glowinski and Adam Morawiec. Analysis of experimental grain boundary distributions based on boundary-space metrics. *Metallurgical and Materials Transactions A*, 45(8):3189–3194, 2014.

[75] Robert A Schwarzer, David P Field, Brent L Adams, Mukul Kumar, and Adam J Schwartz. Present state of electron backscatter diffraction and prospective developments. In *Electron backscatter diffraction in materials science*, pages 1–20. Springer, 2009.

[76] Andrew V Knyazev. Toward the optimal preconditioned eigensolver: Locally optimal block preconditioned conjugate gradient method. *SIAM Journal on Scientific Computing*, 23(2):517–541, 2001.

[77] David M. Saylor, Adam Morawiec, Brent L. Adams, and Gregory S. Rohrer. Misorientation dependence of the grain boundary energy in magnesia. *Interface Science*, 8(2):131–140, Aug 2000.

[78] John W. Cahn and Jean E. Taylor. Metrics, measures, and parametrizations for grain boundaries: a dialog. *Journal of Materials Science*, 41(23):7669–7674, Dec 2006.

[79] David L. Olmsted. A new class of metrics for the macroscopic crystallographic space of grain boundaries. *Acta Materialia*, 57(9):2793 – 2799, 2009.

[80] A. P. Sutton, E. P. Banks, and A. R. Warwick. The five-dimensional parameter space of grain boundaries. *Proceedings of the Royal Society of London A: Mathematical, Physical and Engineering Sciences*, 471(2181), 2015.

[81] A. Morawiec. Comment on 'the five- dimensional parameter space of grain boundaries' by sutton et al. *Proceedings of the Royal Society of London A: Mathematical, Physical and Engineering Sciences*, 472(2187), 2016.

[82] A. P. Sutton. Response to commentary by morawiec. *Proceedings of the Royal Society of London A: Mathematical, Physical and Engineering Sciences*, 472(2187), 2016.

[83] H.F. Poulsen and G.B.M. Vaughan. *Multigrain crystallography and three-dimensional grain mapping*, volume H, chapter 5.5, pages 601–616. International Union of Crystallography, 2019.

[84] R. Pokharel. Overview of high-energy x-ray diffraction microscopy (hedm) for mesoscale material characterization in three-dimensions. In T. Lookman, S. Eidenbenz, F. Alexander, and C. Barnes, editors, *Materials Discovery and Design, Springer Series in Materials Science*, volume 280, pages 167–201. Springer, Cham, 2018.

[85] J. Lind, S.F. Li, R. Pokharel, U. Lienert, A.D. Rollett, and R.M. Suter. Tensile twin nucleation events coupled to neighboring slip observed in three dimensions. *Acta Materialia*, 76:213 – 220, 2014.

[86] D.B. Menasche, J. Lind, S.F. Li, P. Kenesei, J.F. Bingert, U. Lienert, and R.M. Suter. Shock induced damage in copper: A before and after, three-dimensional study. *Journal of Applied Physics*, 119:154902–7, 2016.

[87] R. Pokharel, J.F. Lind, A.K. Kanjarla, R.A. Lebensohn, S.F. Li, P. Kenesei, R.M. Suter, and A.D. Rollett. Polycrystal plasticity: Comparison between grain-scale observations of deformation and simulations. *Annual Reviews of Condensed Matter Physics*, 5(1):317–346, 2014.

[88] C.M. Hefferan, S.F. Li, J. Lind, U. Lienert, A.D. Rollett, and R.M. Suter. Observation of recovery and recrystallization in high purity aluminum measured with forward modeling analysis of high energy diffraction microscopy. *Acta Materialia*, 60:4311–4318, 2012.

[89] Y. Hayashi, D. Setoyama, Y. Hirose, T. Yoshida, and H. Kimura. Intragranular three-dimensional stress tensor fields in plastically deformed polycrystals. *Science*, 366:1492–1496, 2019.

[90] A. Bagri, J.P. Hanson, J. Lind, P. Kenesei, R.M. Suter, S. Gradečak, and M.J. Demkowicz. Measuring grain boundary character distributions in ni-base alloy 725 using high-energy diffraction microscopy. *Metallurgical and Materials Transactions*, 48:354–361, 2016.

[91] Oliver H Seeck and Bridget Murphy. *X-ray Diffraction: Modern Experimental Techniques*. Jenny Stanford Publishing, 2015.

[92] W. R. Busing and H. A. Levy. Angle calculations for 3- and 4- circle x-ray and neutron diffractometers. *Acta Crystallographica*, 22:457–464, 1967.

[93] J.V. Bernier, N.R. Barton, U. Lienert, and M.P. Miller. Far-field high-energy diffraction microscopy: a tool for intergranular orientation and strain analysis. *The Journal of Strain Analysis for Engineering Design*, 46(7):527–547, 2011.

[94] Jonathan F Lind. *In-situ high-energy diffraction microscopy study of zirconium under uni-axial tensile deformation*. PhD thesis, Carnegie Mellon Univeristy, 2013.

[95] J.C. Schuren, P.A. Shade, J.V. Bernier, S.F. Li, B. Blank, J. Lind, P. Kenesei, U. Lienert, R.M. Suter, T.J. Turner, D.M. Dimiduk, and J. Almer. New opportunities for quantitative tracking of polycrystal responses in three dimensions. *Current Opinion In Solid State and Materials Science*, 19:235–244, 2015.

[96] P. T. De Boer, D. P Kroese, Shie M., and Reuven Y R. A tutorial on the cross-entropy method. *Annals of operations research*, 134:19–67, 2005.

[97] S. Kullback and R. A. Leibler. On information and sufficiency. *The annals of mathematical statistics*, 22:79–86, 1951.

[98] Ricardo A. Lebensohn, Anand K. Kanjarla, and Philip Eisenlohr. An elasto-viscoplastic formulation based on fast fourier transforms for the prediction of micromechanical fields in polycrystalline materials. *International Journal of Plasticity*, 32-33:59 – 69, 2012.

[99] B.S. Anglin, R.A. Lebensohn, and A.D. Rollett. Validation of a numerical method based on fast fourier transforms for heterogeneous thermoelastic materials by comparison with analytical solutions. *Computational Materials Science*, 87:209 – 217, 2014.

[100] Kamalika Chatterjee. Determination of grain-level strain and proposing a new method of strain determination for three dimensional x-ray diffraction (3dxrd), 2014.

[101] Ciyou Zhu, Richard H. Byrd, Peihuang Lu, and Jorge Nocedal. Algorithm 778: L-bfgs-b: Fortran subroutines for large-scale bound-constrained optimization. *ACM Trans. Math. Softw.*, 23(4):550–560, December 1997.

[102] David L McDowell. A perspective on trends in multiscale plasticity. *International Journal of Plasticity*, 26(9):1280–1309, 2010.

[103] Robert Suter. Multiscale measurements for materials modeling. *Science*, 356(6339):704–705, 2017.

[104] Angus J Wilkinson and T Ben Britton. Strains, planes, and ebsd in materials science. *Materials today*, 15(9):366–376, 2012.

[105] Reeju Pokharel, Jonathan Lind, Shiu Fai Li, Peter Kenesei, Ricardo A Lebensohn, Robert M Suter, and Anthony D Rollett. In-situ observation of bulk 3d grain evolution during plastic deformation in polycrystalline cu. *International Journal of Plasticity*, 67:217–234, 2015.

[106] A. E. Gleason, C. A. Bolme, E. Galtier, H. J. Lee, E. Granados, D. H. Dolan, C. T. Seagle, T. Ao, S. Ali, A. Lazicki, D. Swift, P. Celliers, and W. L. Mao. Compression freezing kinetics of water to ice vii. *Physical review letters*, 119(2):025701, 2017.

[107] Stuart I Wright and Matthew M Nowell. A review of in situ ebsd studies. In *Electron Backscatter Diffraction in Materials Science*, pages 329–337. Springer, 2009.

[108] T.B. Britton, J. Jiang, Y. Guo, A. Vilalta-Clemente, D. Wallis, L.N. Hansen, A. Winkelmann, and A.J. Wilkinson. Tutorial: Crystal orientations and ebsd — or which way is up? *Materials Characterization*, 117:113–126, 2016.

[109] Stuart I Wright, Matthew M Nowell, Scott P Lindeman, Patrick P Camus, Marc De Graef, and Michael A Jackson. Introduction and comparison of new ebsd post-processing methodologies. *Ultramicroscopy*, 159:81–94, 2015.

[110] Dipendra Jha, Saransh Singh, Reda Al-Bahrani, Wei-keng Liao, Alok Choudhary, Marc De Graef, and Ankit Agrawal. Extracting grain orientations from ebsd patterns of polycrystalline materials using convolutional neural networks. *Microscopy and Microanalysis*, 24(5):497–502, 2018.

[111] Ahmed Fakhry, Tao Zeng, and Shuiwang Ji. Residual deconvolutional networks for brain electron microscopy image segmentation. *IEEE transactions on medical imaging*, 36(2):447–456, 2017.

[112] Tran Minh Quan, David G. C. Hildebrand, and Won-Ki Jeong. Fusionnet: A deep fully residual convolutional neural network for image segmentation in connectomics. *CoRR*, abs/1612.05360, 2016.

[113] Bo Zhu, Jeremiah Z Liu, Stephen F Cauley, Bruce R Rosen, and Matthew S Rosen. Image reconstruction by domain-transform manifold learning. *Nature*, 555(7697):487, 2018.

[114] Alex Krizhevsky, Ilya Sutskever, and Geoffrey E Hinton. Imagenet classification with deep convolutional neural networks. In *Advances in neural information processing systems*, pages 1097–1105, 2012.

[115] Shaoqing Ren, Kaiming He, Ross Girshick, and Jian Sun. Faster r-cnn: Towards real-time object detection with region proposal networks. In *Advances in neural information processing systems*, pages 91–99, 2015.

[116] Alex Kendall, Matthew Grimes, and Roberto Cipolla. Posenet: A convolutional network for real-time 6-dof camera relocalization. In *Proceedings of the IEEE international conference on computer vision*, pages 2938–2946, 2015.

[117] Tomoyoshi Shimobaba, Takashi Kakue, and Tomoyoshi Ito. Convolutional neural network-based regression for depth prediction in digital holography. *arXiv preprint arXiv:1802.00664*, 2018.

[118] R. Liu, A. Agrawal, W. Liao, A. Choudhary, and M. De Graef. Materials discovery: Understanding polycrystals from large-scale electron patterns. In *2016 IEEE International Conference on Big Data (Big Data)*, pages 2261–2269, Dec 2016.

[119] Xiaodong Tao and Alwyn Eades. Errors, artifacts, and improvements in ebsd processing and mapping. *Microscopy and Microanalysis*, 11(1):79–87, 2005.

[120] Stuart I Wright and Matthew M Nowell. Ebsd image quality mapping. *Microscopy and microanalysis*, 12(1):72–84, 2006.

[121] Yu H. Chen, Se Un Park, Dennis Wei, Greg Newstadt, Michael A. Jackson, Jeff P. Simmons, Marc De Graef, and Alfred O. Hero. A dictionary approach to electron backscatter diffraction indexing. *Microscopy and Microanalysis*, 21(3):739–752, 2015.

[122] Patrick G Callahan and Marc De Graef. Dynamical electron backscatter diffraction patterns. part i: Pattern simulations. *Microscopy and Microanalysis*, 19(5):1255–1265, 2013.

[123] M De Graef. Emsoft 3.0, 2015. Software available from http://muri.materials.cmu.edu/?p=858/.

[124] George Cybenko. Approximation by superpositions of a sigmoidal function. *Mathematics of control, signals and systems*, 2(4):303–314, 1989.

[125] Kurt Hornik, Maxwell Stinchcombe, and Halbert White. Multilayer feedforward networks are universal approximators. *Neural networks*, 2(5):359–366, 1989.

[126] Yann LeCun, Yoshua Bengio, et al. Convolutional networks for images, speech, and time series. *The handbook of brain theory and neural networks*, 3361(10):1995, 1995.

[127] Diederik P Kingma and Jimmy Ba. Adam: A method for stochastic optimization. *arXiv preprint arXiv:1412.6980*, 2014.

[128] Xavier Glorot, Antoine Bordes, and Y Bengio. Deep sparse rectifier neural networks. 15:315–323, 01 2011.

[129] Werner Dubitzky, Martin Granzow, and Daniel P Berrar. *Fundamentals of data mining in genomics and proteomics*. Springer Science & Business Media, 2007.

[130] Matthew D Zeiler, Dilip Krishnan, Graham W Taylor, and Rob Fergus. Deconvolutional networks. 2010.

[131] Ian Goodfellow, Yoshua Bengio, and Aaron Courville. *Deep Learning*. MIT Press, 2016. Book available from http://www.deeplearningbook.org/.

[132] Lluis Castrejon, Yusuf Aytar, Carl Vondrick, Hamed Pirsiavash, and Antonio Torralba. Learning aligned cross-modal representations from weakly aligned data. In *Proceedings of the IEEE Conference on Computer Vision and Pattern Recognition*, pages 2940–2949, 2016.

[133] Tiago S Nazaré, Gabriel B Paranhos da Costa, Welinton A Contato, and Moacir Ponti. Deep convolutional neural networks and noisy images. In *Iberoamerican Congress on Pattern Recognition*, pages 416–424. Springer, 2017.

[134] Steven Diamond, Vincent Sitzmann, Stephen Boyd, Gordon Wetzstein, and Felix Heide. Dirty pixels: Optimizing image classification architectures for raw sensor data. *arXiv preprint arXiv:1701.06487*, 2017.

[135] Viren Jain and Sebastian Seung. Natural image denoising with convolutional networks. In *Advances in Neural Information Processing Systems*, pages 769–776, 2009.

[136] Kai Zhang, Wangmeng Zuo, Yunjin Chen, Deyu Meng, and Lei Zhang. Beyond a gaussian denoiser: Residual learning of deep cnn for image denoising. *IEEE Transactions on Image Processing*, 26(7):3142–3155, 2017.

[137] Harold C Burger, Christian J Schuler, and Stefan Harmeling. Image denoising: Can plain neural networks compete with bm3d? In *Computer Vision and Pattern Recognition (CVPR), 2012 IEEE Conference on*, pages 2392–2399. IEEE, 2012.

[138] Kaiming He, Xiangyu Zhang, Shaoqing Ren, and Jian Sun. Deep residual learning for image recognition. In *Proceedings of the IEEE conference on computer vision and pattern recognition*, pages 770–778, 2016.

[139] Saransh Singh, Farangis Ram, and Marc De Graef. Application of forward models to crystal orientation refinement. *Journal of Applied Crystallography*, 50(6):1664–1676, 2017.

[140] Ben Poole, Subhaneil Lahiri, Maithra Raghu, Jascha Sohl-Dickstein, and Surya Ganguli. Exponential expressivity in deep neural networks through transient chaos. In *Advances in neural information processing systems*, pages 3360–3368, 2016.

[141] Hrushikesh Mhaskar, Qianli Liao, and Tomaso A Poggio. When and why are deep networks better than shallow ones? In *AAAI*, pages 2343–2349, 2017.

[142] Martín Abadi, Ashish Agarwal, Paul Barham, Eugene Brevdo, Zhifeng Chen, Craig Citro, Greg S. Corrado, Andy Davis, Jeffrey Dean, Matthieu Devin, Sanjay Ghemawat, Ian Goodfellow, Andrew Harp, Geoffrey Irving, Michael Isard,

Yangqing Jia, Rafal Jozefowicz, Lukasz Kaiser, Manjunath Kudlur, Josh Levenberg, Dandelion Mané, Rajat Monga, Sherry Moore, Derek Murray, Chris Olah, Mike Schuster, Jonathon Shlens, Benoit Steiner, Ilya Sutskever, Kunal Talwar, Paul Tucker, Vincent Vanhoucke, Vijay Vasudevan, Fernanda Viégas, Oriol Vinyals, Pete Warden, Martin Wattenberg, Martin Wicke, Yuan Yu, and Xiaoqiang Zheng. TensorFlow: Large-scale machine learning on heterogeneous systems, 2015. Software available from tensorflow.org.

[143] Nitish Srivastava, Geoffrey Hinton, Alex Krizhevsky, Ilya Sutskever, and Ruslan Salakhutdinov. Dropout: a simple way to prevent neural networks from overfitting. *The Journal of Machine Learning Research*, 15(1):1929–1958, 2014.

[144] Alex Kendall and Roberto Cipolla. Modelling uncertainty in deep learning for camera relocalization. *arXiv preprint arXiv:1509.05909*, 2015.

[145] Sinno Jialin Pan, Qiang Yang, et al. A survey on transfer learning. *IEEE Transactions on knowledge and data engineering*, 22(10):1345–1359, 2010.

[146] Ian Goodfellow, Jean Pouget-Abadie, Mehdi Mirza, Bing Xu, David Warde-Farley, Sherjil Ozair, Aaron Courville, and Yoshua Bengio. Generative adversarial nets. In *Advances in neural information processing systems*, pages 2672–2680, 2014.

[147] Phillip Isola, Jun-Yan Zhu, Tinghui Zhou, and Alexei A Efros. Image-to-image translation with conditional adversarial networks. In *Computer Vision and Pattern Recognition (CVPR), 2017 IEEE Conference on*, 2017.

[148] Judy Hoffman, Eric Tzeng, Taesung Park, Jun-Yan Zhu, Phillip Isola, Kate Saenko, Alexei A Efros, and Trevor Darrell. Cycada: Cycle-consistent adversarial domain adaptation. *arXiv preprint arXiv:1711.03213*, 2017.

[149] Péter Reischig and Wolfgang Ludwig. Three-dimensional sub-grain mapping of elastic strain state and orientations in the bulk of polycrystals. In *40th Risoe International Symposium on Metal Microstructures in 2D, 3D and 4D*, 2019.